PETROVIETNAM

SCIENCE, TECHNOLOGY & INNOVATION

PETROVIETNAM

SPECIAL ISSUE OF THE VIETNAM NATIONAL INDUSTRY - ENERGY GROUP

VOLUME 6/2025

ISSN 3030-4431

IMPLEMENTATION
Vietnam Petroleum Institute

CONTACT ADDRESS
Floor 16th, VPI Tower, Trung Kinh street, Yen Hoa ward, Hanoi
*Tel: 024-37727108 | 0982288671 * Fax: 024-37844156 * Email: tcdk@pvn.vn*

Publishing Licence No. 152/GP - XBĐS dated 12 December 2024 issued by Authority of Press, Authority of Press, Ministry of Culture, Sports and Tourism

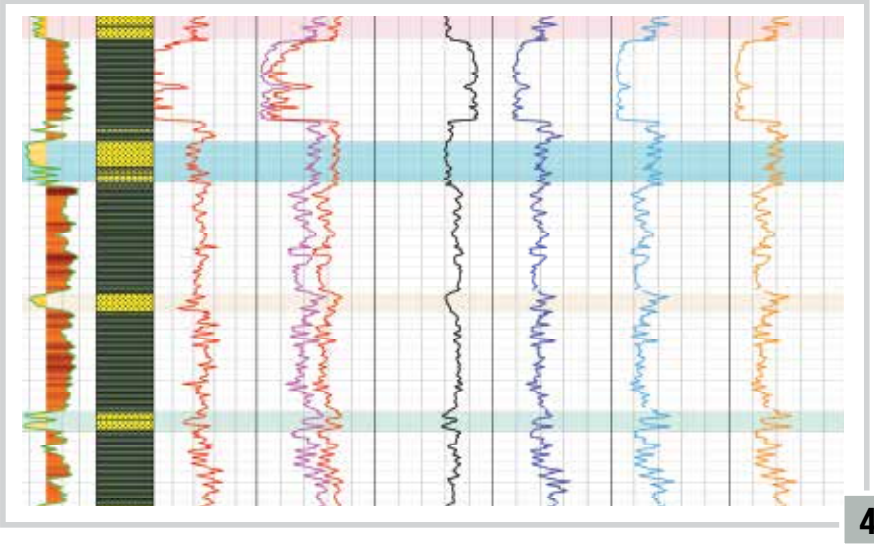

4

PETROLEUM - SCIENCE, TECHNOLOGY AND INNOVATION

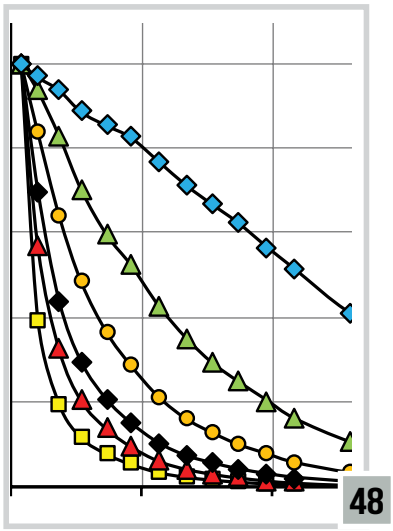

EDITORIAL BOARD'S MESSAGE

In line with the Strategy for Science and Technology Development, Innovation, and Digital Transformation to 2030, with a vision to 2050, the Vietnam National Industry - Energy Group (Petrovietnam) has set a goal to bring its scientific and technological capability, innovation capacity, and digital transformation maturity to a regional advanced level across multiple key areas, with some of which attaining international standards by 2030. Science and technology, innovation, and digital transformation are identified as new drivers of growth, which will help enhance labor productivity and competitiveness. These pillars will play a decisive role in enabling Petrovietnam to achieve sustainable double-digit growth, strengthen its overall capability, adopt modern governance practices, attain regional and international competitiveness, and secure its position among the world's top 500 companies (Fortune Global 500).

This Petrovietnam Special Issue on Science, Technology and Innovation presents results of the application of geomechanical methods in combination with wireline log data to predict sand production in weakly consolidated formations at Blocks 01&02, Cuu Long basin. The study proposes solutions to optimize well completion design, sand control strategies, and perforation planning, thereby enhancing production efficiency and mitigating operational risks in the Cuu Long basin. The Special Issue also features a study evaluating the performance of modified acid systems (CKP^+ and GKP^+) for acidizing sandstone formations in Bach Ho field, offering cost-effective solutions to improve well productivity and sustain long-term hydrocarbon recovery. Furthermore, a comprehensive research on technological solutions for associated gas gathering, transportation, and offshore field interconnection has opened new approaches to enhancing resource utilization efficiency, thus enabling an associated gas recovery rate of over 90%.

In addition, this Special Issue presents solutions to increase the flash point of DCO products to meet Dung Quat Refinery's FO (FP) standards, while also highlighting research on converting agricultural by-products into microcrystalline cellulose (MCC) for PLA-based biodegradable plastic production, thereby contributing to the diversification of petrochemical products toward sustainability. The Special Issue further analyzes the effectiveness of greenhouse gas and SO_2 emission reductions achieved through fuel conversion measures, along with the application of selective catalytic reduction (SCR) technology using DEF solutions to reduce NOx emissions from diesel engines, demonstrating Petrovietnam's strong commitment to the energy transition.

In implementing the Development Strategy to 2030, with a vision to 2050, Petrovietnam is firmly focusing its resources on core business areas while strategically advancing the LNG value chain, developing the offshore wind power ecosystem, restructuring the downstream sector, and laying the groundwork for nuclear power development - thereby supporting the energy transition and reinforcing the national energy security.

Entering 2026, the Editorial Board envisions the Petrovietnam Special Issue on Science, Technology and Innovation continuing to serve as a reputable scientific forum, contributing solutions in management, governance, and technology. Through this role, the Special Issue supports the development of 5 priority areas: international business operations, scientific research, digital transformation, digital data infrastructure development, and new product development, creating long-term growth potential for Petrovietnam.

EDITOR-IN-CHIEF
Vice President of Petrovietnam

Dr. Le Xuan Huyen

PETROVIETNAM
SCIENCE, TECHNOLOGY & INNOVATION PETROVIETNAM

SAND PRODUCTION RISK PREDICTION IN WEAKLY CONSOLIDATED FORMATIONS USING AN INTEGRATED GEOMECHANICAL APPROACH: A CASE STUDY FROM CUU LONG BASIN, OFFSHORE VIETNAM

Pham Quy Ngoc[1], Nguyen Van Thuan[2], Pham Truong Giang[1], Nguyen Minh Quy[1]
[1]Vietnam Petroleum Institute (VPI)
[2]Petrovietnam Drilling Service Corporation (PV Drilling)
Email: ngocpq@vpi.pvn.vn
https://doi.org/10.47800/PVSI.2025.06-01

Summary

Sand production during hydrocarbon extraction represents a critical operational challenge, particularly in weakly consolidated formations such as the Miocene sandstones of the Cuu Long basin, offshore Vietnam, leading to production losses, equipment damage, and potential well abandonment. Accurate prediction is essential for optimizing completion design and selecting suitable sand control.

This study presents a multi-index geomechanical approach for predicting sand production risk using five indicators: (1) sonic transit time (DTCO), (2) sand production index - BI, (3) Schlumberger sand production ratio - SR, (4) combined elastic modulus - E_c, and (5) unconfined compressive strength - UCS. These indices are derived from basic well logs (gamma-ray, sonic, and density) and calculated geomechanical parameters.

The methodology was applied to a well in Blocks 01&02 of the Cuu Long basin, where five major sand bodies were subdivided into 15 distinct sub-intervals subject to log response variations. Results reveal substantial intra-sand-body heterogeneity: Sands 1 - 4 consistently exhibit high risk with measured values below critical thresholds, while Sand 5 overall appears low-medium risk. A detailed analysis of Sand 5 indentifies three distinct sub-intervals with dramatically different characteristics. Field validation confirmed prediction accuracy, with 600 psi depletion triggering sand production in the predicted intervals.

Based on these findings, active sand control measures are recommended for all high-risk intervals to ensure safe and sustainable production. The integrated multi-index approach provides enhanced reliability compared to single-criterion methods and can be readily applied to analogous geological settings with similar formation characteristics, offering a cost-effective alternative to extensive core testing programs.

Key words: Sand production prediction, geomechanics, weakly consolidated formations, Cuu Long basin, well completion.

1. Introduction

Sand production during oil and gas extraction represents one of the most significant technical challenges in the petroleum industry globally, including in Vietnam's offshore fields. This phenomenon occurs when formation particles are entrained and transported by flowing fluids during production, resulting in a cascade of detrimental consequences including (i) reduced production rates due to plugged flow lines and equipment; (ii) erosion and damage to downhole and surface facilities; (iii) increased operational and maintenance costs; and (iv) potential well abandonment in severe cases. The industry estimates suggest that sand-related damage costs operators millions of dollars annually per affected well.

Over the past several decades, sand production prediction and control have attracted considerable attention from the international scientific community. Research efforts have focused on fundamental methodologies and models, as well as practical applications of wireline log analysis [1 - 10]. In Vietnam,

Date of receipt: 15/11/2025.
Date of review and editing: 15/11 - 6/12/2025.
Date of approval: 6/12/2025.

sand production research initiatives began in the 2000s with significant contributions from Vietnamese researchers [11 - 14].

Accurate determination of formation mechanical properties and sand production potential is essential for deciding whether sand control equipment is necessary and, if so, which type is most appropriate. Sand production susceptibility depends on the complex interplay of formation mechanical properties, in-situ stress field, perforation orientation and design, and reservoir pressure depletion during production. Additionally, formation strength progressively degrades due to fluid-rock interaction effects during production. Without proper completion design in the initial well completion phase, operators may face significant remedial costs, production deferment, or, in extreme cases, total well loss.

Various authors have proposed sand production prediction models based on field observations, drilling data, and laboratory core testing [2, 3, 7, 10]. However, these approaches suffer from several practical limitations:

- High cost and long testing durations: Core acquisition and laboratory testing programs are expensive and time-consuming, particularly in offshore environments.

- Limited sample availability: Many fields have restricted core coverage with limited numbers and sizes of samples, which is insufficient for comprehensive model calibration and regional extrapolation.

- Sample quality concerns: Core handling and preservation practices, differences between reservoir and laboratory conditions, and equipment limitations can compromise test results.

- Coverage gaps: Core data rarely provides complete vertical coverage of production intervals.

In contrast, basic wireline log measurements are routinely acquired in virtually all wells, providing excellent vertical resolution and formation representativeness.

This study leverages standard wireline log data to derive geomechanical parameters, which are then used to apply five established prediction indices: (i) compressional sonic transit time (DTCO), (ii) sand production index (B), (iii) Schlumberger sand production ratio (SR), (iv) combined elastic modulus (E_c), and (v) unconfined compressive strength (UCS). These methods have been successfully implemented in various global petroleum provinces by multiple researchers [1, 4, 9, 15].

According to established criteria, formations with high sand production potential requiring sand control from initial completion are characterized by the following threshold values of: BI < 20,000 MPa, SR < 1.24×10^8 MPa^2, E_c < 26,080 MPa, UCS < 27.58 MPa, and DTCO > ~95 µs/ft. This integrated approach offers an alternative perspective on sand production prediction and can enhance the reliability of predictive models and sand control strategies for the study area and analogous geological settings.

The study area is located within Blocks 01&02 of the Cuu Long basin on the southern Vietnamese continental shelf (Figure 1). The basin has undergone multiple tectonic phases including rifting, intense compression, and thermal subsidence, resulting in complex geology and lithology with diverse depositional facies and sedimentary environments. The primary producing intervals in this area are Miocene formations characterized by weakly consolidated, predominantly interbedded sand-shale sequences, making sand production a major operational concern.

The regional stratigraphic column (Figure 1) clearly displays the sedimentary succession of the Cuu Long basin, spanning from Pre-Tertiary basement to Pliocene - Quaternary deposits.

Basement and syn-rift sequence (Pre-Tertiary to Early Oligocene): The Pre-Tertiary basement comprises weathered and fractured granitoids and metamorphic rocks, which serve as the primary fractured basement reservoir in the basin.

The overlying Eocene Ca Coi and Tra Cu formations (Sequences F and E) consist of conglomerate, sandstone, shale, and thin coal/marl layers deposited in proluvial - alluvial to lacustrine - swamp environments during the initial rifting phase.

The Early Oligocene Tra Tan formation (Sequences C and D) is dominated by shale with andesite and basalt interbeds, indicating continued rifting with volcanic activity.

Transitional sequence (Late Oligocene to Early Miocene): The Bach Ho formation (Sequences B1.1 and B1.2) marks a transition from rifting to thermal subsidence, comprising interbedded sand, silt, shale, and localized basalt/tuff layers in swamp - alluvial - lacustrine to fluvial - marginal marine settings. This formation represents a major clastic reservoir interval where sand production is a significant concern due to poorly consolidated sandstones.

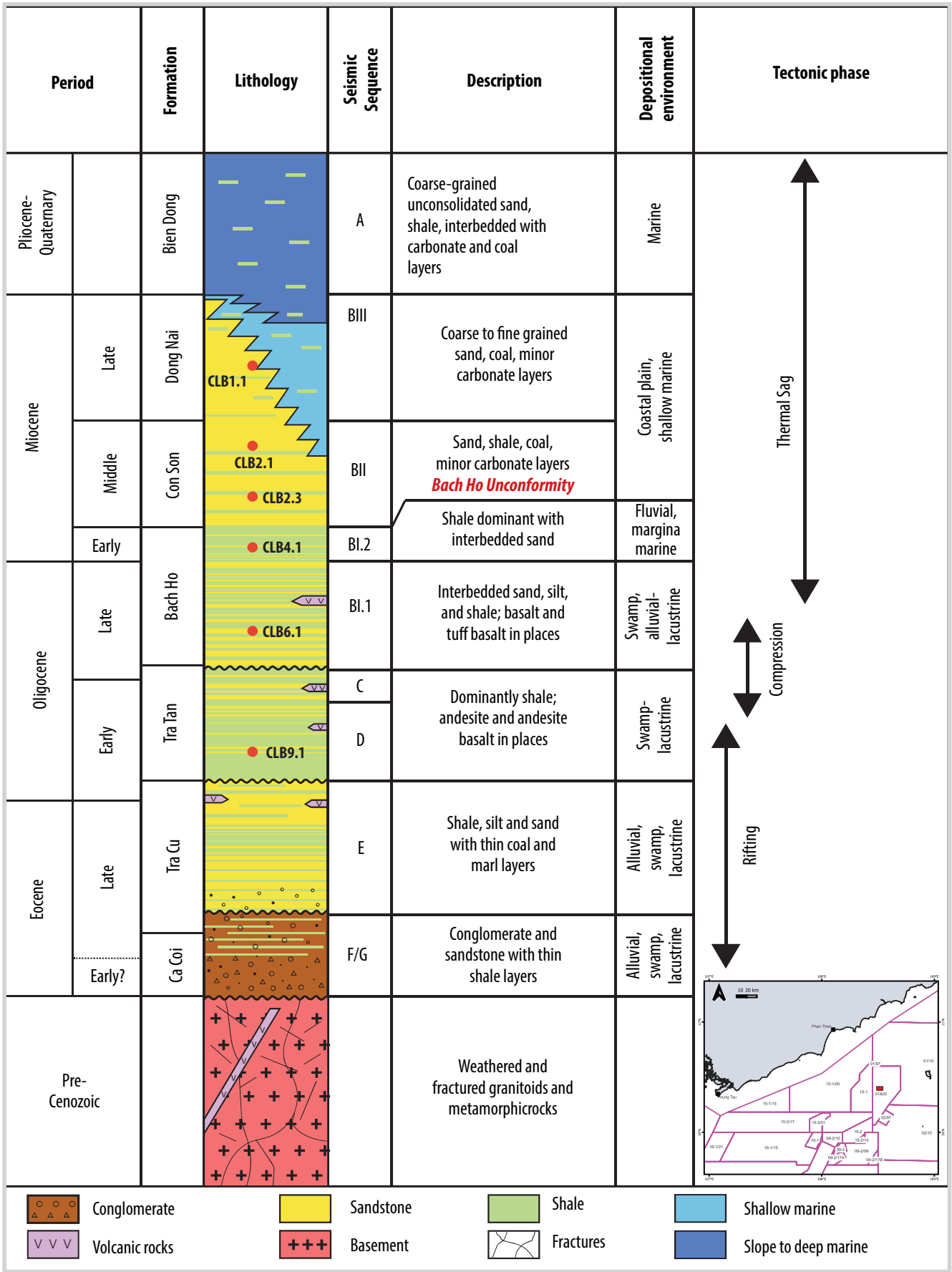

Figure 1. *Study area and stratigraphic characteristics.*

Post-rift thermal sag sequence (Middle Miocene to present): The Con Son, Dong Nai, and Bien Dong formations (Sequences B2, B3, and A) represent progressive marine transgression, evolving from fluvial - marginal marine to coastal - shallow marine and fully marine conditions. Lithologies grade upward from sand - shale - coal assemblages to coarse-grained unconsolidated sands with carbonate interbeds. These Miocene formations, particularly the Lower Miocene (Con Son) and Upper Miocene (Dong Nai) sequences, are the primary sand-producing intervals in the Cuu Long basin, characterized by weakly cemented, friable sandstones that are highly susceptible to sand production during hydrocarbon extraction.

2. Theoretical basis and methodology

2.1. Determination of geomechanical parameters

Accurate sand production prediction requires a comprehensive understanding of rock mechanical properties. Geomechanical parameters are derived from wireline log measurements, including gamma ray (GR), compressional sonic transit time (DTC, μs/ft) or velocity (V_p, km/s), shear sonic transit time (DTS, μs/ft) or velocity (V_s, km/s), and bulk density (ρ_b, kg/m^3). Key geomechanical parameters, including Poisson's ratio (ν), shear modulus (G, MPa), bulk modulus (K_b, MPa), Young's modulus (E, MPa), and unconfined compressive strength (UCS, MPa) are derived from Equations (1 - 6).

- Poisson's ratio (ν)

Poisson's ratio represents the ratio of transverse (lateral) strain to axial strain under uniaxial stress, quantifying the deformation response of formations to in-situ stress. It is calculated from compressional (V_p) and shear (V_s) wave velocities:

$$\nu = (V_p^2 - 2V_s^2)/[2(V_p^2 - V_s^2)] = (DTS^2 - 2DTC^2)/[2(DTS^2 - DTC^2)] \quad (1)$$

- Shear modulus (G)

Shear modulus represents the ratio of shear stress to shear strain, quantifying resistance to shape deformation. It is derived from bulk density (ρ_b) and shear wave velocity (V_s):

$$G_{dyn}\ (MPa) = \rho_b \times V_s^2 \quad (2)$$

- Bulk modulus (K_b)

Bulk modulus quantifies resistance to volumetric compression, representing the inverse of compressibility:

$$K_{b\_dyn}\ (MPa) = \rho_b \times (V_p^2 - 4/3 \times V_s^2) \quad (3)$$

- Young's modulus (E)

Young's modulus, or elastic modulus, represents the ratio of axial stress to axial strain, quantifying formation stiffness:

$$E\ (MPa) = \rho_b V_s^2 \times (3V_p^2 - 4V_s^2)/(V_p^2 - V_s^2) = 9K_bG/[3(K_b + G)] \quad (4)$$

- Unconfined compressive strength (UCS)

UCS quantifies formation resistance to axial deformation under overburden pressure. For shale formations, the Horsrud [16] correlation is applied:

$$UCS\ (MPa) = 0.77 \times V_p^{2.93} \quad (5)$$

For weakly consolidated sandstones, the McNally [17] relationship is employed:

$$UCS\ (MPa) = 1200 \times exp[-0.0367(304800/V_p)] \quad (6)$$

2.2. Sand production prediction methodologies

To assess sand production potential, the following five complementary criteria are applied:

- Compressional sonic transit time method

Formation consolidation strength is indicated by compressional wave velocity; lower velocities correlate with higher susceptibility to failure and sand production. Empirically, formations with compressional sonic transit times below 95 μs/ft are generally stable. Conversely, higher transit times indicate elevated sand production risk requiring mitigation measures. The critical threshold varies among fields, but for weakly consolidated sandstones, sand production typically occurs when the DTCO exceeds 95 μs/ft [4]. For this study, a slightly more optimistic threshold of 93 μs/ft is adopted to optimize prediction criteria.

- Sand production index (BI) method

Petroleum engineers routinely employ wireline logs for assessing sand production due to difficulties in obtaining intact core samples from unconsolidated sands. Two principal log-based methods exist: the Schlumberger ratio (SR) and the sand production index (BI). Higher BI values indicate greater elastic modulus and superior rock strength. According to Dong et al. [4], formations with BI below 20,000 MPa exhibit high sand production potential and require control measures. The index is calculated as:

$$BI = E/[3(1 - 2\nu)] + (4/3) \times E/[2(1 + \nu)] \quad (7)$$

where: BI = sand production index (MPa); E = dynamic Young's modulus from logs (MPa); ν = dynamic Poisson's ratio from logs

- Schlumberger sand production ratio (SR) method

For more precise strength and sand production assessment, Schlumberger's model defined the SR index based on bulk modulus (K_b) and shear modulus (G) per Equation (8). Similar to BI, higher SR values indicate greater strength due to increased elastic, shear, and bulk moduli. Schlumberger established that SR values below 1.24×10^8 MPa^2 indicate high sand production potential [4, 6, 9]:

$$SR = K \times G = [E/3(1-2\nu)] \times [E/2(1+\nu)]$$

- Combined elastic modulus (E_c) method

This method utilizes sonic and density logs to calculate E_c. Formations become unstable and produce sand when E_c falls below 26,080 MPa, requiring sand control measures [4, 6, 9]:

$$E_c = (3.03 \times 10^8 \times \rho b)/DTCO_2$$

where: E_c = combined modulus sand production index (MPa); DTCO = compressional sonic transit time (μs/ft); ρ_b = bulk density (g/cm^3)

- Rock strength (UCS) method

According to formation mechanical principles, weaker sands with lower UCS exhibit higher sand production potential and instability during drilling and production. In this study area, formations with UCS below 27.58 MPa are classified susceptible to sand production.

3. Results and discussion

3.1. Lithology identification and geomechanical characterization

The study area was subdivided into sand and shale lithologies based on gamma ray log response. Specifically, Sand bodies 1, 2, 3, and 4 exhibit gamma ray values below

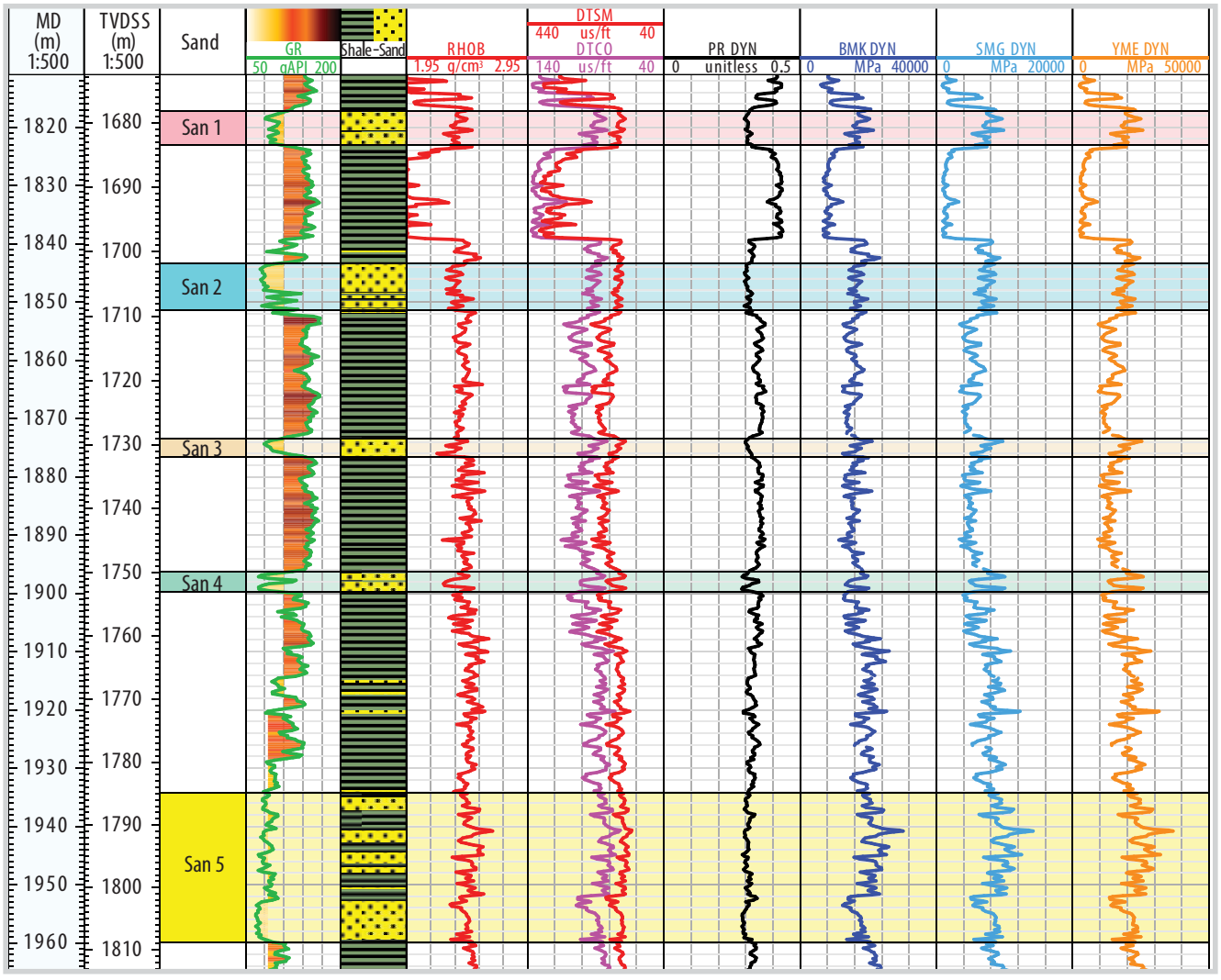

Figure 2. *Lithology and data input for sanding risk analysis.*

Table 1. *Geomechanical parameters for individual sub-intervals showing intra-sand-body variability*

Sand intervals	Sub-interval	Depth (m)	Poisson ratio	Bulk modulus (MPa)	Shear modulus (MPa)	Young modulus (MPa)	UCS (MPa)	DTCO (µs/ft)
Sand 1	Sand 1a	1,817 - 1,821	0.310	16,800	7,350	18,200	25.8	92.5
	Sand 1b	1,821 - 1,823	0.307	17,200	7,650	19,400	27.9	89.8
Sand 2	Sand 2a	1,843 - 1,845	0.309	16,450	7,280	19,050	26.9	91.2
	Sand 2b	1,845 - 1,847	0.312	16,100	7,100	17,800	25.1	93.8
	Sand 2c	1,847 - 1,849	0.306	16,750	7,380	19,350	27.4	90.5
	Sand 2d	1,849 - 1,851	0.305	16,900	7,500	19,900	28.1	89.2
Sand 3	Sand 3a	1,873 - 1,875	0.311	16,500	7,180	18,750	26.2	92.1
	Sand 3b	1,875 - 1,876	0.310	16,600	7,240	19,020	26.6	91.6
Sand 4	Sand 4a	1,896 - 1,898	0.313	16,450	7,150	18,480	25.5	93.2
	Sand 4b	1,898 - 1,899	0.309	16,750	7,400	19,550	27.6	91.0
Sand 5	Sand 5a	1,934 - 1,953	0.304	20,100	9,050	24,500	33.8	83.5
	Sand 5b	1,953 - 1,955	0.308	16,250	7,100	19,100	26.5	95.2
	Sand 5c	1,955 - 1,959	0.307	19,500	8,650	22,800	31.2	87.8

110 API, while Sand 5 shows values below 85 API (Figure 2). Individual sand body thicknesses range from 3.2 to 25.73 m as detailed in Tables 1 and 2. According to field reports [18], these productive intervals began experience sand production after approximately 600 psi of reservoir pressure depletion.

Figure 2 and Table 1 present calculated geomechanical parameters and rock strength derived from wireline log data. Average values for Sands 1 - 5 include Young's modulus (YME_DYN) of 18,888 - 23,204 MPa, shear modulus (SMG_DYN) of 7,212 - 8,894 MPa, bulk modulus (BMK_DYN) of 16,536 - 19,851 MPa, and Poisson's ratio (PR_DYN) of 0.305 - 0.311. Minimum YME_DYN and SMG_DYN occur in Sand 3, while minimum BMK_DYN and PR_DYN occur in Sand 2 and Sand 5, respectively.

Rock strength (UCS) ranges from 26.08 to 32.69 MPa across all intervals. The minimum UCS of 26.08 MPa in Sand 4 indicates the weakest consolidation, which, when combined with its limited thickness (3.42 m), suggests a significant influence from bounding shale intervals, resulting in elevated sand production potential. Conversely, Sand 5 exhibits maximum UCS (32.69 MPa) along with the highest elastic, shear, and bulk moduli. Additionally, greater burial depth subjects Sand 5 to increased overburden stress, further enhancing consolidation. Therefore, Sand 5 demonstrates superior consolidation and the lowest sand production risk among all intervals.

3.2. Sand production risk assessment

Geomechanical parameters were utilized to calculate sand production indices according to the methodologies described above. Results are presented in Table 2 and Figure 3.

- Compressional sonic transit time analysis

Formations with high sand production potential exhibit DTCO values exceeding 93 µs/ft, representing a slight optimization from the 95 µs/ft threshold proposed by Dong et al. [4]. Analysis of Figure 3 and Table 2 reveals DTCO values ranging from 85 to 135 µs/ft, with interval averages of 85.75 to 92.61 µs/ft. Sands 1 - 4 show average values of 90.59 - 92.61 µs/ft, all exceed the 90 µs/ft threshold, while Sand 5 (85.75 µs/ft) falls below. These results indicate that Sands 1 - 4 exhibit higher sand production potential than Sand 5 by this criterion, although isolated intervals within Sand 5 exceed the threshold (shown in red, Figure 3).

- Sand production index (BI) analysis

Increasing BI values indicate greater elastic modulus and enhanced rock stability. Formations with BI below 20,000 MPa exhibit high sand production potential [4]. For the study area, average BI values for Sands 1 - 5 are 20,427.79, 19,906.36, 19,900.20, 19,934.94, and 23,372.15 MPa, respectively (Table 2 and Track 7, Figure 3). Only Sand 1 and Sand 5 exceed the threshold, indicating that Sand 5 exhibits the lowest sand production risk by this criterion.

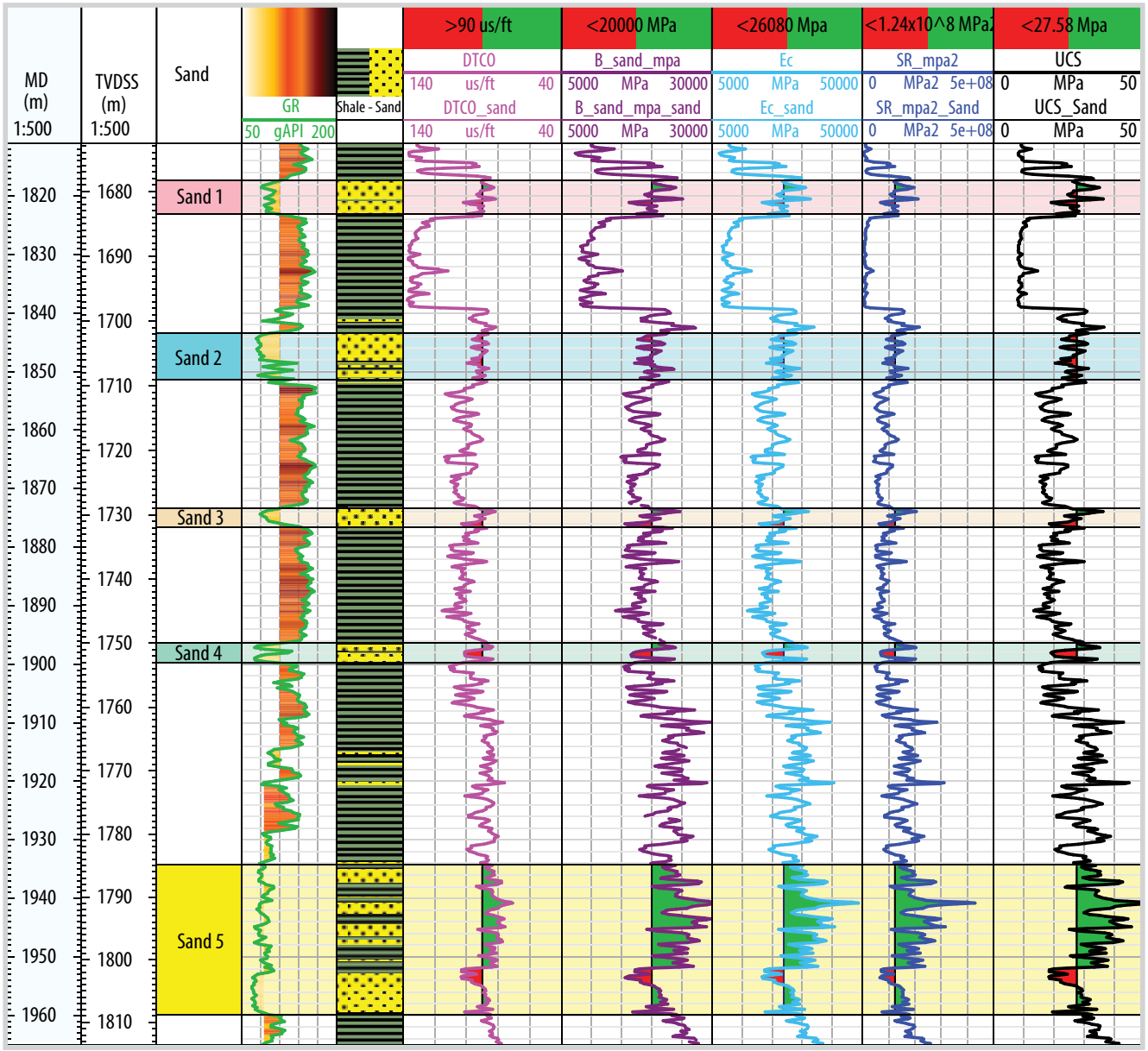

Figure 3. *Sand production indices.*

- Schlumberger sand production ratio (SR) analysis

Track 9 in Figure 3 highlights intervals where SR < 1.24×10^8 MPa^2 (red shading), indicating elevated sand production potential that requires control measures [6, 9]. Table 2 shows the average SR values for Sands 1 - 5, ranging from 1.22 to 1.82×10^8 MPa^2. Only Sand 5 exceeds the critical threshold, confirming lower sand production susceptibility compared to other intervals.

- Combined elastic modulus (E_c) analysis

According to multiple researchers [1, 4, 6, 9], formations with E_c below 26,080 MPa require sand control. Track 8 in Figure 3 displays intervals below this threshold in red, indicating higher sand production potential. Average E_c values range from 26,009 to 31,516 MPa across all intervals. Only Sand 3 falls below the critical value.

- Rock strength (UCS) analysis

Table 2 demonstrates that Sand 5 exhibits the highest UCS (32.69 MPa), exceeding the 27.58 MPa threshold, while all other intervals fall below this value. These results confirm that active sand control measures are required throughout the productive life of well for Sands 1 - 4.

Table 2 identifies specific depth intervals within each sand body that exhibit the highest sand production potential based on the integrated multi-index assessment. These intervals should be avoided during perforation planning if sand control equipment is not installed or given priority for active sand control implementation.

Table 2. High sand production risk intervals within sand bodies

No.	Sub-Interval	Depth (m)	Thick (m)	DTCO (µs/ft)	BI (MPa)	SR ($\times 10^8$ MPa^2)	Ec (MPa)	UCS (MPa)	Risk
	Threshold →			> 93	< 20,000	< 1.24	< 26,080	< 27.58	
1	Sand 1a	1,817 - 1,821	3.75	96.8	17,200	1.08	22,500	25.2	High
2	Sand 1b	1,821 - 1,823	2.06	94.5	18,800	1.15	24,200	26.8	High
3	Sand 2a	1,843 - 1,845	2.09	95.2	18,200	1.12	23,800	26.2	High
4	Sand 2b	1,845 - 1,847	2.00	97.5	16,800	1.05	21,900	24.8	High
5	Sand 2c	1,847 - 1,849	2.40	94.8	18,500	1.18	24,500	27.1	High
6	Sand 2d	1,849 - 1,851	1.50	93.5	19,200	1.20	25,200	28.2	High
7	Sand 3a	1,873 - 1,875	1.61	98.2	16,200	1.02	21,200	24.2	High
8	Sand 3b	1,875 - 1,876	1.62	97.8	16,500	1.04	21,500	24.5	High
9	Sand 4a	1,896 - 1,898	1.69	96.5	17,500	1.09	22,800	25.5	High
10	Sand 4b	1,898 - 1,899	1.73	94.2	18,900	1.16	24,800	27.2	High
11	Sand 5a	1,934 - 1,953	18.78	83.5	24,200	1.45	30,500	33.8	Low
12	Sand 5b	1,953 - 1,955	2.00	95.2	17,800	1.11	19,100	26.5	High
13	Sand 5c	1,955 - 1,959	4.95	93.8	21,500	1.18	22,800	31.2	Medium

4. Conclusions and recommendations

This study demonstrates that standard wireline log measurements can be used to derive key geomechanical parameters (Poisson's ratio, Young's modulus, bulk modulus, shear modulus) and rock strength (UCS). Five complementary prediction methodologies were applied: compressional sonic transit time, sand production index (BI), Schlumberger ratio (SR), combined elastic modulus (E_c), and UCS.

Analysis of five sand bodies in the study well reveals that Sands 1 - 4 exhibit high sand production potential, indicating the need for proactive completion design and sand control implementation prior to initial production. In contrast, Sand 5 shows the lowest sand production susceptibility. However, even in the absence of sand control measures, perforation of the high-risk depth intervals identified in Table 3 should be avoided to minimize sand production issues.

The integrated multi-index approach presented in this study offers several significant advantages:

- Cost-effectiveness: Reliance on routinely acquired wireline log data reduces dependence on expensive core acquisition and laboratory testing, shortening project timelines and lowering costs and.

- Enhanced coverage: Wireline logs provide continuous vertical coverage of production intervals, enabling comprehensive reservoir characterization.

- Improved reliability: The multi-index approach reduces uncertainty by achieving consensus among multiple independent prediction criteria, increasing reliability against single-method assessments.

- Regional applicability: The methodology can be readily extended to adjacent areas and analogous geological settings with similar formation characteristics, facilitating rapid field development planning.

While this study confirms the effectiveness of log-based sand production prediction, several areas warrant further investigation:

- Validation against production history: Systematic comparison of predictions with actual sand production rates and volumes from multiple wells would enable statistical validation and threshold calibration for the Cuu Long basin.

- Integration with core data: Where available, core-derived mechanical properties should be correlated with log-calculated values to assess accuracy and potentially develop basin-specific empirical corrections.

- Time-lapse assessment: Monitoring sand production evolution with reservoir depletion through periodic logging or downhole monitoring could reveal threshold changes and enable dynamic risk reassessment.

- Machine learning applications: With sufficient data volume, supervised learning algorithms could potentially optimize index weighting or discover additional predictive log signatures.

This integrated geomechanical approach provides a robust and cost-effective framework for sand production risk assessment in weakly consolidated formations. By

leveraging standard wireline log data through multiple complementary prediction indices, operators can make informed decisions regarding completion design, sand control strategy, and perforation planning, ultimately enhancing production efficiency and reducing operational risks in challenging reservoirs such as those encountered in the Cuu Long basin.

References

[1] T.J. Ajayi, O.Y. Adeogun, and Omeru, "Predicting sanding potential using empirical method in "Ebendo" field, Niger Delta, Nigeria", *Journal of Applied Sciences and Environmental Management*, Volume 26, Issue 9, pp. 1557 - 1564, 2022.

[2] Sadegh Asadi, Khalil Rahman, Hoanh V. Pham, Thao Le Minh, and Andy Butt, "Sand production assessment considering the reservoir geomechanics and water breakthrough", *The APPEA Journa*l, Volume 55, Issue 1, p. 215 - 224, 2015. DOI: 10.1071/aj14016.

[3] I.D.R. Bradford, J. Fuller, P.J. Thompson, and T.R. Walsgrove, "Benefits of assessing the solids production risk in a North Sea reservoir using elastoplastic modelling", *SPE/ISRM Rock Mechanics in Petroleum Engineering, Trondheim, Norway, 8 - 10 July 1998.* DOI: 10.2118/47360-MS.

[4] Ma Dong, Bian Long, Li Lun, and Hu Juncheng, "Application of logging data in predicting sand production in oilfield", *Electronic Journal of Geotechnical Engineering,* Volume 18, pp. 6173 - 6180, 2013.

[5] Ehsan Khamehchi and Ebrahim Reisi, "Sand production prediction using ratio of shear modulus to bulk compressibility (case study)", *Egyptian Journal of Petroleum*, Volume 24, Issue 2, pp. 113 - 118, 2015. DOI: 10.1016/j.ejpe.2015.05.002.

[6] Osaki Lawson-Jack, Etim D. Uko, Iyeneomie Tamunobereton-Ari, and Matthew A. Alabraba, "Geomechanical characterization of a reservoir in part of Niger Delta, Nigeria", *Asian Journal of Applied Sciences and Technology*, Volume 3, Issue 1, pp. 10 - 30, 2019.

[7] Khalil Rahman, Abbas Khaksar, and Toby Kayes, "Minimizing sanding risk by optimizing well and perforation trajectory using an integrated geomechanical and passive sand-control approach", *SPE Annual Technical Conference and Exhibition, Denver, Colorado, USA, 21 - 24 September 2008*. DOI: 10.2118/116633-MS.

[8] Surej Kumar Subbiah, Lex de Groot, and Hilbrand Graven, "An innovative approach for sand management with downhole validation", *SPE International Symposium and Exhibition on Formation Damage Control, Lafayette, Louisiana, USA, 26 - 28 February 2014*. DOI: 10.2118/168178-MS.

[9] Kingsley Maraizu Ogbuagu, Chukwuemeka Ngozi Ehirim, and Tamunonengiyeofori Dagogo, "Evaluation of formation susceptibility and sand production potential in an offshore field, Niger Delta basin, Nigeria", *Energy Geoscience*, Volume 5, Issue 1, 2024. DOI: 10.1016/j.engeos.2023.100213.

[10] S.M. Willson, Z.A. Moschovidis, J.R. Cameron, and I.D. Palmer, "New model for predicting the rate of sand production", *SPE/ISRM Rock Mechanics Conference, Irving, Texas, 20 - 23 October 2002*. DOI: 10.2118/78168-MS.

[11] Hoàng Thanh Tùng, Lê Thị Hoàng Thi, Trương Hoài Nam, Lê Vũ Quân, và Tạ Văn Cường, "Ứng dụng mô hình giải tích để dự báo khả năng sinh cát của các vỉa khí tầng miocene mỏ Hải Thạch, bể Nam Côn Sơn", *Tạp chí Dầu khí*, Số 12, trang 16 - 26, 2016.

[12] Tạ Quốc Dũng, Lê Thế Hà, và Nguyễn Tiến Đạt, "Ứng dụng phương pháp địa thống kê trong dự báo các thông số địa cơ học và ứng dụng mô hình SANDPIT3D trong dự báo sinh cát cho giếng khai thác ở bể Nam Côn Sơn", *Tạp chí Dầu khí*, Số 4, trang 39 - 50, 2019.

[13] Ta Quoc Dung, and Hoang Thanh Tung, "The model to predict sand production for production wells in the Cuu Long basin", *Journal of Science and Technology Development*, Volume 17, Issue 3, pp. 172 - 178, 2014. DOI: 10.32508/stdj.v17i3.1493.

[14] Tạ Quốc Dũng, và Hoàng Trọng Quang, *Nghiên cứu điều kiện sinh cát và thiết lập chương trình mô phỏng sinh cát trong các giếng khoan khai thác dầu tầng Miocene thềm lục địa Việt Nam*. Trung tâm Phát triển Khoa học Công nghệ trẻ, 2003.

[15] Per Horsrud, "Estimating mechanical properties of shale from empirical correlations", *SPE Drilling and Completion*, Volume 16, Issue 2, pp. 68 - 73, 2001. DOI: 10.2118/56017-PA.

[16] G.H. McNally, "Estimation of coal measures rock strength using sonic and neutron logs", *Geoexploration*, Volume 24, Issue 4 - 5, pp. 381 - 395, 1987. DOI: 10.1016/0016-7142(87)90008-1.

[17] Petronas, *HIIP and reserves assessment report,* 2013.

PETROVIETNAM
SCIENCE, TECHNOLOGY & INNOVATION PETROVIETNAM

AN EFFECTIVE ACID COMBINATION FOR IMPROVED ACIDIZING TREATMENT OF SANDSTONE FORMATION: A CASE STUDY IN BACH HO FIELD, VIETNAM

Luong Hai Linh[1], Nguyen Van Trung[1], Do Quang Khanh[1], Nguyen The Dung[2], Ho Nam Chung[2], Nguyen Van Hong[3]
[1]Petrovietnam University (PVU)
[2]Vietsovpetro Joint Venture (Vietsovpetro)
[3]Schlumberger Vietnam Services Co.
Email: linhlh@pvu.edu.vn
https://doi.org/10.47800/PVSI.2025.06-02

Summary

The acidizing treatment of near-wellbore regions in oil and gas reservoirs is a critical technique for enhancing permeability and boosting hydrocarbon recovery. However, the conventional hydrochloric acid (HCl)-based solutions often face challenges such as the formation of stable emulsions, secondary precipitation, and incompatibility with reservoir fluids. This study focuses on evaluating the performance of modified acid systems (CKP^+ and GKP^+) for acidizing sandstone formations in the Bach Ho field. The experiments aimed at assessing the efficiency of these acid systems in enhancing permeability, mitigating clay swelling, and preventing the formation of secondary precipitates. Experimental results, including shale stability tests, dissolution experiments on formation rock, and permeability recovery evaluations, indicated that the proposed chemical systems effectively reduced the skin factor, enhancing oil permeability and sustaining recovery rates. The addition of anti-emulsifying agents and clay stabilizers improved the acid systems' compatibility with crude oil, reducing emulsion formation. Furthermore, the modified acid systems showed promising results in preventing iron-related precipitation, a common issue with conventional acid systems. Simulations conducted using Schlumberger's Kinetix Matrix software demonstrated that the proposed acid treatments could efficiently remove formation damage, especially in Miocene and Oligocene reservoirs, where traditional treatments had limitations. Overall, the study suggests that the CKP^+ and GKP^+ systems provide a cost-effective solution for improving well productivity and sustaining long-term hydrocarbon recovery.

Key words: Acid treatment, sandstone formation, Bach Ho field, formation damage, high clay content.

1. Introduction

Throughout the operations involved in oil and gas, including drilling, cementing, well completion, perforation, workover, and water injection, a series of events may occur near the wellbore formation, leading to changes in its natural physical and chemical properties. The impact of these events leads to a decline in permeability, resulting in reduced production efficiency in production wells and injection efficiency in injection wells. This decrease in permeability around the wellbore, as previously mentioned, is referred to as formation damage [1].

Date of receipt: 16/5/2025
Date of review and editing: 16/5 - 15/7/2025
Date of approval: 15/7/2025

The acidizing treatment of the near-wellbore region is a widely applied stimulation technique in the petroleum industry. It is particularly effective in restoring or enhancing the productivity of wells impaired by formation damage caused by factors such as drilling fluid invasion, scale deposition, or fines migration. The process involves injecting acid solutions - typically hydrochloric acid or blended organic/inorganic systems - into the near-wellbore formation to dissolve obstructive materials, clean pore spaces and natural fractures, thereby improving permeability and flow efficiency toward the wellbore. Compared to alternative methods such as hydraulic fracturing or mechanical wellbore cleaning, acidizing offers several advantages, including lower operational costs, shorter treatment durations, and broad applicability across various lithologies. Additionally,

acidizing minimizes secondary formation damage and can be repeated multiple times throughout the well's production life, making it an efficient and cost-effective method for enhancing hydrocarbon recovery.

Recent advances in sandstone acidizing encompass the offshore application of GLDA chelating-acid systems, the development of aluminum-based retarded mud acids, and comprehensive reviews of acidizing mechanisms and workflows to optimize treatment design. Nars-El-Din et al. [2] presented the first offshore field application of a 25 wt% GLDA (glutamic acid N,N-diacetic) chelating-acid system in a sour (H_2S/CO_2) sandstone reservoir. After a xylene pre-flush, the GLDA solution - containing corrosion inhibitor and surfactant - was injected and allowed to soak for 6 hours before flowback. Field measurements showed exceptionally low casing corrosion (0.0023 lbm/ft^2), no formation of filter cake or fines migration, and ~88% chelant recovery. The GLDA treatment dissolved carbonate, oxide, and sulfide scales without secondary precipitation. Over the subsequent 60 days, oil production increased by 2,307 barrels, and the stimulation effect persisted for nearly 6 months - substantially longer than conventional mud-acid treatments. These results demonstrate that GLDA offers a low-corrosion, environmentally friendly alternative for sandstone acidizing in sour environments. Qin Ji et al. [3] evaluated the performance and mechanism of an aluminum-based retarded mud acid (15 wt% HCl, 1.5 wt% HF, 5 wt% $AlCl_3{\cdot}6H_2O$) for sandstone stimulation, compared to conventional mud acid (15 wt% HCl, 1.5 wt% HF). Batch solubility tests with kaolinite, bentonite, and illite at 75°F and 200°F, analyzed by ICP, SEM/EDS, and 19F NMR, demonstrate that $AlCl_3$ retards HF reaction (via AlF_4^- complexation) without forming AlF_3 precipitates, maintaining low free-F^- concentration and reducing secondary silica-gel formation. Core-flood experiments on Berea sandstone at 75, 200, and 300°F show deeper acid penetration (by CT imaging) and greater permeability enhancement (up to +212% at 75°F) with the retarded system, although the retardation efficacy diminishes at higher temperatures. These findings confirm that Al-based retarded mud acid offers controlled HF release, minimized formation damage, and improved stimulation depth. Shafiq and Mahmud [4] provided a comprehensive review of sandstone matrix acidizing, detailing the chemical mechanisms, treatment workflows, and performance of various acid systems under reservoir conditions. The review identifies critical future needs: development of economically viable, high-temperature-stable acids; expanded experimental data on heterogeneous sandstones; and deployment of pore-scale imaging to elucidate dissolution morphology and optimize stimulation design.

Based on numerous studies, the primary challenges commonly encountered during acid treatment of consolidated sandstone formations include limited penetration depth, secondary precipitation, elevated temperatures, and corrosion issues [5]. To identify factors that sustain treatment effectiveness in Miocene, Oligocene, and Upper Oligocene formations of Bach Ho field, this study will apply a synthesis and analysis approach, investigating the near-wellbore treatment data from 1988 to 2022.

Research has identified several challenges encountered during acid treatment of consolidated sandstone formations, including limited penetration depth, secondary precipitation, elevated temperatures, and corrosion issues [5]. This study aims to examine the factors that sustain treatment effectiveness in the Miocene, Oligocene, and Upper Oligocene formations of the Bach Ho field, analyzing near-wellbore treatment data from 1988 to 2022.

Between 1988 and 1999 [6], insufficient data for evaluating treatment effectiveness led to categorizing treatments into two groups: acid emulsion and acid solution. The acid emulsion method involves emulsifying acid solutions with oil phases such as diesel oil, crude oil, and acid microemulsions containing organic solvents and co-solvents [7]. The acid solution group includes hydrochloric acid, mud acid, polymer acid, and acid foam. Data from this period indicated that acidizing in clastic formations shows more significant challenges than in basement formations, emphasizing the need for further research to optimize acid systems [8].

From 2000 to 2022, the success of acid treatments was influenced by various factors, including reservoir geology, wellbore completion characteristics, acid composition, and the type of formation damage. Acid systems such as emulsified acid, hydrochloric acid (CKP), and mud acid (GKP) had notable impacts on clastic reservoirs in the Bach Ho field. Data analysis showed no significant difference in effectiveness between the conventional hydrochloric acid, mud acid, and acid emulsion systems between 2005 and 2007. However, after 2009, a decline in the efficiency of conventional hydrochloric acid and mud acid stimulation techniques was observed.

Table 1. *Composition of acid systems used in the experiment*

No.	Solution	Composition (%)				
		HCl	HF	CH_3COOH	NTF	PAV
1	Hydrochloric acid	12	-	4	1.5	1.5
2	Mud acid	12	1.5	4	1.5	1.5

From 2000 to 2010, the acid emulsion system yielded positive results for clastic formations in the Lower Miocene, Upper Oligocene, and Lower Oligocene. Success rates remained high, typically ranging from 60% to 100%, with the lowest recorded rate being around 59% in 2004. The success rate was notably stable, remaining at approximately 80% for 6 consecutive years (2005 - 2010). However, after 2010, the use of acid emulsion was discontinued due to safety concerns [9 - 13].

Comparing the success rates of acid emulsion systems with hydrochloric acid and mud acid systems from 2005 to 2010, the emulsion systems were found to have a positive impact on clastic formations in the Bach Ho field. This suggests that organic contaminations (e.g., asphaltene, resin, oil/water emulsion, and water/oil emulsion) play a significant role, and addressing only inorganic contaminations is insufficient. Overall, the analysis indicates a decline in the effectiveness of hydrochloric and mud acid systems after 2011, primarily due to changes in the composition and concentration of acids and additives, which warrants further investigation to align with current field conditions.

2. Methodology

In this study, we initially conducted a series of experiments to evaluate the performance of the conventional acid solution used for acidizing treatment on sandstone formations, specifically focusing on the formation of emulsions, precipitation, and the potential for scaling. The results from these preliminary tests provided insights into the limitations and areas for improvement in the existing acid systems. The experiments focused on the acids that were currently being used at the Bach Ho field, including hydrochloric acid and mud acid, with the compositions provided in Table 1. This is the average composition of the acid systems as per the usage instructions for the Bach Ho field.

The crude oil used for the study was from Well 1 and Well 2. These two wells have experienced a decrease in production in recent years, following near-wellbore treatment, indicating poor treatment effectiveness. The incompatibility of reservoir oil with chemical systems is evident through two aspects and phenomena: (1) the formation of high-viscosity stable emulsions and (2) the formation of slugs, chemically composed of precipitates of asphaltene, resin, and high molecular weight paraffin [14 - 16].

Subsequently, based on the findings from the conventional acid experiments and widely accepted worldwide guidelines for acid selection in sandstone formations [1, 17], we developed a modified acid system. These guidelines are used by major companies such as Schlumberger, BJ, and Halliburton. The modified system was developed by adjusting the acid composition and the concentration of individual components. The authors analyzed the following criteria: permeability variation range, temperature range of the formation to be treated, mineral composition (quartz, feldspar, and clay mineral content), solubility of the formation rock in 15% HCl solution, and siltstone content. Based on analysis results, the authors proposed the optimal composition of the pre-flush acid and the main acid solution for the Lower Miocene, Upper Oligocene and Lower Oligocene formations in the Bach Ho field, as shown in Tables 2 and 3. This new formulation (CKP^+ and GKP^+) was designed to enhance compatibility with the formation fluids while minimizing undesired reactions such as precipitation or emulsion formation. The modified acid system underwent comprehensive testing, including shale stability evaluation, compatibility tests with formation fluids, thermal stability assessments, dissolution experiments on formation rock samples, permeability recovery tests, and corrosion evaluations. These tests aimed to ensure the stability and efficiency of the chemical system under the operational conditions of the Bach Ho field. The acid composition used in the corrosion test is shown in Table 4.

To improve compatibility, prevent secondary precipitation, and mitigate the formation of high-viscosity stable emulsions, the authors proposed using additional anti-sludge and anti-emulsion additives. In addition, the ability to inhibit swelling and stabilize clay was improved by using a clay stabilizer.

The emulsifier-breaking additives and clay stabilizers in the modified acid systems (CKP+ and GKP+) play a crucial role in enhancing the compatibility of the acid solutions with crude oil and preventing the formation of persistent emulsions. Specifically, the non-emulsifying agents help to reduce the crude oil and acid to emulsify, thereby inhibiting the stable emulsion creation that could otherwise cause flow restrictions. Mechanistically, these additives alter the surface properties of the acid, oil, clay interactions and the interfacial tension, thereby preventing both emulsion formation and secondary precipitation.

Finally, a Kinetix Matrix simulation was performed to model the acid injection process and its effect on skin factor changes throughout the acidizing treatment. Reservoir parameters used in simulation are shown in Table 5.

3. Result and discussion

3.1. Performance of the current acids

3.1.1. Stable emulsion capability

First, mixtures of Well 1 crude oil and acid solution were prepared to a total oil-acid volume of 25 ml and heated at 70°C for 2 hours to ensure homogenization. Each mixture was then blended with one of two acid formulations (hydrochloric "CKP" or mud-acid "GKP") at acid-to-oil volume ratios of 25:75, 50:50, and 75:25. The blends were vigorously shaken to form uniform emulsions and subsequently placed to a thermostatted bath maintained at 80°C. At defined intervals, and again after 2 hours or upon complete phase separation, the volumes of oil, water and emulsion layers were recorded. Thereafter, each sample was passed through a 100-mesh screen; any retentate was rinsed with 80°C water until completely passed. An acid system was deemed compatible if, after thermal treatment, it exhibited fully separated oil-water layers with a sharp interface and left no residue on the screen. In contrast, incomplete separation after 2 hours at 80°C and persistent screen blockage (indicative of stable, large-droplet emulsions) signified acid-oil incompatibility, with attendant risks of pore plugging and permeability impairment. Tables 6 and 7 summarize the emulsification capacities observed for CKP and GKP, respectively.

The results indicate that both the hydrochloric acid

Table 2. *Composition of the pre-flush acid solution*

No.	Chemical	Concentration (%)	Function
1	HCl	6 - 10	Dissolves inorganic contamination
2	CH_3COOH	5	Creates a buffering effect to keep pH at low level
3	Clay stabilizer	2	Inhibits clay swelling
4	Anti-sludge agent	1 - 2	Prevents the sludge formation
5	Interactive solvents	2	Improves quickly flow back to the well after treatment.
6	Anti-emulsifying agent	2	Prevents emulsion formation during treatment
7	Surfactant	5	Increases the contact of chemicals with the formation rock
8	Corrosion inhibitors	3 - 5	Inhibits, reduces corrosion
9	Water	Remaining	Dispersion medium

Table 3. *Composition of GKP+*

No.	Chemical	Concentration (%)	Function
1	HCl	6 - 10	Dissolves inorganic contamination
2	HF	0.5 - 1	Dissolves inorganic contamination
3	CH_3COOH	5	Creates buffering effect to keep pH at low level
4	Clay stabilizer	2	Inhibits clay swelling
5	Anti-sludge agent	1 - 2	Prevents the sludge formation
6	Interactive solvents	2	Improves quickly flow back to the well after treatment.
7	Anti-emulsifying agent	2	Prevents emulsion formation during treatment
8	Surfactant	5	Increases the contact of chemicals with the formation rock
9	Corrosion inhibitors	3 - 5	Inhibits, reduces corrosion
10	Water	Remaining	Dispersion medium

Table 4. *Composition of acid in corrosion test*

No.	Acid	Composition
1	CKP^+	HCl 8% + CH_3COOH 5% + Non-emulsifier 5% + Surfactant 2% + CS-1/CS-2 (2%) + Mutual solvent + CI-31 + Non-sludge 2%
2	GKP^+	HCl 8% + HF 0.5% + CH_3COOH 5% + Non-emulsifier 5% + Surfactant 2% + CS-1/CS-2 (2%) + Mutual solvent + CI-31 + Non-sludge 2%

Table 5. *Reservoir parameters*

No.	Parameter	Value	Unit
1	Reservoir pressure	148.898	atm
2	Productivity index	1.9	$m^3/d/atm$
3	Permeability	89.4	mD
4	Skin factor	+9.8	
5	Reservoir temperature	90	°C
6	Water cut	2 - 5	%
7	Oil rate	95	m^3/d
8	GOR	60	m^3/m^3
9	Gas density	0.72	
10	Oil density	0.8519	
11	Water density	1.02	
12	Pipe diameter	73	mm
13	Wellhead pressure	26	atm
14	Gas lift pressure	88	atm
15	Gas lift rate	25000	m^3/d

Table 6. *Results of emulsion and slug formation of CKP acid system with Well 1 crude oil*

No.	Acid/oil ratio	Phase	Emulsion state during sample storage time (%)				Note
			0 min	5 min	15 min	120 min	
1	25/75	Water	0	0	0	0	Whole was emulsion
		Emulsion	25	25	25	25	
		Oil	0	0	0	0	
2	50/50	Water	0	14.5	14.5	14.5	Separation part was water and emulsion
		Emulsion	25	10.5	10.5	10.5	
		Oil	0	0	0	0	
3	75/25	Water	0	18,5	18,5	18.5	Separated into 3 layers
		Emulsion	25	2,5	2,5	2.5	
		Oil	0	4	4	4	
Other observations: The CKP acid system was generally incompatible with crude oil from Well 1. When the acid contacted the oil, it formed a stable emulsion (25:75 ratio) or an incomplete emulsion, with a portion remaining as emulsion. The emulsion had high viscosity and could not pass through a 100-mesh screen (Figure 1).							

and mud acid systems currently used at the Bach Ho field are incompatible with the crude oil from Well 1. Notably, with a water phase ratio of 50%, the formed emulsion remains stable without separation.

The crude oil from Well 2 was generally compatible with the hydrochloric acid system, except at an acid-to-oil ratio of 25:75. However, this oil was incompatible with the mud acid system, as it tended to form slugs.

3.1.2. Slug formation capability

To evaluate the slug-formation tendencies of the acid system, 1000 ppm Fe^{3+} was added to the test acid solution and then mixed with the crude oil sample at a 1:1 volumetric ratio. The mixture was shaken vigorously to form a uniform emulsion, then placed in a thermostated bath at 80°C for 2 hours. After equilibration, the emulsion was poured through a 100-mesh screen and inspected. If

Figure. 1. *Images of samples (CKP acid and Well 1 crude oil mixture with different volume ratios) after passing through a 100-mesh screen.*

Table 7. *Results of emulsion and slug formation of GKP acid system with Well 1 crude oil*

No.	Acid/oil ratio	Phase	Emulsion state during sample storage time (%)				Note
			0 min	5 min	15 min	120 min	
1	25/75	Water	0	0	0	0	Whole is emulsion
		Emulsion	25	25	25	25	
		Oil	0	0	0	0	
2	50/50	Water	0	1.5	1.5	1.5	Mainly in emulsion
		Emulsion	25	23.5	23.5	23.5	
		Oil	0	0	0	0	
3	75/25	Water	0	18.5	18.5	18.5	Partly water, oil in emulsion form
		Emulsion	25	3.5	3.5	3.5	
		Oil	0	3.0	3.0	3.0	
Other observations: The GKP acid system was generally incompatible with crude oil from Well 1. At a water phase ratio of 50%, the formed emulsion was stable and did not separate. However, with a water phase ratio greater than 50%, phase separation occurred but was incomplete. The emulsion exhibited high viscosity and could not pass through a 100-mesh screen (Figure 2).							

Figure 2. *Images of samples (GKP acid and Well 1 crude oil mixture with different volume ratios) after passing through a 100-mesh screen.*

the oil phase did not fully pass through, the residue was rinsed with 80°C hot water. The acid system was deemed non-depositing if, after thermal treatment, complete phase separation occurred, and no solids remained on the sieve.

During the slug-formation test with the Fe-containing acid and crude oils from Wells 1 and 2, phase separation occurred, but a significant precipitate formed. Consequently, the separated oil phase could not pass

Figure. 3. *Images of precipitation and slug formation when CKP and GKP acid mixed with crude oil.*

through the 100-mesh screen (Figure 3), indicating deposit formation under these conditions.

Therefore, the acid systems currently used at the Bach Ho field pose a risk of forming stable emulsions with high viscosity when interacting with crude oil from the existing wells. The acid system itself, when contaminated with Fe (from pipeline and wellbore equipment corrosion products exposed to the acid solution), forms precipitates and slugs upon interaction with crude oil. These issues must be addressed during the optimization of the acid system composition.

3.1.3. Precipitation capability

To evaluate the capability of hydrochloric acid (CKP) and mud acid (GKP) systems to prevent secondary iron gel precipitation, Fe^{3+} at concentrations of 50 - 5,000 ppm was added to the acid solutions. Immediately following Fe^{3+} addition, both hydrochloric acid and mud acid solutions became cloudy and precipitated a white substance (Figure 4). This is a concerning signal, as in actual treatments, during pumping from the surface to the near-bottomhole zone, acid solutions dissolve and absorb steel corrosion products, creating Fe ions. These Fe ions can precipitate rapidly in the acid solution, leading to increased secondary precipitate formation, which could lead to near-bottomhole plugging.

Additional investigations of precipitation capability were carried out using a porous core model composed of reservoir rock and a reservoir model apparatus. Tests on Miocene rock samples from Well 3 and Well 4 showed that the post-treatment solution turned turbid and formed precipitates after being left undisturbed for a certain period.

A similar experiment was conducted to examine the precipitation potential of hydrochloric and mud acid as they flowed through a core sample. A reservoir model apparatus was used to analyze the resultant solution, with a core sample from Well 5 chosen for evaluation. Hydrochloric acid and mud acid were injected into the sample, and the resulting solution was allowed to settle undisturbed to observe any precipitation. The results showed the formation of a white precipitate in the post-reaction solution. The permeability recovery factor outcomes are detailed in Table 8.

To demonstrate the plugging ability of the precipitate, an experiment was conducted using the mud acid system with an additional 1,000 ppm Fe (specific composition: HCl 12% + CH_3COOH 4% + HF 1.5% + NTF 2% + 1,000 ppm Fe). The solution and precipitate were poured through a 100-mesh screen, and a large amount of precipitate was observed on the screen. This indicates that the precipitate size is >100 µm, capable of plugging sandstone pores.

Images of the precipitates obtained from the mud acid mixture with different Fe concentrations (500, 1,000, and 2,000 ppm) after drying are shown in Figure 5. These precipitates are NTF-iron complexes. Our findings align with the research in [18], which confirmed that NTF-iron complexes are poorly soluble. To improve the effect of NTF

Table 8. *Result of permeability recovery factor determination*

No.	Sample information	
1	Sample	Sample 1
2	Reservoir	Miocene
3	Gas permeability, (mD)	40.9
4	Temperature,(^{0}C)	115
5	Pressure, (atm)	100
6	Initial oil permeability K_1, (mD)	6.102
7	Chemical solution	CKP*
8	Oil permeability after treatment K_2, (mD)	5.956
9	Permeability recovery factor $K_{re} = K_2/K_1 \times 100\%$	99%
*CKP: HCl 6% + CH_3COOH 5% + NTF 4% + HF 1.5% + WCI-1212 1.25% + WHT 8213 3.75% + 1% PAV 2% + OS-802 100 g/m^3		

in the presence of iron, Shuchart and Gdanski [18] investigated adding the compound GLDA (L-glutamic acid diacetic acid) to NTF.

In conclusion, the studies presented in this section demonstrate that the hydrochloric acid and mud acid systems currently used at the Bach Ho field have limited secondary precipitation prevention capacity. These systems require further examination and improvement to meet new operational conditions.

3.2. Performance of the modified acids

3.2.1. Shale stability

HCl-based acid systems lack the ability to prevent clay-swelling and may even induce clay-gel formation, thereby reducing permeability in formations containing HCl-sensitive clays, especially at lower temperatures. To overcome this limitation, two organic quaternary-amine stabilizers, CS-1 and CS-2, were evaluated. Both are colorless to pale-yellow viscous liquids, stable and low-toxicity in acidic environments, and effective from acidic to near-neutral pH [19, 20]. At 0.02 - 0.05 wt%, they outperform conventional NH_4Cl/KCl brines in enhancing shale stability, minimizing particle migration, and preventing pore blockage by fine clay fragments. These products are analogous to industry standards such as Halliburton's Cla-Sta FS, Schlumberger's L055, and Baker Hughes' Claytreat-3C and Claymaster-10.

CS-1 and CS-2 adsorb onto clay surfaces via electrostatic attraction: their positively

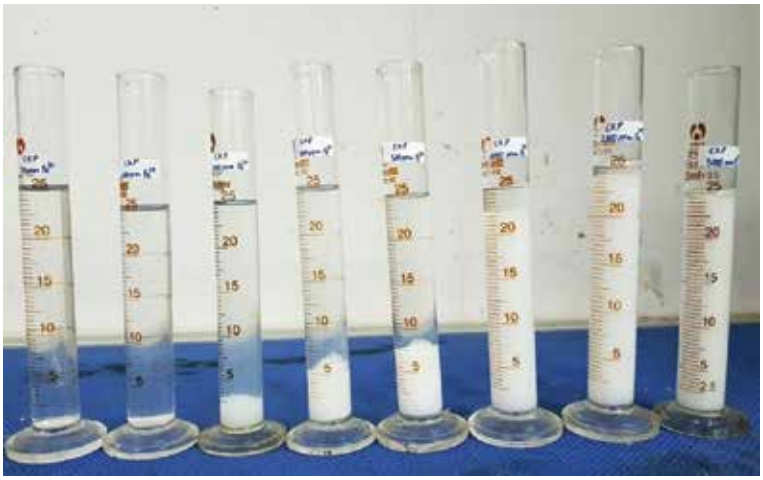

Figure. 4. *Images of precipitation when adding Fe^{3+} to CKP acid.*

Figure 5. *Images of the precipitates obtained from the mud acid mixture with different Fe contents.*

charged functional groups bind to negatively charged clay platelets, forming a hydrophobic adsorption layer that impedes water ingress and suppresses clay swelling. Adsorption increases the clay's surface potential; this was confirmed by zeta-potential measurements on clay suspensions treated with CS-1 at 0.02% and 0.05%, which showed a marked rise in surface charge. Moreover, the polymeric nature of CS-1 provides interparticle bridging, as its cationic repeat

Table 9. *Results of evaluating the compatibility of the proposed acid with crude oil from Well 1*

Time (min)	Emulsion separation	
	CKP^+	GKP^+
5	Completely soluble, no precipitation	Completely soluble, no precipitation
10	Completely soluble, no precipitation	Completely soluble, no precipitation
30	Completely soluble, no precipitation	Completely soluble, no precipitation

units link adjacent clay particles, preventing detachment and migration of fine grains that could otherwise plug pore throats.

The inhibitory effectiveness of CS-1 and CS-2 on shale from Formation X was quantified using laboratory swell-meter tests. Both stabilizers at 0.02 - 0.05% yielded superior suppression of shale expansion compared to brines containing 8% KCl or 5% NH_4Cl (Figure 6). In drilling practice, KCl is typically dosed at 80 - 120 kg/m^3 in formulations such as KCl/PHPA/Glycol or Ultradril® (MI Swaco) to protect shale, but protection often wanes after one day. In contrast, CS-1 and CS-2 deliver prolonged inhibition, effectively preventing shale swelling over extended periods at low concentrations.

3.2.2. Chemical system compatibility with formation fluid

Compatibility was assessed at 80°C using CKP^+ and GKP^+ acid formulations - each containing a non-emulsifier, clay stabilizer, surfactant and scale inhibitor - and formation fluids comprising crude oil from Wells 1 and 2 of the Bach Ho field, seawater, and completion brine (25.7% $CaCl_2$, 1.23 g/cm^3; 24% NaCl, 1.18 g/cm^3). Systems were deemed compatible if they either fully dissolved to yield a homogeneous single phase (in miscible cases) or completely separated without secondary precipitate formation (in immiscible cases). Results for Well 1 (Table 9, Figure 7) and Well 2 were equivalent, confirming that CKP^+ and GKP^+ are fully compatible with the tested formation fluids, with no precipitates or emulsions observed.

3.2.3. Thermal stability

Thermal stability was evaluated by heating CKP^+ and GKP^+ acid solutions in transparent, heat-resistant vials at 2 - 3°C/min in an oven. At every 10°C increment, up to a final temperature of 120°C, the samples were held for 10 - 15 min and visually inspected. After 120 min at 90°C, both formulations remained clear and homogeneous, with no phase separation or precipitation; identical behavior was observed at 125°C and 130°C. These results demonstrate that CKP^+ and GKP^+ retain thermal stability under the tested conditions.

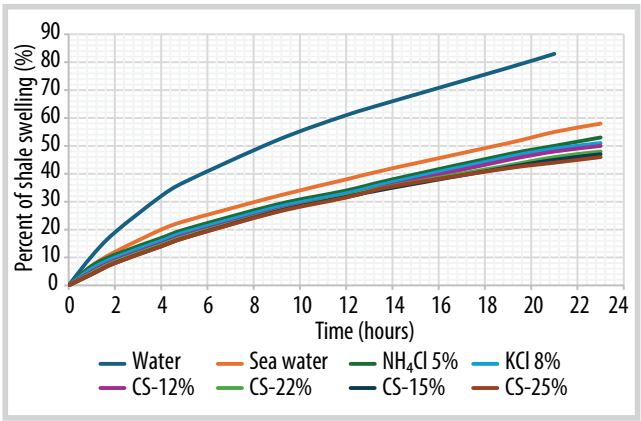

Figure 6. *Effects of salt on clay swelling.*

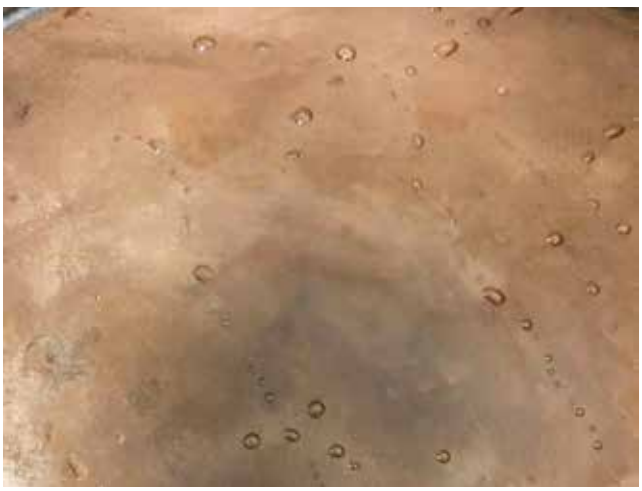

Figure 7. *Images of samples after passing through a 100-mesh screen.*

3.2.4. Dissolution experiment on formation rock

Consolidated sandstone from the Bach Ho field (18 g each from the Lower Miocene and Lower Oligocene) was characterized for composition and mineralogy, then exposed to the CKP^+/GKP^+ acid systems. Pre-experimental analyses established baseline chemical and mineralogical profiles. Table 10 reports that the mass percentage dissolved after drying. Dissolution tests showed that the acid blend attacked less than 6% of the rock, confirming minimal degradation of the cementing matrix and preserving the integrity of loosely consolidated Lower Miocene sands.

3.2.5. Permeability recovery experiments

Global service-provider guidelines correlate treatment efficacy with acid volume per meter of perforation. Optimal stimulation requires > 1.55 m^3/m (125 gal/ft), while near-wellbore cleanup typically uses 0.31 - 0.93 m^3/m (25 - 75 gal/ft).

Core-flood experiments to evaluate permeability recovery were conducted on Lower Miocene and Lower Oligocene cores using the following protocol. First, each core was oil-saturated by injecting five pore volumes (PV) of crude oil in the forward direction, and the initial permeability (K_1) was measured. Inorganic damage was then induced by sequentially injecting one PV of Solution A (5 g/l $CaCl_2$ + 5 g/l $FeCl_3 \cdot 6H_2O$) followed by one PV of Solution B (5 g/l Na_2CO_3 + 2.5 g/l Na_2SO_4 + 2.5 g/l NaOH) or until effluent precipitation occurred. After aging under reservoir conditions for 1 - 2 hours, three PV of viscous oil were forward-flooded to determine post-damage permeability (K_2). Acid treatment was performed in reverse flow by injecting one PV of NH_4Cl brine, one PV of pre-flush acid, and one PV of the main acid formulation. Finally, three PV of viscous oil were injected forward to measure the treated permeability (K_3). The permeability-recovery factor (K_3/K_1) was calculated to assess the effectiveness of the proposed chemical system (Table 11).

Based on the results obtained, it is evident that:

- All simulations of formation damage yielded reduced permeability, sometimes markedly, confirming that the experimental protocol successfully reproduced damage mechanisms such as $Fe(OH)_3$, $CaCO_3$, and $CaSO_3$ precipitation.

- Treatment efficacy was evaluated by comparing permeability before damage (K_1) and after acid remediation (K_3). A K_3/K_1 ratio ≥ 0.9 denotes effective removal of both primary and secondary damage.

Core-flood results demonstrate that the proposed acid systems not only restore permeability but also inhibit clay swelling, yielding high recovery factors and confirming their suitability for damage remediation.

3.2.6. Corrosion test

The authors investigated the corrosion performance of the chemical system, comparing it to the corrosion inhibitor CI-31 currently used in the acid treatment process at Field X, provided by Baker Hughes. To assess

Table 10. *Results of sample dissolution experiments*

No.	Chemical system	Initial sample mass	Sample mass after reaction	Percent of sample dissolved	
		g	g	90°C	120°C
1	GKP^+ = 10:1	9.003	8.892	1.2	
2	GKP^+ = 10:1	9.001	8.516	5.4	
3	GKP^+ = 10:1	9.002	8.900		1.1
4	GKP^+ = 10:1	9.003	8.937		0.7

Table 11. *Results of evaluating the permeability recovery*

No.	Sample information		
1	Sample	Sample 1	Sample 2
2	Reservoir	Oligocene	Miocene
3	Gas permeability (mD)	21.78	218.64
4	Temperature (°C)	100	100
5	Pressure, atm	100	100
6	Initial oil permeability, K_1 (mD)	3.22	40.22
7	Oil permeability after simulating contamination K_2 (mD)	2.19	29.14
8	Pump order	NH_4Cl 5%: $1V_0$	NH_4Cl 5%: $1V_0$
		Acid CKP^+: $1V_0$	Acid CKP^+: $1V_0$
		Acid GKP^+: $2V_0$	Acid GKP^+: $2V_0$
		NH_4Cl 5% - $1V_0$	NH_4Cl 5% - $1V_0$
9	Oil permeability after treatment K_3 (mD)	4.2	65.56
10	Permeability recovery factor K_{re}	**155.27**	**191.94**

corrosion characteristics under conditions resembling those of the formation, the "HP-HT Corrosion Cell" was used, maintaining conditions at 120°C and 100 atm for 4 hours, in accordance with ASTM standards (ASTM G1-03; ASTM G3-72) using the mass loss method. The evaluation results are displayed in Table 12.

The corrosion evaluation results demonstrate that the proposed chemical systems featuring corrosion inhibitor CI-31 show diminished corrosion rates compared to the present acid system utilized in Bach Ho field. Furthermore, these outcomes satisfy the criteria of maintaining a corrosion rate below 10 mm/year.

3.2.7. Simulation

Well X-1ST began production via gas lift in the Miocene reservoir on September 1, 2021, with an initial output of 89 tons per day from zones at depths ranging between 2,760 - 2,803 m and 2,848 - 2,920 m within the Bach Ho field.

The authors used Schlumberger - Techlog Kinetix Matrix software to formulate the treatment pumping schedule, simulate the treatment procedure for individual layers (Figure 8), evaluate each solution during treatment, and monitor real-time variation in the skin factor throughout the treatment (Figure 9).

Table 12. *Corrosion test results*

Sample	Mass - before (g)	Mass - after (g)	Mass loss (g)	Corrosion rate (mm/year)
CKP$^+$				
1	353.005	352.695	0.3100	3.2738
2	343.923	343.611	0.3120	3.2918
3	347.543	347.031	0.5120	5.4044
Average				**3.9900**
GKP$^+$				
1	349.215	348.803	0.4120	4.3504
2	350.147	349.529	0.6180	6.5253
3	361.123	360.522	0.6012	6.3434
Average				**5.7397**
Acid being used for Bach Ho field				
1	GKP			**7.60**
2	CKP			**6.02**

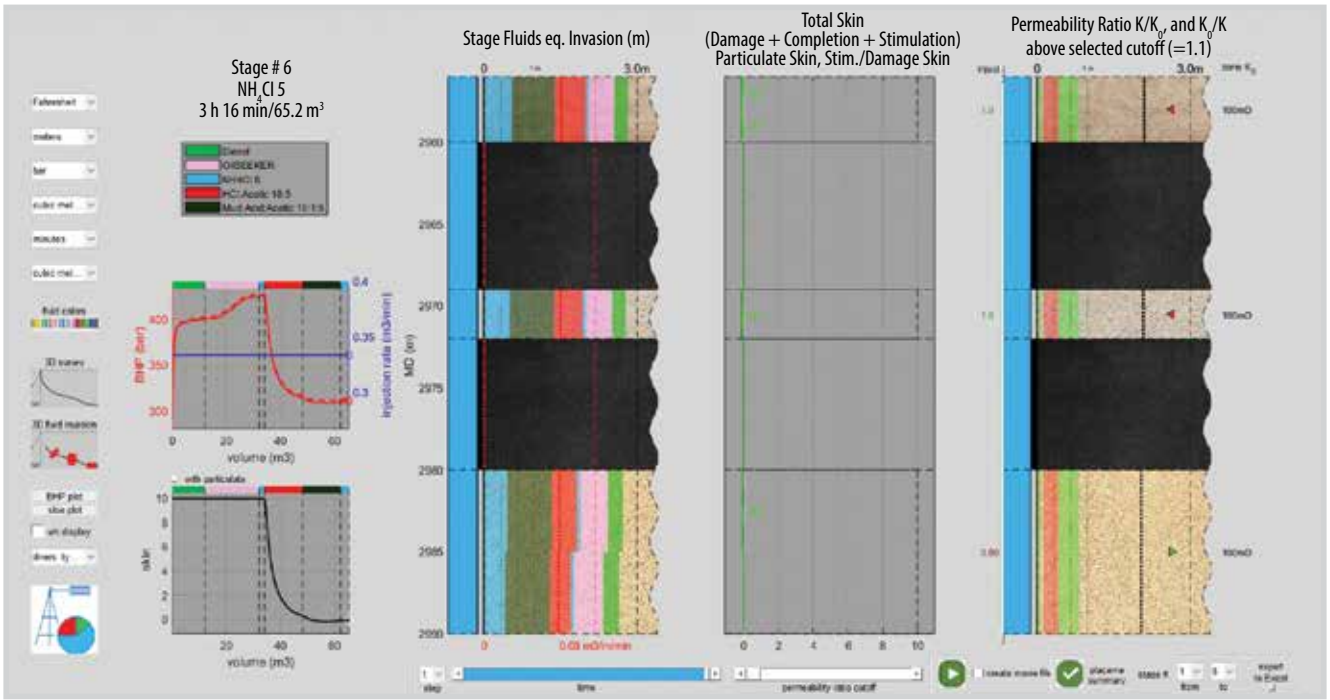

Figure 8. *Treatment process simulation for each layer.*

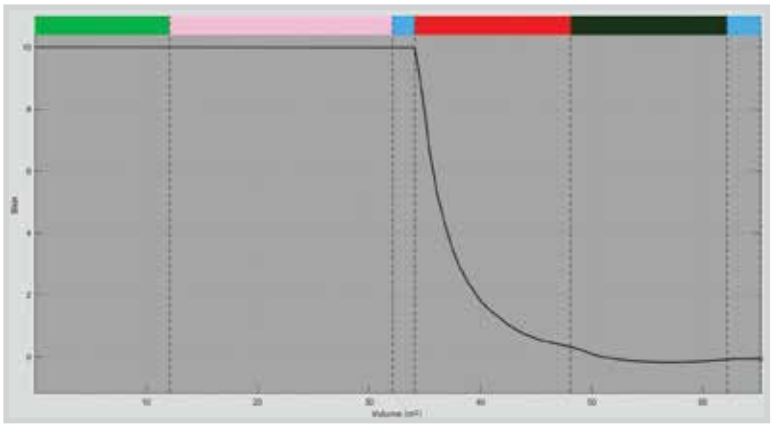

Figure 9. *Real-time variation in the skin factor throughout the treatment.*

The simulation results indicate that the acid system effectively dissolves inorganic scale and infiltrates fine particles from the formation into the near-wellbore area. Specifically, for Well X-1ST, the CKP^+ and GKP^+ acid systems proposed in this study, consisting of 8% HCl, 0.5% HF, and additional additives, show effective fouling dissolution within the well. As a result, the skin factor gradually decreased during the simulation, from 9.8 to 0, after treatment with the proposed acid system.

4. Conclusion

In conclusion, the modified acid systems, CKP^+ and GKP^+, exhibit significant advantages over conventional acidizing methods in the Bach Ho field. The results from the laboratory experiments and simulations confirm that these systems address common issues such as emulsion formation, clay swelling, and secondary precipitation. The introduction of clay stabilizers and anti-emulsifiers in the acid formulations has enhanced compatibility with crude oil and mitigated the formation of undesirable emulsions. Moreover, the dissolution experiments and permeability recovery tests have proven that these systems can effectively remove formation damage and restore permeability, especially in formations with high clay content. The simulation results highlight the promising potential of these acid systems in reducing the skin factor, improving hydrocarbon recovery, and ensuring stability under high-temperature and high-pressure conditions. These findings provide valuable insights into the design of more effective acid treatments for challenging reservoirs, offering both economic and operational benefits. Further optimization and field trials will be essential to fully understand the long-term performance of these systems in different geological settings.

References

[1] Michael J. Economides and Kenneth G. Nolte, *Reservoir stimulation, 3rd edition*. John Wiley & Sons, 2000.

[2] H.A. Nasr-El-Din, H. Dana, V. Tomos, T. Stanitzek, C.A. de Wolf, and A. Alex, "Field treatment to stimulate an oil well in an offshore sandstone reservoir using a novel, low-corrosive, environmentally friendly fluid", *SPE International Symposium and Exhibition on Formation Damage Control, Lafayette, Louisiana, USA, 26 - 28 February 2014*. DOI: 10.2118/168163-MS

[3] Qin Ji, Lijun Zhou, and Hisham Nasr-El-Din, "Acidizing sandstone reservoirs with aluminum-based retarded mud acid", *SPE Journal*, Volume 21, Isse 3, pp. 1050 - 1060, 2016. DOI: 10.2118/169395-PA.

[4] Mian Umer Shafiq and Hisham Ben Mahmud, "Sandstone matrix acidizing knowledge and future development", *Journal of Petroleum Exploration and Production Technology*, Volume 7, pp. 1205 - 1216, 2017. DOI 10.1007/s13202-017-0314-6.

[5] НИПИ Отчет, *"Разработка специальных составов и опытно-промышленные испытания технологии ОПЗ для слабоцементированных песчаников м/р Дракон"*, СП Вьетсовпетро, 2015.

[6] НИПИ морнфтегаз СП, Вьетсовпетро, Годовые отчеты о научно-исследовательской работе *"Анализ состояния эксплуатационного фонда скважин, рекомендации по оптимизации его работы и интенсификации нефтедобычи"*, 1991 - 2017.

[7] Satya Priya Moulik and Animesh Kumar Rakshit, "Physicochemistry and applications of microemulsions", *Journal Surface Science Technology*, Volume 22, Issues 3 - 4, pp. 159 - 186, 2006.

[8] Vietsovpetro/NIPI, "*Nghiên cứu kết hợp đồng thời các giải pháp xử lý vùng cận đáy giếng, thông vỉa sâu, loại trừ lắng đọng hữu cơ trong cần khai thác nhằm tăng hiệu quả khai thác giếng dầu*".

[9] Vietsovpetro/NIPI, "*Công nghệ sử dụng hợp chất acid để nâng cao hệ số sản phẩm của giếng khai thác và độ tiếp nhận của giếng bơm ép thuộc đối tượng Oligocene mỏ Bạch Hổ*", 2008.

[10] Vietsovpetro/NIPI, "*Công nghệ tăng sản lượng khai thác dầu nhờ bơm các thành phần không có tính acid để tạo hỗn hợp acid tại đáy giếng khi tiến hành xử lý vùng cận đáy giếng*", 2012.

[11] Vietsovpetro/NIPI, *"Nghiên cứu và tối ưu hóa tổ hợp công nghệ để xử lý vùng cận đáy giếng các giếng khoan của Vietsovpetro*", 2018.

[12] Từ Thành Nghĩa, Nguyễn Thúc Kháng, Lê Việt Hải, Nguyễn Quốc Dũng, Nguyễn Văn Trung, và Phan Đức Tuấn, "Công nghệ xử lý acid vùng cận đáy giếng các vỉa dầu có nhiệt độ cao ở thềm lục địa Nam Việt Nam", *Tạp chí Dầu khí*, Số 1, 2018

[13] Nguyen Quoc Dung, Pham Trung Son, Nguyen Van Trung, and Nguyen Van Nga, "Characterisation of acid treatment for damaged zone in fractured granitic basement of Bach Ho field", *Petrovietnam Journal*, Volume 6, pp. 41 - 47, 2019

[14] Norman R. Morrow and Zhengxin Tong, "Method for increasing the production of hydrocarbon liquids and gases", United States Patent US 7549472 B2, 2009.

[15] D.A. Shock, J.D. Sudbury, and J.J. Crockett, "Studies of the mechanism of paraffin deposition and its control", *Journal of Petroleum Technology*, Volume 7, Issue 9, pp. 23 - 28, 1955. DOI: 10.2118/384-G.

[16] Noman Shahreyar, "*Review of paraffin control and removal in oil well using Southwestern petroleum short course searchable database*", 2000.

[17] L.J. Kalfayan and A.S. Metcalf, "Successful sandstone acid design case histories: Exceptions to conventional wisdom", *SPE Annual Technical Conference and Exhibition, Dallas, Texas, 1 - 4 October, 2000*. DOI: 10.2118/63178-MS.

[18] C.E. Shuchart and R.D. Gdanski, "Improved success in acid stimulation with a new organic HF system, *European Petroleum Conference, Milan, Italy, 22 - 24 October 1996*. DOI: 10.2118/36907-MS.

[19] D.E. Simon and M.S. Anderson, "Stability of clay minerals in acid", *SPE Formation Damage Control Symposium, Lafayette, Louisiana, 22 - 23 February 1990*. DOI. 10.2118/19422-MS.

[20] K. Krishna Mohan, Ravimadhav N. Vaidya, Marion G. Reed and H. Scott Fogler, "Water sensitivity of sandstones containing swelling and non-swelling clays", *Colloids and Surfaces A: Physicochemical and Engineering Aspects*, Volume 73, pp. 237 - 254, 1993. DOI: 10.1016/0927-7757(93)80019-B.

PETROVIETNAM
SCIENCE, TECHNOLOGY & INNOVATION PETROVIETNAM

A COMPREHENSIVE STUDY ON TECHNOLOGICAL SOLUTIONS FOR ASSOCIATED GAS GATHERING, TREATMENT, AND UTILIZATION AT OFFSHORE FIELDS OPERATED BY VIETSOVPETRO

Le Viet Dung, Nguyen Lam Anh, Nguyen Anh Phong, Nguyen Quoc Dung, Chu Van Luong, Nguyen Hoai Vu
Vietsovpetro Joint Venture
Email: vunh.pt@vietsov.com.vn
https://doi.org/10.47800/PVSI.2025.06-03

Summary

In 1986, after nearly 5 years of exploration, Vietsovpetro successfully produced its first crude oil from the Bach Ho field, located in Block 09-1 of the Cuu Long basin on the Vietnamese continental shelf. This milestone marked a historic breakthrough for Vietnam's petroleum industry, positioning the country among the oil-producing and exporting nations and laying the foundation for the development of the modern Vietnamese oil and gas sector.

In 1995, Vietsovpetro achieved another significant milestone by pioneering the gathering, treatment, and onshore transportation of associated gas through innovative technological solutions and engineering improvements, despite limited offshore infrastructure at the time. This initiative marked the second major leap in Vietnam's petroleum industry and served as the technological and operational foundation for the subsequent establishment and growth of the Petrovietnam Gas Joint Stock Corporation (PV GAS).

This article presents the key technical highlights of a cluster of projects on associated gas gathering and utilization implemented by Vietsovpetro at offshore fields in Block 09-1 and adjacent offshore fields.

Key words: Associated gas, gas gathering, gas treatment, Block 09-1, Bach Ho field.

1. Introduction

In the 1940s, countries such as the United States, Norway, and Canada utilized up to 70% of the associated gas separated from crude oil production for processing, power generation, and other applications. Over the subsequent decades, these countries have significantly improved their gas recovery efficiency and currently utilize more than 95% of their associated gas. Major international oil companies, including Chevron (USA), TotalEnergies (France), and Shell (UK and the Netherlands), have achieved nearly 100% associated gas utilization in their field developments [1].

In contrast, the former Soviet Union (now the Russian Federation) historically prioritized crude oil production, and associated gas often was flared at the field site. However, since the early 2000s, driven by economic development and global environmental commitments, the Russian government has implemented stricter regulations, mandating associated gas utilization levels of up to 95% for new field developments.

Maximizing associated gas recovery is a crucial component of sustainable hydrocarbon development. Many governments now require oil and gas operators to submit a detailed plan for gathering and utilizing associated gas in investing and developing oil fields. Compliance with these regulations has become a key criterion for governments to grant or suspend oil and gas exploration and production licenses in regions and territories.

The Bach Ho oil field, located in Block 09-1 of the Cuu Long basin, was initially designed, constructed, and developed primarily for oil extraction, with the associated gas being flared directly on offshore platforms [2]. As a result, between 1986 and the first quarter of 1995,

Date of receipt: 25/8/2025.
Date of review and editing: 25/8 - 28/9/2025.
Date of approval: 28/9/2025.

Vietsovpetro flared more than 6 billion cubic meters of associated gas, equivalent to approximately 6 million tons of oil. During this period, Vietnam was experiencing a severe energy crisis. Each year, Vietnam imports diesel oil (DO), fuel oil (FO), and liquefied petroleum gas (LPG) to meet domestic energy demands. The Ba Ria thermal power plant, located only 120 kilometers from the Bach Ho field, depended entirely on imported DO and FO for electricity generation. Moreover, the country was still under international embargo, facing acute shortages of foreign currency and undergoing profound economic and social hardship.

The continuous flaring of associated gas not only resulted in the loss of a valuable non-renewable national resource but also had adverse environmental impacts, contributing to air pollution and ecological degradation in oil-producing regions. Addressing the technical and economic challenges of gathering and utilizing associated gas thus became an urgent and strategic objective for the Petrovietnam, and particularly for Vietsovpetro.

In 1995, Vietsovpetro initiated the gathering of associated gas for utilization at offshore facilities, with the remaining volume transported ashore. By September 30, 2025, Vietsovpetro had gathered, treated, and delivered approximately 40.3 billion cubic meters of associated gas to onshore facilities, of which more than 23.5 billion cubic meters of gas had been used to meet the industrial development of Vietnam's gas, electricity, fertilizer, petrochemical value chain, and serving residential and industrial needs. The success of this initiative has established a reliable foundation for the long-term growth of the Vietnamese gas industry.

2. Technological solutions for associated gas gathering, treatment, and transportation at Vietsovpetro's and adjacent fields

In 1991, with the approval of the Government, Vietsovpetro developed a technical and economic feasibility study titled "Gathering and transportation of associated gas from the Bach Ho field to shore", with the following key points:

- Efficient utilization of fuel resources was identified as one of the urgent tasks for Vietnam's economic and social development;

- Associated gas from offshore facilities in Block 09-1 needed to be gathered and utilized to the maximum extent;

- The main content of the feasibility study was to develop a program for transporting gas to shore for use as fuel in thermal power plants in southern Vietnam.

The implementation of the project for gathering and transporting associated gas from the Bach Ho field to Thu Duc, Ho Chi Minh City, was estimated to take approximately 8 to 10 years.

Based on an assessment of existing infrastructure and field conditions at the offshore Bach Ho Field, Vietsovpetro initiated research into technological solutions for the early gathering and transportation of associated gas to shore, despite the absence of gas compression facilities at that time.

2.1. Solution for the early associated gas gathering and transportation of 1 million stm^3/day from the Bach Ho field to shore without using compressors

To implement the associated gas gathering and transportation project from the Bach Ho Field, Vietsovpetro proposed to construct the Bach Ho - Dinh Co - Ba Ria gas pipeline, with a total length of 120 km and a diameter of 406 mm.

Vietsovpetro conducted research on technological solutions and carried out offshore trials to assess the feasibility of gathering and transporting 1.0 million stm^3/day of associated gas from the Bach Ho field to the Ba Ria thermal power plant, utilizing the natural energy of oil wells in conditions where gas compressors were not yet available:

- Hydraulic calculation for the transportation of 1.0 million stm^3/day of associated gas through the 120 km pipeline (406 mm diameter), from the Bach Ho Field to the Ba Ria thermal power plant, showed a pressure loss of approximately 17 - 18 atm.

- Given that the required gas pressure at the onshore receiving point was 20 atm, the necessary inlet pressure at the offshore end had to be 38 - 40 atm. Vietsovpetro conducted experiments to separate gas from high-pressure, high-flow oil wells. The results indicated that gas separated from the oil-gas mixture produced from the basement formation at the wellhead platform BK-2 yielded approximately 1.0 million stm^3/day of associated gas at 38 - 40 atm.

- With an inlet gas pressure of around 40 atm and a flow rate of 1.0 million stm^3/day, Vietsovpetro successfully transported the gas through the Bach Ho - Dinh Co - Ba

Ria pipeline, via Gas Distribution Station (GDS) at Ba Ria, and delivered it to the Ba Ria thermal power plant starting from the second quarter of 1995.

2.2. Solution for drying associated gas from the Bach Ho field without using a heat exchanger for onshore transportation

The implementation of the above solution showed that the gas separated at the wellhead platform BK-2 had a temperature of 90 - 100°C and a pressure of 38 - 40 atm, which was transported to shore through a subsea pipeline, where the temperature averaged around 25 - 28°C. Upon reaching the shore, the gas had been cooled, and liquids that had condensed along the pipeline caused the gas stream to arrive at shore in a two-phase (liquid-gas) form, which did not meet the fuel requirement for the Ba Ria thermal power plant. While the Central Processing Platform No.2 (CPP-2) did not have a heat exchange system, Vietsovpetro developed a gas dehydration solution offshore by passing the gas stream through a subsea pipeline loop from BK-2 to BK-3 and then back to BK-2. As the gas circulated through the subsea loop, it was naturally cooled by the seawater, causing it to become a two-phase form which was then sent to a slug catcher, a liquid separator already installed on the CPP-2 platform (nearby BK-2), to separate the liquids. The gas exiting the slug catcher was in single-phase (dry gas) form and was routed into the Bach Ho - Dinh Co pipeline for transportation to the Ba Ria thermal power plant. As a result, the gas reaching the power plant had a temperature of at least 25 - 28°C and was in dry form, thus meeting the fuel specifications required by the Ba Ria thermal power plant.

2.3. Solution to increase gas flow to 2 million stm³/day for onshore transportation

The complete gas compression station (CGCS) at the Bach Ho field was constructed adjacent to the MSP-4 platform and officially commenced operation in February 1997. With a capacity of 1 million stm³/day and an output pressure of 105 atm, it was primarily designed to supply gas for internal consumption within the Bach Ho field. At that time, the Phu My 1 thermal power plant had been built and came into operation, and the onshore gas demand increased to 2 million stm³/day. According to the calculation for pipeline pressure to transport 2 million stm³/day from the offshore to Phu My Plant, the minimum required gas pressure at Bach Ho offshore must be around 58 - 60 atm. To meet this requirement, Vietsovpetro researched and implemented a technological solution utilizing an ejector (gas mixing device) to blend two streams of gas: high-pressure gas steam (105 atm) from the CGCS and a low-pressure gas stream (28 atm) after preliminary separation (UPOG) on the BK-2 platform. As a result, a medium-pressure gas stream was obtained.

By mixing 1 million stm³/day of high-pressure gas from CGCS with 1 million stm³/day of low-pressure gas after UPOG using the ejector, a combined stream of 2 million stm³/day was obtained at a pressure of approximately 60 atm, which was sufficient to transport to shore, supplying both the Phu My 1 and Ba Ria thermal power plants.

At that time, the ejector installed by Vietsovpetro was the largest offshore gas mixing device ever deployed on offshore facilities worldwide, a specifically designed technological solution for long-distance gas transportation.

2.4. Solution for low-pressure gas gathering at Bach Ho field

The low-pressure gas separated on platforms at the Bach Ho field typically had pressures ranging from 0.5 to 1.5 atm, and was flared at the individual platform flare stacks because it could not be gathered economically due to the high cost of installing compression systems. To recover and utilize this low-pressure gas, Vietsovpetro studied and implemented a solution for transporting gas-saturated oil (oil containing dissolved gas) between the platforms. Specifically, oil at each platform was separated at a high-pressure separator (on the separator in the first stage), then the saturated oil was transferred to another nearby platform without passing through a low-pressure separator or pump. Finally, the oil was routed to a designated gathering platform, as detailed below [3]:

- Low-pressure gas gathering at platform MSP-4: Production fluids from MSP-7, MSP-5, and MSP-3, after passing through high-pressure separators (first stage), were transferred as gas-saturated oil to MSP-4 via the pipeline sequence MSP-7 → MSP-5 → MSP-3 → MSP-4. At MSP-4, second-stage separation was carried out, recovering low-pressure gas (0.5 - 1.0 atm) from those platforms and from portions of MSP-6 and MSP-4 itself. A booster compressor with a capacity of 18 thousand stm³/day was installed on MSP-4 to compress this low-pressure gas to 6 - 7 atm, which was then sent to the CGCP compression platform and further compressed to 105 atm.

- Gathering low-pressure gas at platform MSP-9: Similarly to MSP-4, on MSP-10, production fluids from BK-15 and MSP-10 were separated at the first stage, and the gas-saturated oil was then transferred to MSP-9, where low-pressure gas (0.5 - 1.5 atm) was separated in a second-stage separator. A booster compressor with a capacity of 18 thousand stm^3/day was installed on MSP-9 to compress the low-pressure gas to 13 - 14 atm, and it was then transferred to the Central Compression Platform (CCP).

- Gathering low-pressure gas at CPP-2 and CPP-3: At the central processing platforms CPP-2 and CPP-3, low-pressure gas was separated from production fluids of all BK platforms at the Bach Ho field. Significant volumes of low-pressure gas were separated at these platforms. To gather all the low-pressure gas separated from CPP-2 and CPP-3, Vietsovpetro proposed and implemented the installation of gas compression stations with a capacity of 150 thousand stm^3/day per platform. The gas was compressed to 12 - 13 atm and then transferred to the CCP next to CPP-2 for further compression up to 125 atm.

By using this method of transferring saturated oil without pumps and installing booster compressors on fixed platforms such as MSP-4, MSP-9, CPP-2, and CPP-3, Vietsovpetro successfully gathered 90 - 95% of the associated gas separated from the oil production facilities at Bach Ho field, Block 09-1.

2.5. Solution for gathering remaining associated gas from the Rong field after DGCP went into operation

In 2010, the Rong gas compression platform (DGCP), with a capacity of 1 million m^3/day, went into operation. As crude oil production volume in the Rong field increased significantly with the commissioning of new production platforms (e.g., RC-5, RC-9), the volume of associated gas separated exceeded the gathering capacity of DGCP.

The associated gas that could not be gathered at DGCP was typically flared on platforms at Rong field. Vietsovpetro studied and implemented the following solutions for gathering associated gas [4]:

- High-pressure gas gathering and transportation to Bach Ho: High-pressure gas from the Rong field was gathered and transported to the Bach Ho compression platform using an existing pipeline (formerly used for oil transportation), along the route RP-2 → RC-1/3 → BK-2 → CPP-2 without gas compressors. From October 2011 to December 2012, Vietsovpetro successfully gathered and transported 64.6 million stm^3 of associated gas from Rong field to Bach Ho field.

- Installation of booster compressors for remaining gas: To gather additional the remaining gas after DGCP began operation, Vietsovpetro proposed and installed two booster compressors - one on DGCP and another on RP-3 platform - each with a capacity of 500 thousand stm^3/day. From November 2013, the booster compressor on DGCP started operating, followed by the booster compressor on RP-3, enabling the gathering of an additional 1.0 million stm^3/day of Rong field gas for transfer to the Bach Ho field. This gas would have been otherwise flared in Rong field. The solution not only helped optimize resource use but also reducing the environmental impact associated with gas flaring.

3. Application of research in production practice at Vietsovpetro

3.1. Technological solutions utilizing associated gas at Vietsovpetro's oil fields

3.1.1 Utilizing associated gas for oil and gas production via gas-lift without using compressors

Based on experience and mechanical lifting methods currently applied worldwide, Vietsovpetro has gradually researched and tested various lifting methods in crude oil production at the Bach Ho field, Block 09-1 [4]:

- A pilot study was conducted using submersible hydraulic piston pumps and screw pumps at wells 21 and 28 on the fixed platform MSP-1, Bach Ho field. Due to high-temperature wells, long operational times, and high levels of mechanical impurities in the produced fluids, the equipment frequently shuts down. The pilot test was unsuccessful, and the method proved ineffective.

- A pilot study of electric submersible pumps (ESP) was conducted in 10 wells at the Bach Ho field, the results showed that presence of mechanical impurities and sand in the produced fluids frequently caused pumps to fail and burn out, leading to low efficiency and frequent repair and replacement.

- Testing of combined ESP and gas-lift systems was carried out at 3 wells in the Bach Ho field and 6 wells on the RP1 platform at the Rong field. None of the tests was effective.

- A pilot study was conducted on the gas-lift method without a compressor on platform MSP-1 by using high-pressure gas separated from high-rate and high-pressure

wells (such as wells 401 and 403/MSP-1) to inject into low-rate wells with poor natural flow. The results showed that gas-lift method operated stably, extended production time, and were independent of sand and contaminants, equipment limitations, and power on platforms. The total amount of crude oil produced using this gas-lift method without a compressor reached 81,660 tons, with approximately 24,702,150 m^3 of compressed gas utilized.

Since 1997, Vietsovpetro has implemented the gas-lift technology on a wide scale. Consequently, the central compression platform (CCP) at the Bach Ho field was put into operation in August 1997, supplying high-pressure gas (125 atm), and enabling extended gas-lift applications across Vietsovpetro's fields. This success significantly improved well productivity and oil recovery factors for fields in Block 09-1. It also served as a valuable reference for oil operators to apply not only on the Vietnamese continental shelf but also across Southeast Asia.

3.1.2. Utilizing associated gas as fuel for power generation and centralizied power supply on offshore facilities

Initially, under the 16716 "Korall" design model for developing the Bach Ho field, the offshore power supply system relied on independent diesel-powered generator stations, including DGRA 500/500 and AMAN (800 kW) diesel generators, as well as 6ЧН-25/34/8ЧН-25/34 electric engines installed on platforms.

Vietsovpetro researched and gradually implemented the use of associated gas as a fuel source for offshore power systems, through the following key initiatives [5]:

- Vietsovpetro transitioned from diesel to associated gas in power generation systems on offshore facilities in Block 09-1, including both the Bach Ho and Rong fields. This transition was successfully implemented.

- Vietsovpetro also researched the application of associated gas for gas turbines and mechanical drives on gas compression platforms.

Since 2012, all power generation on Vietsovpetro's offshore installations in Block 09-1 has been fully fueled by associated gas.

To optimize the supply of offshore power resources at Block 09-1, Vietsovpetro conducted studies and developed a centralized power system, utilizing subsea power cables to distribute electricity across the entire field. This solution has brought significant savings for Vietsovpetro in the field operation and production in Block 09-1 on the Vietnamese continental shelf. From commissioning to December 31, 2019, the centralized power system had generated and supplied a total output of 772,454,100 kWh.

3.1.3. Using associated gas to replace FO/DO fuel for oil heating on processing platforms and FSOs

On the CPP-3, the boiler system providing heat for crude oil (T-1-A/B/C/D) used DO/FO oil. Vietsovpetro conducted research on using associated gas as a substitute for diesel oil (DO) for the boilers on CPP-3. Currently, the amount of associated gas used to maintain and stabilize the boiler system is about 18 - 25 thousand stm^3/day, replacing DO/FO fuel.

On FSOs, the high-capacity boiler systems for heating oil are used to heat crude oil before it is transferred to the processing tanks. In these tanks, water is separated to meet the specifications for commercial crude oil. Since 2014, on the VSP-02 FSO, Vietsovpetro conducted a study on recovering flash gas from breathing valves and proposed the installation of a gas compression station for utilizing this gas. The gas compression station gathers all flash gas released from the processing and cargo tanks, then compresses it to 5 atm, dries it, and supplies it for the boiler system as a fuel source, replacing DO/FO for oil heating on the FSO. The gas compression system on the VSP-02 FSO was commissioned in 2016, and by December 31, 2019, it had saved 7,358 tons of FO.

The aforementioned facilities have demonstrated high economic efficiency and made significant and sustainable contributions to the national economy, society, and environmental protection.

3.2. Effectiveness of applying research to production practice at Vietsovpetro

- From April 1995 to February 1997, Vietsovpetro supplied 579 million stm^3 of associated gas from the Bach Ho field to the Ba Ria thermal power plant.

- In 1997, Vietsovpetro supplied 2 million stm^3/day of gas to both the Ba Ria and Phu My 2.1 thermal power plants. The total additional volume of gas delivered onshore during this period was 233.2 million m^3.

- In 2008, the use of gas-saturated oil transport at the Bach Ho field to collect low-pressure gas, along with the installation of booster compressors marked a further milestone in associated gas recovery at oil and gas fields in Block 09-1.

- After 2010, when the DGCP was commissioned but could not gather all separated associated gas, Vietsovpetro's technological solutions achieved significant recovery of high-pressure associated gas from the Rong field. From October 2011 to December 2012, a total of 64.6 million stm^3 of associated gas was delivered to Bach Ho field then ashore. From November 2013 onward, an additional 1.0 million stm^3/day of gas was successfully gathered and utilized.

3.3. Economic efficiency of the project cluster

A cluster of projects on the research and application of technological solutions for the gathering, processing, and utilization of associated gas at Vietsovpetro's offshore fields and adjacent fields has brought significant economic benefits. The total economic efficiency of the project cluster is evaluated based on the effectiveness of the associated gas gathering and utilization solutions, as presented above:

- The effectiveness of the early gas gathering solution, delivering 1 million stm^3/day to shore without compressors and used as a substitute fuel for DO/FO at the Ba Ria thermal power plant (fast-track phase), is VND 1,471.69 billion (equivalent to USD 132.05 million) (Table 1).

- Effectiveness of the solution using an ejector to increase the gas transport capacity to shore to 2.0 million stm^3/day: It boosted the volume of gas transported ashore during the 1995 - 1997 period by 233.2 million m^3. The entire volume of gas was used as fuel for the Ba Ria and Phu My 2.1 thermal power plants, replacing 545.2 thousand tons of FO, with a cost saving of VND 654.60 billion, equivalent to USD 56.32 million.

- Effectiveness of associated gas gathering solutions from the Rong field, transporting it to Bach Ho CCP and then to shore (Rong field fast-track phase): Shown in Table 2.

- Comparison of efficiency of oil production by using gas-lift solution (in first phase) without gas compression platform versus the option of using gas compression platform: From March to June 1990, pilot tests were conducted using annulus gas of well 401/MSP-1 as gas-lift supply for wells 24, 27, 28, 36, 37, 38, and 46. After successful trials, from February 1993 to January 1997, the gas-lift oil production method without using compressors was expanded to wells 21, 24, 27, 28, 36, 37, 38, and 46 (using high-pressure gas separated from the products of wells 401 and 403/MSP-1). The total amount of oil extracted using the gas-lift method without compressors was 81,660 tons. The total amount of gas used was approximately 24,702,150 stm^3. The unit price for gas-lift compression in 1997 was USD 24.86 per thousand m^3. Therefore, the total cost savings achieved by using gas-lift for oil production without compressors were USD 0.61 million, equivalent to VND 6.91 billion (Table 3).

- Effectiveness of using associated gas as fuel for gas turbine engines to replace DO/FO for power generation on Vietsovpetro's offshore facilities: since the centralized power system was put into operation until December 31, 2019, the total electricity output of the system reached 772,454,100 kWh. Details of the electricity output from gas turbines are presented in Table 4.

The economic efficiency of the centralized power system is reflected in the cost savings gained by replacing individual diesel power stations. These savings are calculated based on the difference between the unit cost of generating electricity by individual diesel power stations and by centralized power supply, multiplied by the total power consumption of offshore facilities from the time the centralized power system was put into operation until December 31, 2019 (Table 5).

The total cost savings of Vietsovpetro for the period 2013 - 2019 is: 772,454,100 kWh × (USD 0.352 /kWh - USD 0.091 /kWh) = USD 201.86 million.

Table 1. *Cost savings calculation table from using gas to replace FO*

Year	Fuel gas volume		FO price	Cost if FO is used as fuel	Cost of gas purchase	Cost savings for power plants using gas instead of FO	
	Million m^3	FO equivalent, thousand tons	USD/ton	Billion VND	Billion VND	Billion VND	Conversion, million USD
1995	202.9	474.3	100	527.09	86.40	440.69	39.66
1996	287.8	672.8	133	988.37	206.10	782.27	70.99
1997	88.6	207.2	138	331.25	82.53	248.72	21.40
Total	579.3	1,354.3	-	1,846.72	375.03	**1,471.69**	**132.05**

Table 2. Cost savings from the early transportation of associated gas from the Rong field ashore

Year	Total volume of gas transported onshore		FO price	Cost if FO is used as fuel	Cost of gas purchase	Cost savings for power plants using gas instead of FO	
	Million m^3	FO Equivalent, thousand tons	USD/ton	Billion VND	Billion VND	Billion VND	Conversion, million USD
2011	5.4	12.7	675	175.63	37.84	137.79	6.70
2012	59.2	138.4	830	2,395.38	583.74	1,811.64	86.85
Total	64.6	151.0	-	2,571.01	621.58	**1,949.43**	**93.55**

Table 3. Economic efficiency of the oil production solution using gas lift without compressors

Well	Oil (tons)	Fluid (tons)	Gas lift (m^3)	Total cost savings from gas lift without using compressors (million USD)
21	4,474	9,585	1,437,750	0.036
24	18,489	45,796	6,869,400	0.171
27	19,845	19,882	2,982,300	0.074
28	9,557	17,284	2,592,600	0.064
36	1,633	2,429	364,350	0.009
37	1,194	7,130	1,069,500	0.027
38	11,060	35,425	5,313,750	0.132
46	15,408	27,150	4,072,500	0.101
Total	81,660	164,681	24,702,150	**0.614**

Table 4. Total electricity output from gas turbines as of December 31, 2019

Platform	Operating time		Average power generation capacity (kW)	Total electricity output from the start of operation to 31/12/2019 (kWh)
	Days	Hours		
PPD	2,266	54,384	5,500	294,479,800
CPP-3	2,043	49,032	7,950	380,133,400
GTG KPD	1,886	45,264	1,800	81,475,200
Typhoon	1,886	45,264	-	16,365,700
Total				**772,454,100**

- Economic efficiency of gathering gas on the VSP-02 FSO to replace DO/FO as fuel for crude oil heating in boilers.

Previously, FO as fuel was used for boilers on the FSO to heat crude oil, resulting in significant expenses for Vietsovpetro in the procurement and transportation of FO to the FSO. Meanwhile, flash gas released from the processing and cargo tanks on the FSOs was vented directly into the environment. Vietsovpetro conducted studies and invested in a gas recovery system on the VSP-02 FSO to collect flash gas, recover condensate for mixing with crude oil and utilize the recovered gas as boiler fuel. This solution has been then expanded to the VSP-01 FSO. By utilizing the gathered flash gas on the VSP-02 FSO during 2016 - 2019, Vietsovpetro saved approximately USD 4.86 million in FO costs (Table 6).

In addition, the economic efficiency of the solution to lower the dew point through subsea heat exchange, as well as the economic efficiency derived from the scientific content of Vietsovpetro's research and proposals for the construction projects of the CGCS, CCP, DGCP gas compression platforms and the two boosters at the Rong field, is considerable. However, due to insufficient data collection, it is not yet possible to quantitatively evaluate the economic efficiency of these solutions.

3.4. Social benefits and other sectoral benefits

In the 1990s, fuel for power generation was extremely scarce, while associated gas was being flared offshore (due to inadequate facilities). By using a fast-track design and construction solution, associated gas was gathered, processed, and transported to shore to supply the Ba Ria

Table 5. *Unit cost of diesel-generated electricity and gas turbine-generated electricity*

No.	Index	Unit	Value
A. Unit cost of producing 1 kWh using a diesel power station in 2013			
1	Total offshore electricity service cost in 2013 of the electrical engineering Enterprise (excluding diesel fuel)	USD	31,296,403
2	Total offshore electricity output in 2013	kWh	229,786,000
3	Diesel consumption per 1 kWh	liter/kWh	0.346
4	Average diesel price	USD/m²	495
5	Average transportation cost for 1 ton of goods from shore to offshore	USD/ton	152
6	Diesel fuel cost to produce 1 kWh	USD/kWh	0.216
7	Unit cost of producing 1 kWh using a diesel generator on offshore facilities	USD/kWh	0.352
B. Unit cost of producing 1 kWh of electricity using gas turbines and the centralized power supply system		USD/kWh	0.091

Table 6. *Economic efficiency of gas recovery for heating use on Vietsovpetro's FSOs as of December 31, 2019*

No.	Index	Unit	Year				Total
			2016	2017	2018	2019	
1	Volume of gas collected for use as boiler fuel on VSP-02 FSO	Ton	1,689.0	651.0	807.0	3,301.0	6,448.0
	Calorific value of gas	MJ/kg	47.59				
	Calorific value of FO oil	MJ/kg	41.7				
2	Equivalent FO volume (if gas had not been used)	Ton	1,927.38	742.88	920.90	3,766.89	7,358.1
3	Unit price calculation						
	FO oil price	USD/m³	396	429	495	594	
	FO oil density	Ton/m³	0,95				
	Converted FO oil price	USD/ton	416.84	451.58	521.05	625.26	
	Offshore cargo transportation cost	USD/ton	148.5	120.5	98	111.5	
	FO oil price at offshore facilities	USD/ton	565.3	572.1	619.1	736.8	
4	FO saved by using gas as boiler fuel	Million USD	1.09	0.42	0.57	2.78	**4.86**

thermal power plant. This brought a major transformation to Vietnam's industrial landscape and laid the groundwork for the establishment of the Phu My thermal power plants. Subsequently, it helped alleviate the energy crisis and reduce rotating power outages in the 1990s.

The application of technological solutions facilitated the gathering of associated gas from production fields in the Cuu Long basin, located on the continental shelf offshore southern Vietnam. Vietsovpetro's facilities have effectively become a hub for connecting and transporting gas from fields such as Rong, Rang Dong, Su Tu Den, Su Tu Vang, Su Tu Trang, Hai Su Den, Hai Su Trang, Te Giac Trang, Ca Ngu Vang, Thien Ung, and Dai Hung, contributing to enhance the efficiency of oil field development on the Vietnam continental shelf.

The gathering, processing and transporting of associated gas to shore by Vietsovpetro has delivered significant benefits to the Vietnamese economy. This initiative replaced traditional DO as a fuel source in thermal power plants and laid the groundwork for the development of new products such as urea, LPG, and raw materials for petrochemical plants, forming a solid foundation for the growth of the Vietnamese gas industry. Specifically, the production of urea fertilizer from domestically natural gas has contributed to ensuring national food security; LPG has contributed to urbanization, replacing traditional fuel sources in various industries. These developments have also created employment opportunities and increased household incomes. Gathering associated gas reduced offshore flaring, thereby lessening air pollution, maximizing of the

national resource recovery, and supporting sustainable socio-economic development.

4. Conclusion

The results of research, development, and implementation of associated gas gathering, processing, transportation, and utilization at fields in Block 09-1 and adjacent fields lead to the following conclusions:

Scientific and technological achievements: Successfully established and developed an integrated system of solutions for associated gas gathering, processing, transportation, and utilization. The developed technologies are grounded in solid scientific foundations, well-suited to actual field conditions, and have been implemented at Vietsovpetro and replicated nationwide.

Resource recovery efficiency: The application of solutions developed through this project cluster has increased the associated gas recovery and utilization rate from nearly 0% (previously almost entirely flared offshore) to over 90%, thereby enhancing the value of national oil and gas resources.

Hub connectivity role: Vietsovpetro's facility system has become a central hub for the gathering and transportation of gas, as well as the interconnection of offshore oil and gas fields in southern Vietnam, creating significant opportunities for investment and development in associated gas gathering from adjacent fields operated by Vietnam National Industrial - Energy Group and its partners.

Socio-economic contributions: Established a critical foundation for attracting domestic and international investments and for developing products that serve national economic growth, such as electricity, fertilizers, and chemicals. The successful implementation of these solutions has delivered substantial economic benefits to Vietsovpetro and Vietnam's petroleum industry.

Future prospects: The economic efficiency of this research cluster is expected to continue growing throughout the remaining life cycle of Vietsovpetro's field and will further expand as the facility system is connected to additional small and marginal fields in the future.

References

[1] В.И.Фейгин, О.Б.Брагинский, С.А.Заболотский, И.Г.Кукушкин, А.В.Маевский, Н.И.Масленнико, и *Ю.Г.Рыков, Исследование состояния и перспектив направлений переработки нефти и газа, нефте- и газохимии в РФ*. Библиотека Института современного развития, 2011.

[2] Petrovietnam, *"Luận chứng kinh tế - kỹ thuật hệ thống thu gom và vận chuyển khí Bạch Hổ"*, 1991.

[3] Trần Lê Phương, Phạm Thành Vinh, A.G. Axmadev, Tống Cảnh Sơn, Châu Nhật Bằng, Nguyễn Hữu Nhân, Đoàn Tiến Lữ, Trần Thị Thanh Huyền, Lê Thị Đoan Trang, Đỗ Dương Phương Thảo, và Phan Đức Tuấn, "Tối ưu, nâng cao hiệu quả hoạt động hệ thống công nghệ thu gom, vận chuyển dầu khí tại các mỏ của Vietsovpetro", *Tạp chí Dầu khí*, Số 4, trang 24 - 31, 2020.

[4] Nguyễn Thúc Kháng, Trần Văn Vĩnh, Chu Văn Lương, Tống Cảnh Sơn, Phạm Trung Sơn, và Phạm Thành Vinh, "35 năm xây dựng và phát triển công nghệ khai thác dầu và khí của Liên doanh Việt - Nga Vietsovpetro", *Tạp chí Dầu khí*, Số 5, trang 14 - 21, 2016.

[5] Cao Tùng Sơn, Nguyễn Thúc Kháng, Lê Việt Dũng, Chu Văn Lương, Nguyễn Hoài Vũ, và Phùng Quang Thắng, "Giải pháp sử dụng khí đồng hành cho máy phát điện trên các công trình kết nối ngoài khơi tại mỏ Bạch Hổ và mỏ Rồng", *Tạp chí Dầu khí*, Số 9, trang 47 - 51, 2018.

PETROVIETNAM
SCIENCE, TECHNOLOGY & INNOVATION PETROVIETNAM

IMPROVING FDP DECISIONS UNDER SPARSE DATA: AN ADAPTIVE METROPOLIS APPROACH FOR NET-PAY QUANTILES

Pham Xuan Phuc, Le Tran Minh Tri, Tran Vu Tung, Nguyen Hong Kien, Nguyen Ngoc Tuan Anh, Pham Tien Trung
Phu Quoc Petroleum Operating Company (Phu Quoc POC)
Email: tungtv@phuquocpoc.vn
https://doi.org/10.47800/PVSI.2025.06-04

Summary

Early field-development decisions often rely on very small samples of reservoir property measurements, where common spreadsheet workflows (typically lognormal fits) become fragile and analyst-dependent. This paper presents the Metropolis-Adaptive Distribution Range-Constrained (M-ADRC) method, a practical Metropolis-Hastings (MH) approach with adaptive constraints for generating representative synthetic populations from low number of observations. The workflow combines (i) domain-informed parameter bounds, (ii) adaptive proposal tuning, (iii) automatic switching between Pearson Type III and lognormal distribution families, and (iv) adaptive iteration policy for samples with extreme bias.

Using a Southeast Asia gas field netpay dataset, the representative population generated by M-ADRC is benchmarked against the traditional lognormal spreadsheet approach across diverse net pay samples. Results show that M-ADRC achieves significantly lower Wasserstein Distance and smaller Swanson's mean error, reaching the "excellent" Wasserstein threshold with roughly eight samples, only half the sample requirement of the spreadsheet approach.

The workflow is lightweight, fully open-source, and requires no specialized hardware. It includes default settings, diagnostic checks, and sensitivity results, enabling reservoir engineers to apply M-ADRC without specialized tuning expertise. M-ADRC yields more reliable small-sample quantiles, reducing the risk of biased inputs in FDP scenarios and enhancing decision confidence. Workflow limitations such as restricted distribution types, resilience to extreme sampling bias, and the lack of geospatial properties will be addressed in future work.

Key words: Reservoir characterization, metropolis-hastings, uncertainty quantification, field development plan.

1. Introduction

Field development plant (FDP) is a strategy outlining the characteristics of an oil and gas field obtained through the exploration phase, and recommending the optimal procedure to extract the hydrocarbon safely, economically, while complying with all regulations and operational constraints. A central cornerstone of any FDP is reserve estimation, which is carried out through reservoir characterization [1]. One popular estimation method during the early stage of development is volumetric [2], where the reservoir is simplified as a porous box. The original oil and gas in place (OOGIP) is then calculated by multiplying the volume of the box (area times thickness) with porosity, hydrocarbon saturation, and dividing by formation volume factor [3]:

$$OOIP = \frac{Ah\phi S_o}{B_o}$$

$$OGIP = \frac{Ah\phi S_g}{B_g}$$

Therefore, quantifying the uncertainty in formation parameters such as porosity, water saturation, and net pay is pivotal for effective employment of volumetric methods [4, 5]. However, the complex nature of field exploration makes direct sampling difficult. To overcome limited sample data, reservoir engineers and geoscientists often rely on geostatistical methods, ranging from simple Kriging to sequential Gaussian simulation [6]. Research on these reservoir properties has been significant, with several papers proposing variations of methods and discussing the importance of these properties [7, 8].

Date of receipt: 22/9/2025.
Date of review and editing: 22/9 - 13/11/2025.
Date of approval: 13/11/2025.

Regarding the challenge of modeling the true distribution of geophysical properties from a small number of samples, a wide variety of statistical methods have been proposed [9]. GhojehBeyglou [10] compared Kriging, Sequential Gaussian Simulation (SGS), and Gaussian Random Function Simulation (GRFS) in determining porosity distribution and concluded that Kriging excels at giving single-point prediction, while SGS and GRFS are more compatible in capturing the variability. For 1D distribution, Aleardi [11] investigated the best statistical models for predicting the multi-dimensional distribution of porosity and litho-fluid facies based on a histogram.

In addition to the aforementioned statistical methods, a popular approach that has demonstrated considerable effectiveness is the application of Monte Carlo simulation [7], a repeated sampling method that has seen extensive use in the oil and gas industry and significantly refined over time through advances in computer engineering. However, traditional Monte Carlo implementations, such as those in Crystal Ball, require large datasets to produce reliable results, posing challenges in data-scarce environments like offshore fields. Therefore, the Metropolis-Hastings (MH) algorithm [12] is introduced as a Markov Chain Monte Carlo (MCMC) technique used to sample from complex probability distributions, applicable for low to very low numbers of samples. This method generates a sequence of correlated samples by proposing candidate points and accepting them with a probability that ensures convergence to the target distribution. MH has been researched thoroughly in petroleum engineering and geoscience, including reservoir modeling [13], well parameters estimation [14], and, most notably, history matching [15 - 17].

This study introduces a practical Metropolis-Hastings-based algorithm called Metropolis-Adaptive Distribution Range-Constrained (M-ADRC) to sample reservoir parameters by incorporating statistical data of the population to create an accurate representative synthetic population. The algorithm is packaged and deployed in a web environment for internal use. A case study using net pay data from Southeast Asian gas fields further validates the M-ADRC approach and demonstrates its superiority over the traditional approach.

2. Methodology

2.1. Distribution

The proposed algorithm currently deals with lognormal and Pearson III distributions.

Lognormal distribution

The lognormal distribution is a continuous probability distribution in which the logarithm of the variable is normally distributed. It is characterized by a positive skew (right-tailed). There are two parameters controlling a lognormal distribution (Figure 1):

- μ: The mean of the natural logarithm of the distribution.

- σ: The standard deviation of the natural logarithm of the distribution.

In petroleum engineering, this distribution type is frequently applied to model reservoir properties such as net pay, permeability, reserves, as these parameters often arise from multiplicative geological processes and exhibit right-skewed distributions [18, 19].

Pearson III distribution

The Pearson Type III distribution is a three-parameter probability distribution that represents a shifted and scaled form of the gamma distribution [20]. It is defined by:

- Skew (α) - controls the skewness. Negative means left-skewed and positive means right-skewed. Zero means normal distribution.

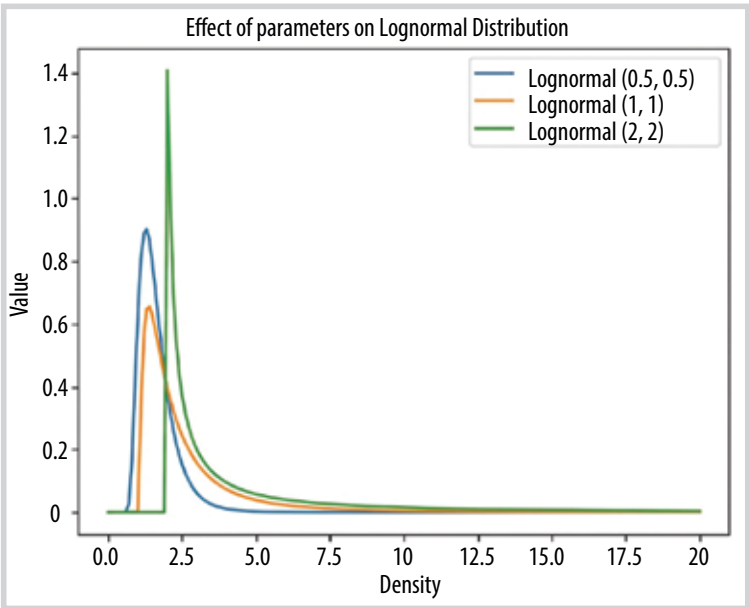

Figure 1. *Effect of parameters on lognormal distribution.*

- Location (μ) - shifts the curve left or right.
- Scale (β) - stretches or compresses the distribution.

Due to its flexibility in representing both positively and negatively skewed data (Figure 2), it has been widely applied in hydrology, sedimentology, and petroleum reservoir characterization. However, its complexity also poses challenges in modeling compared to simpler distribution types such as lognormal.

Metropolis-Hastings algorithm

The Metropolis-Hastings algorithm is a robust MCMC method designed to sample complex probability distributions where direct sampling is infeasible. It constructs a Markov chain that converges to the target distribution (P(x)), enabling the generation of representative samples. Assuming a sample set of x_0, x_1,… x_n from a presumably lognormal distribution of shape μ and scale σ, the algorithm's steps are as follows:

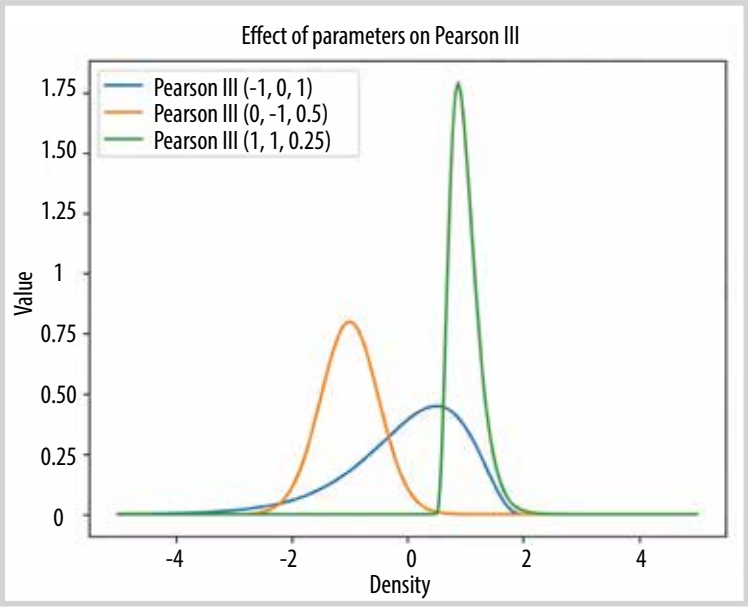

Figure 2. *Effect of parameters on Pearson III distribution.*

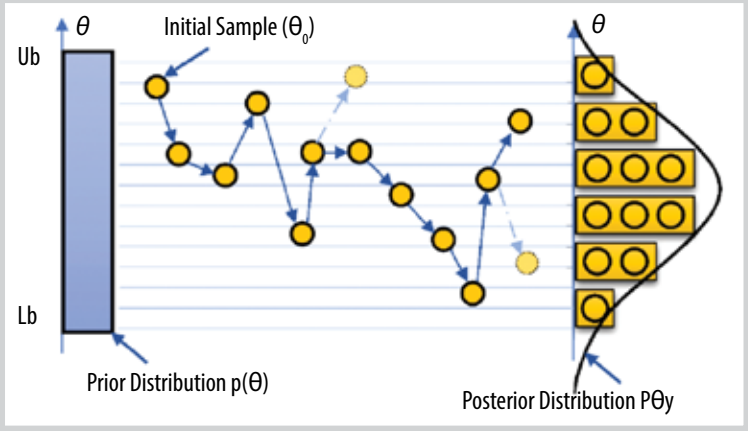

Figure 3. *Graphical representation of Metropolis-Hasting algorithm [21].*

Initialization: Start at iteration i = 0, select an initial value (μ_0 and l_0 with l = log (σ)) from the parameter space, typically based on domain knowledge or the mean/median value of the samples.

Proposal: Generate new candidate values μ_i and l_i from values in the previous iteration by adding a proposal term Є randomly selected from a symmetric, usually normal, distribution:

$$\mu_i = \mu_{i-1} + \epsilon_\mu$$
$$l_i = l_{i-1} + \epsilon_l$$
$$\epsilon \in N(0, \sigma)$$

Acceptance probability: The acceptance probability is calculated as:

$$\alpha = min\left(1, \frac{p(\mu_i, l_i)}{p(\mu_{i-1}, l_{i-1})}\right)$$

Acceptance/rejection: Draw a random number u from a uniform distribution. If α is larger than or equal to u then accept μ_i and l_i into the Markov chain. If not, then reject them and add the old values $\mu_{(i-1)}$ and $l_{(i-1)}$ instead.

Iteration: Repeat steps 2 - 4 for N number of iterations to generate Markov chains of μ and l. After a burn-in period, typically 10% of N, the chains converge and samples are collected.

Optimal parameters selection: From the chains, multiple methods can be employed to select the best set of parameters. For this study, simple median selection is sufficient.

$$\mu_i = \mu_{i-1} + \epsilon_\mu$$
$$l_i = l_{i-1} + \epsilon_l$$

For other types of distributions with a different number of parameters, the same concept is applicable. Figure 3 represents the graphical illustration of Metropolis-Hastings: generate a posterior distribution from a prior uniform distribution.

M-ADRC modified algorithm:

From the Metropolis-Hasting fundamentals, many functionalities are incorporated into M-ADRC algorithm:

Range restrictions

One of the key requirements for the algorithm to perform efficiently is a range limit of parameters (skewness, location, scale, mean of population), which can be obtained from domain experts' analysis and analogy data from nearby fields. The range should be wide to avoid accidentally excluding the true parameter values, also not so broad that the search space becomes inefficient and defeats the purpose of parameters range restriction. When the algorithm proposes an out-of-bound sample, it will be rejected. This improves the stability and efficiency of the search process.

Adaptive proposal

Acceptance rate is a key attribute in evaluating the reliability of Metropolis-Hasting process. Too low (< 1%) or too high (> 60%) rate implies poor sampling procedure. Acceptance rate can be adjusted through the proposal width of each parameter. To avoid manually tuning the width, a piecewise function is integrated into the algorithm. During burn-in period, the function divides this phase into 10 subsections and monitors the acceptance rate in each. If the acceptance rate is out of bound (1 - 60%), the function will multiply the rate by an adjustment factor depending on the magnitude of the acceptance rate. The adjustment factors are user-inputs. Future work may explore auto-adaptive algorithms for proposal width, such as works proposed by Rosenthal [22].

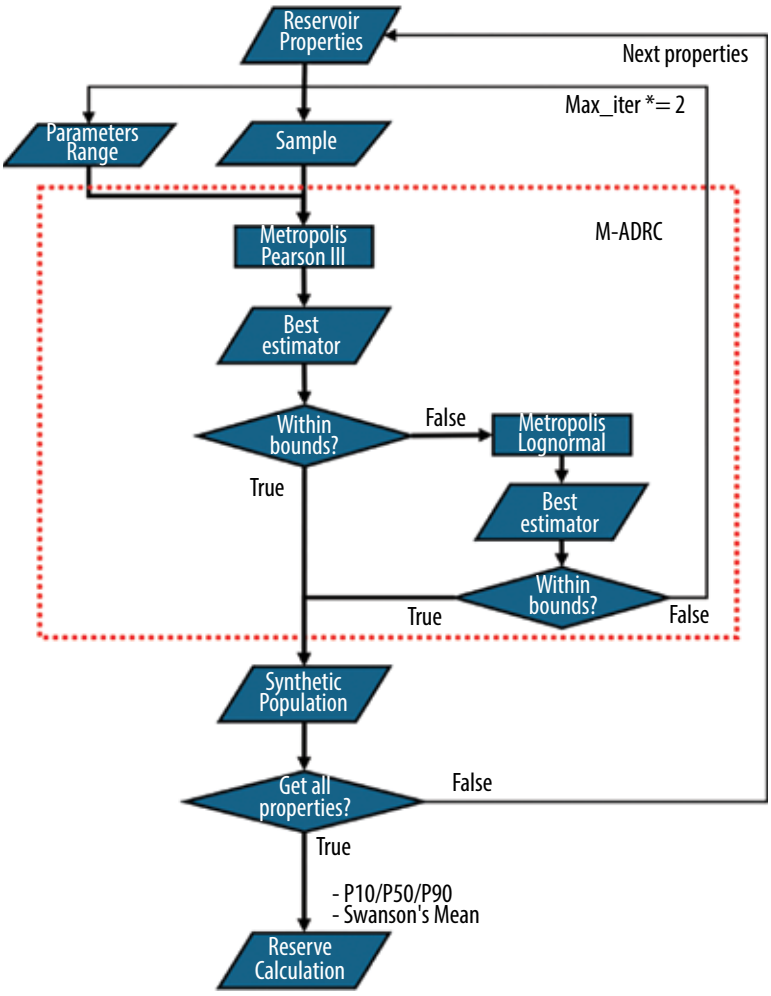

Figure 4. *M-ARDC workflow incorporated into reserve calculation.*

Distribution switch

If the original Pearson III fit fails to produce a correct final solution (out-of-bounds), which can happen in extreme cases of sampling bias, the algorithm will switch to a lognormal distribution and restart the entire process. Lognormal distributions are much more robust than Pearson III [23] and almost guarantee to produce a "reasonable" solution. A "risk factor" to quantify the risks involved in using these samples for modeling distribution will be introduced in future work.

Adaptive iterations

In worst-case scenario where both the Pearson III and lognormal distributions fail, the algorithm pulls a last-ditch effort by restarting the entire process from the beginning, with double the number of iterations. Our analysis shows that the main reason for failure is due to zero acceptance rate. This, however, can be remedied by increasing number of iterations so that the algorithm has time to stabilize during burn-in. This is, nevertheless, a quick fix that does not address the underlying sampling bias problem. This issue will be revisited in our future work.

Workflow

The M-ADRC workflow is visualized in Figure 4. Detailed procedures are as follows:

First, the algorithm will attempt to fit a Pearson III distribution on the sample and collect skew, location, scale values as initial guess.

The modified Metropolis algorithm is then executed to obtain distribution of these parameters, ensuring that all parameters must be within bounds. The best-guess value for each parameter is chosen as the median.

If the best-guess values do not meet requirements, the algorithm will switch to lognormal distribution and rerun the process.

If lognormal distribution also fails, the algorithm will restart from the beginning with double number of iterations.

The reserve estimation is incorporated into the M-ADRC workflow. For each property such as net pay, porosity, saturation, the algorithm will generate a synthetic population accordingly. Once all results have been acquired, it is then the decision of the petroleum engineers on how to proceed with reserve calculation: take the P10/P50/P90 or Swanson's mean of each property and multiply them in classical volumetric formula, or perform Monte Carlo on the joint synthetic population to get a synthetic distribution of the reserves.

2.2. Lognormal spreadsheet-based approach (LSA)

Many petroleum operating companies assume lognormal distribution for majority of reservoir properties like net pay, porosity, reserve. In order to generate distribution, they fit a lognormal curve to the samples, get μ and σ, generate the Percentage Point Function (PPF) and use it for Monte Carlo simulation. This process, while simple and reliable in many cases, can be highly misleading under some circumstances. The number of samples must be sufficient to generate a representative distribution. Commercial software may require a minimum of twelve (12) samples to work. In many field development projects, the number of core samples can be as low as four (4), which significantly decreases the reliability of the synthetic distribution. In addition, sometimes the sample can be of poor quality: too far apart or too clustered, left-skewed. A practice employed by our engineers is to duplicate the samples so that the number of samples exceeds the threshold of commercial software. This is, however, an unproven practice with no scientific justification.

3. Case study setup

The case study focuses on net pay data from nearly 2,000 wells in gas fields across Southeast Asia, characterized by a lognormal

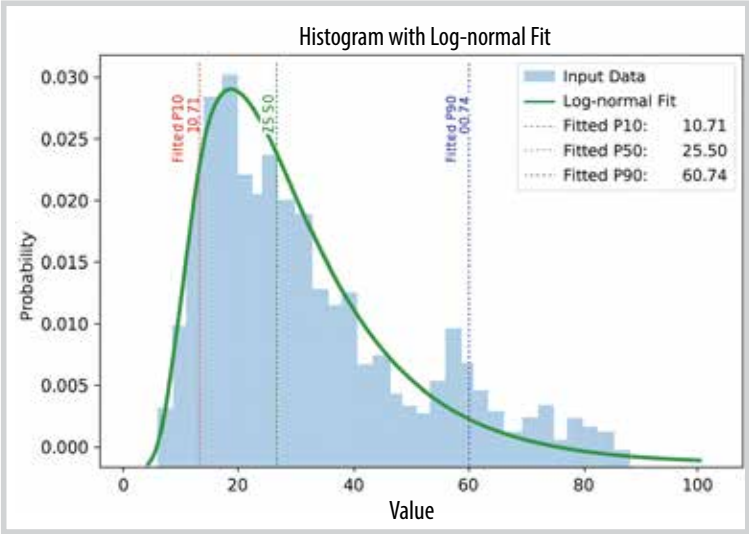

Figure 5. *Lognormal fitted curve.*

distribution. A smaller subset of 500 wells with similar geological and operational attributes to our operating fields has been selected and will be used for this case study. The net pay data for this population can be characterized by either lognormal, Johnson's SU, or Pearson III distribution, as shown in Figure 6. Currently the algorithm focuses on Pearson III and lognormal distributions. Future work may extend further to include more comprehensive distribution types.

All simulations are implemented in Python and executed on standard office machine, with no specialized software or hardware.

For the parameters range as input for M-ADRC (Table 1), this case study uses very wide range, much wider than the actual values as boundaries:

The simulation parameters are listed in Table 2.

The flowchart for validation process is presented in Figure 7. Detailed explanation is as follows:

Sample selection: A number of random samples were drawn from the 500-well dataset.

Simulation: The M-ADRC algorithm and traditional lognormal-based spreadsheet approach (LSA) were executed to generate the percentage point function (PPF).

Validation: The PPF generated from the proposed algorithm and spreadsheet method were validated against actual population using two metrics:

Wasserstein distance (WD): Also known as Earth Mover's distance, measures distance between two probability distributions. It is widely used in uncertainty quantification (Scheidt and Caers, 2009). The common form is the 1-Wasserstein distance:

$$W_1(P,Q) = \int_0^1 \left|F_p^{-1}(q) - F_Q^{-1}(q)\right| dq$$

Table 1. Distribution parameters used by M-ADRC

Distribution parameters	Range	Actual population value
α (Pearson III)	0 - 40	1.2
μ (Pearson III)	0 - 2,000	138
β (Pearson III)	0 - 2,000	89
Population mean	20 - 300 (95th percentile)	138
μ (Lognormal)	3 - 6.4	4.9
σ (Lognormal)	0-2	0.7

Where q is the quantile and F^{-1} (q) is the quantile function. Two identical distributions will have a distance that equals zero. The unit of Wasserstein distance is the same as the unit of the distribution. For this study, Wasserstein distance between the PPF of the synthetic and actual population will be compared. A "decent" WD score depends on the magnitude of the distributions. Figure 8 shows that for this dataset, a WD score of 25 or less can be considered excellent, as the synthetic population accurately represents actual population.

Swanson's mean (SM): Is an empirical approximation of mean for lognormal or moderately right-skewed distribution based on P10, P50, and P90. The most common formula in oil and gas [24] is:

$$Swanson's\ Mean = 0.3P_{10} + 0.4P_{50} + 0.3P_{90}$$

For this study, the relative difference between SM of synthetic and actual population will be recorded. It is calculated as:

$$\%\ Relative\ Difference = \left|\frac{Synthetic - Actual}{Actual}\right| \times 100$$

Iteration: The process was repeated 1,000 times to assess robustness, with results recorded for statistical analysis.

Repeat: Repeat the entire process but with a higher number of samples. This study will demonstrate an analysis for number of samples from 4 to 12.

4. Results and discussion

4.1. Wasserstein distance

Figure 9 shows the median Wasserstein distance between actual PPF of the true

Table 2. Simulation parameters

Simulation parameters	Value
Proposal α	0.1
Proposal μ (Pearson III)	0.5
Proposal β	0.5
Proposal μ (Lognormal)	0.4
Proposal σ	0.4
n_iteration	10,000
Burn-in	1,000

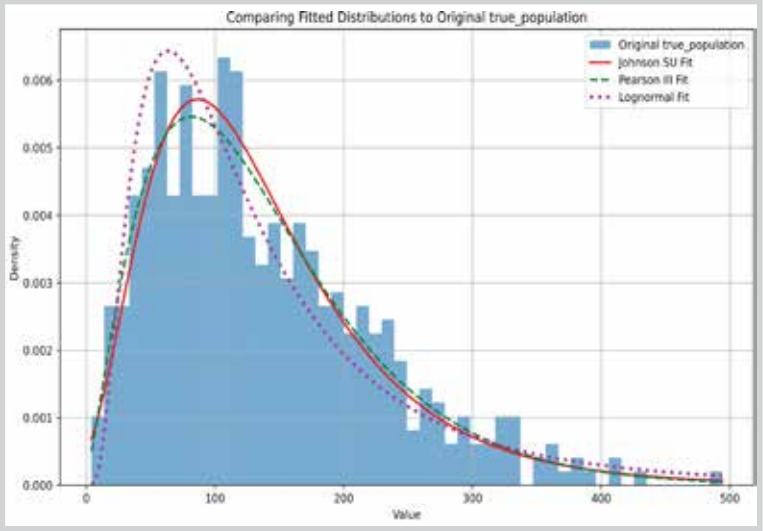

Figure 6. Compare distribution types to data.

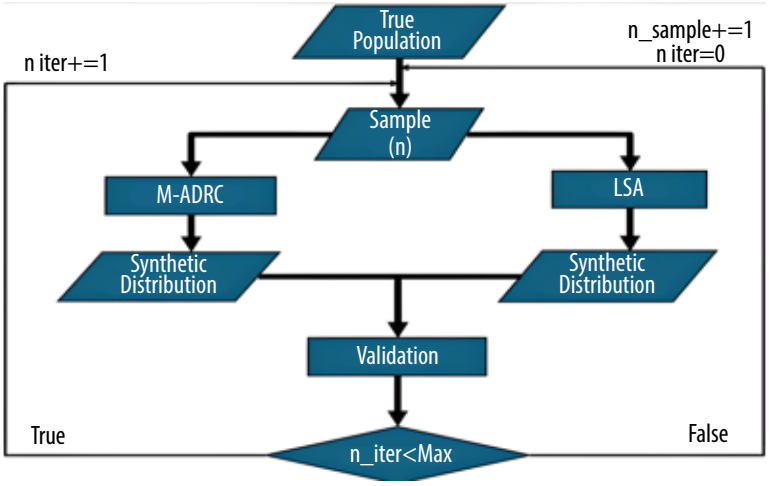

Figure 7. Workflow for the case study.

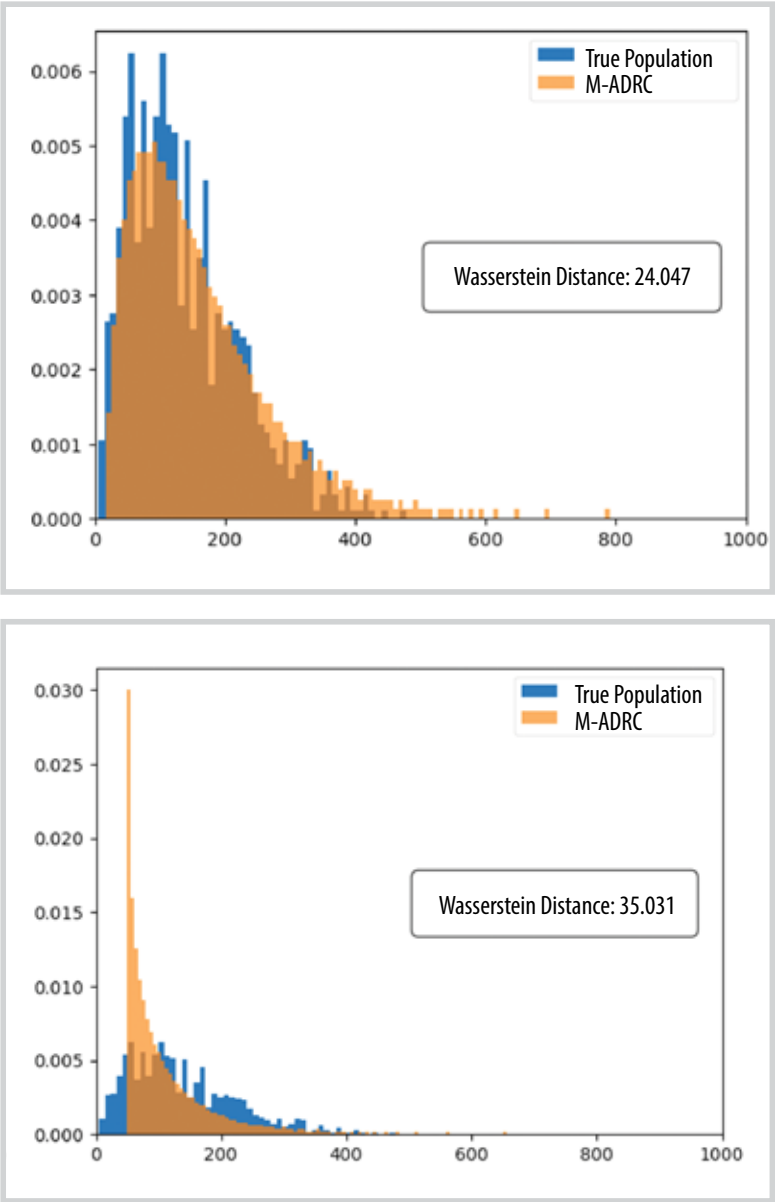

Figure 8. *Example of Wasserstein distance between synthetic and actual population.*

population and synthetic PPF generated from M-ADRC and LSA with increasing number of samples. Each data point represents the median WD value for 1,000 simulation cases with different samples. M-ADRC demonstrates superiority over conventional LSA method. If we consider a Wasserstein distance of 25 as the threshold for excellent representation, then M-ADRC reaches this threshold at around 8 samples, while LSA needs 16 - 18 samples.

Figure 10 further demonstrates the percentage of cases in each run where M-ADRC outputs lower Wasserstein distance value than LSA. To prove its effectiveness, M-ADRC needs to demonstrate improvement in comparison to LSA for more than 50% of cases. The results show that M-ADRC exceeds this threshold by a wide margin, starting at nearly 70% and increasing further as the number of samples grows.

4.2. Swanson's mean

Similar to Wasserstein distance, M-ADRC also shows significantly improved performance in terms of Swanson's mean difference compared to LSA. Figure 11 plots the median relative difference of Swanson's mean between the actual population and synthetic distribution generated from M-ADRC and LSA. Each data point is the median relative difference for 1,000 simulation cases. Although M-ADRC continues to outperform LSA, the performance gap narrows as sample size increases. This is expected because estimating a distribution's mean via Swanson's mean is far less demanding than modeling the full distribution using the Wasserstein distance.

Figure 12 plots the percentage of cases where M-ADRC outperforms LSA in Swanson's mean relative difference metric for different number of samples. The gap between two methods remains relatively constant rather than widening as seen in Figure 10. Nevertheless, M-ADRC maintains at least 60% ratio across all runs.

Results of the case study clearly demonstrate the vast improvement of M-ADRC compared to conventional lognormal spreadsheet approach (LSA) in representing the true population based on a small number of samples. By integrating an advanced MCMC algorithm with adaptive tuning, range restrictions, and distribution switch, M-ADRC is established as a state-of-the-art algorithm, capable of providing reliable synthetic distribution.

4.3. Limitations

The approach requires domain knowledge to limit the range of distribution parameters, especially the mean value. At current stage of development, the algorithm still lacks capability to effectively handle extreme sampling bias. Poor sample selections significantly reduce the

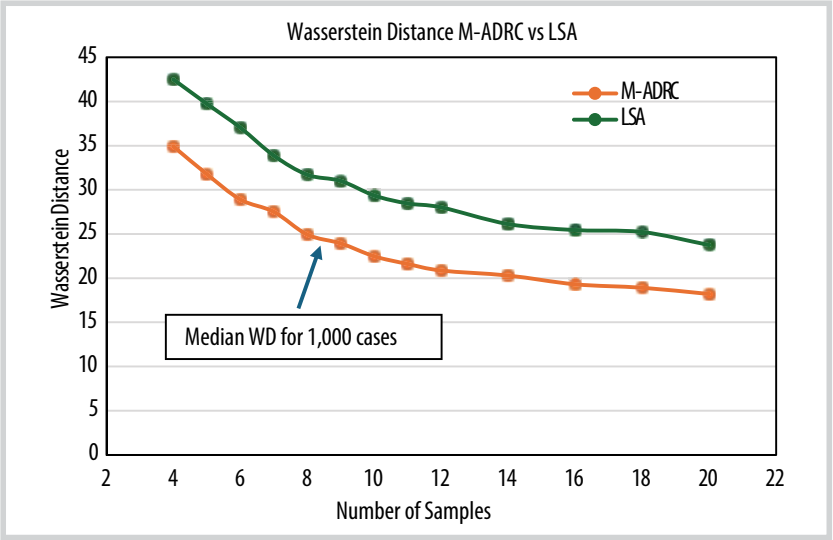

Figure 9. *Median Wasserstein distance between synthetic and actual population: M-ADRC vs LSA.*

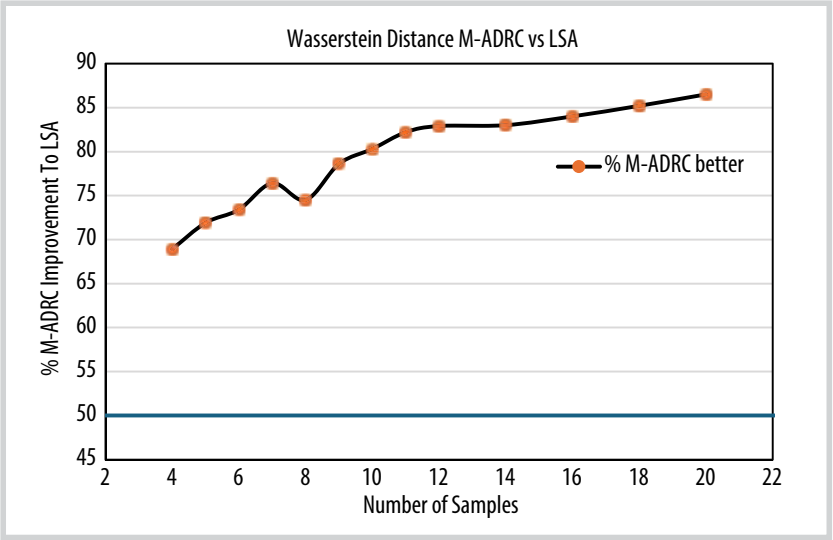

Figure 10. *Percentage of cases where M-ADRC yields improved results to LSA - Wasserstein distance.*

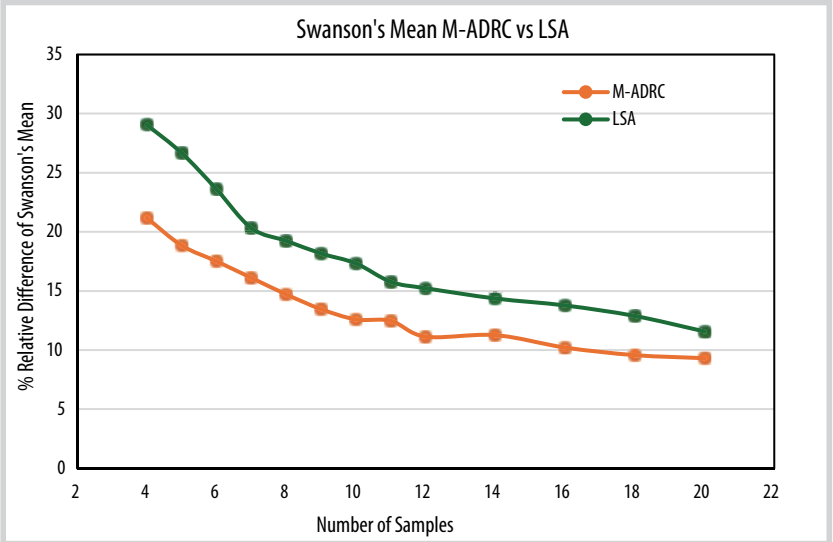

Figure 11. *Median % relative difference of Swanson's mean between synthetic and actual population: M-ADRC vs LSA.*

performance of the algorithm. Figure 13 illustrates that when input samples differ substantially from the true population distribution, the resulting synthetic population will poorly represent the actual population. Furthermore, the workflow does not take into account geospatial properties.

- Web applications

The algorithm is packaged into a web-based solution consisting of two applications (Figure 14): Metropolis sampling to create a synthetic population, and best fit to fit distribution parameters to the synthetic or actual population.

The web application offers several advantages:

+ Accuracy: Robust sampling with only six samples, reducing data requirements.

+ Scalability: Applicable to other parameters (e.g., porosity, water saturation) with similar distributions.

+ Usability: Intuitive interface accessible to non-expert users, with automated parameter estimation.

- Metropolis sampling

The web application is designed to streamline the application of the Metropolis algorithm for reservoir engineers and geophysicists, even those without extensive computational expertise. The workflow includes:

Data Input: Users upload a .csv file containing formation parameter data (e.g., net pay, porosity, water saturation). The file must include a header row and numeric columns, with missing values handled via imputation or exclusion.

Parameter Selection: Users select a numeric column (e.g., "Net_Pay") and a distribution function (e.g., lognormal, Gaussian) from a dropdown menu.

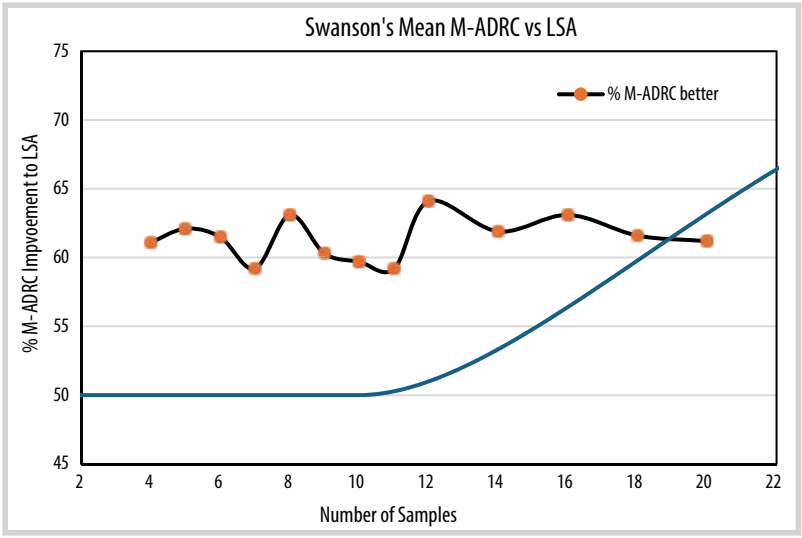

Figure 12. *Percentage of cases where M-ADRC yields improved results to LSA - Swanson's mean.*

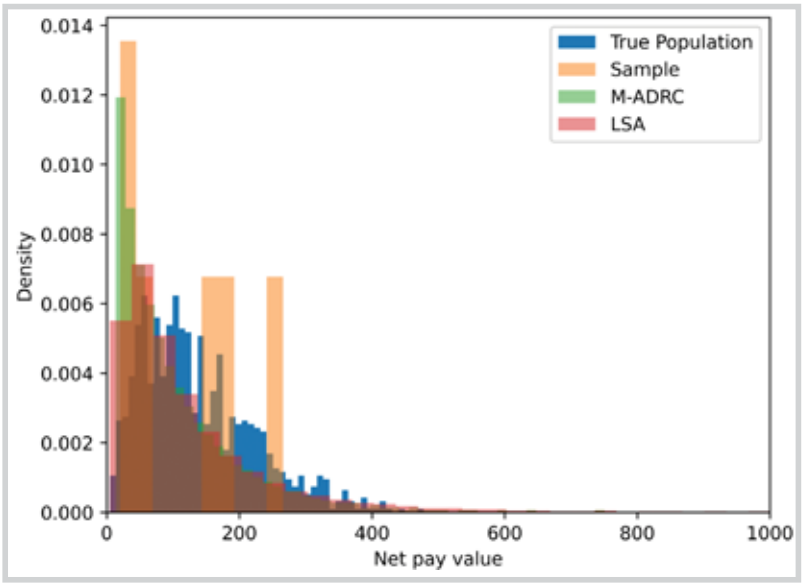

Figure 13. *Effect of poor sampling on synthetic population generation.*

The application estimates distribution parameters (e.g., μ, σ for log-normal) using maximum likelihood estimation.

Sampling Process: A "Run Sampling" button triggers the metropolis algorithm. The application runs N iterations with a burn-in of 10% of N, generating a synthetic population of 90%N samples.

Output and Validation: Results are displayed as a histogram of the synthetic population alongside the input data distribution. Users can download the synthetic data as a .csv file for further analysis (e.g., in reservoir simulation software).

The application is built using Streamlit framework with a Python backend, ensuring scalability and ease of deployment (Figure 15).

- Best fit application

The best fit application is designed to take a population as input, fit a distribution type (normal, lognormal, triangular) to the population, generate fitted parameters, and compare the fitted distribution to the actual distribution. Figure 16 demonstrates the workflow of the application:

Data Input: Users upload a .csv file containing the population.

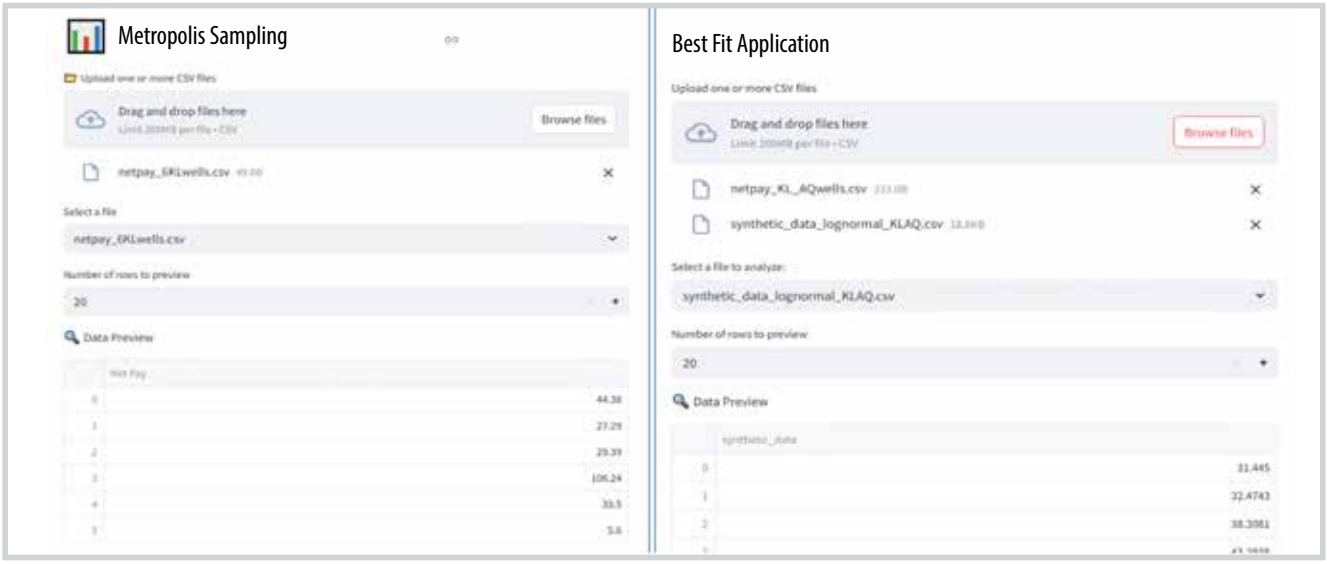

Figure 14. *The solution consists of two applications: Metropolis Sampling and Best Fit.*

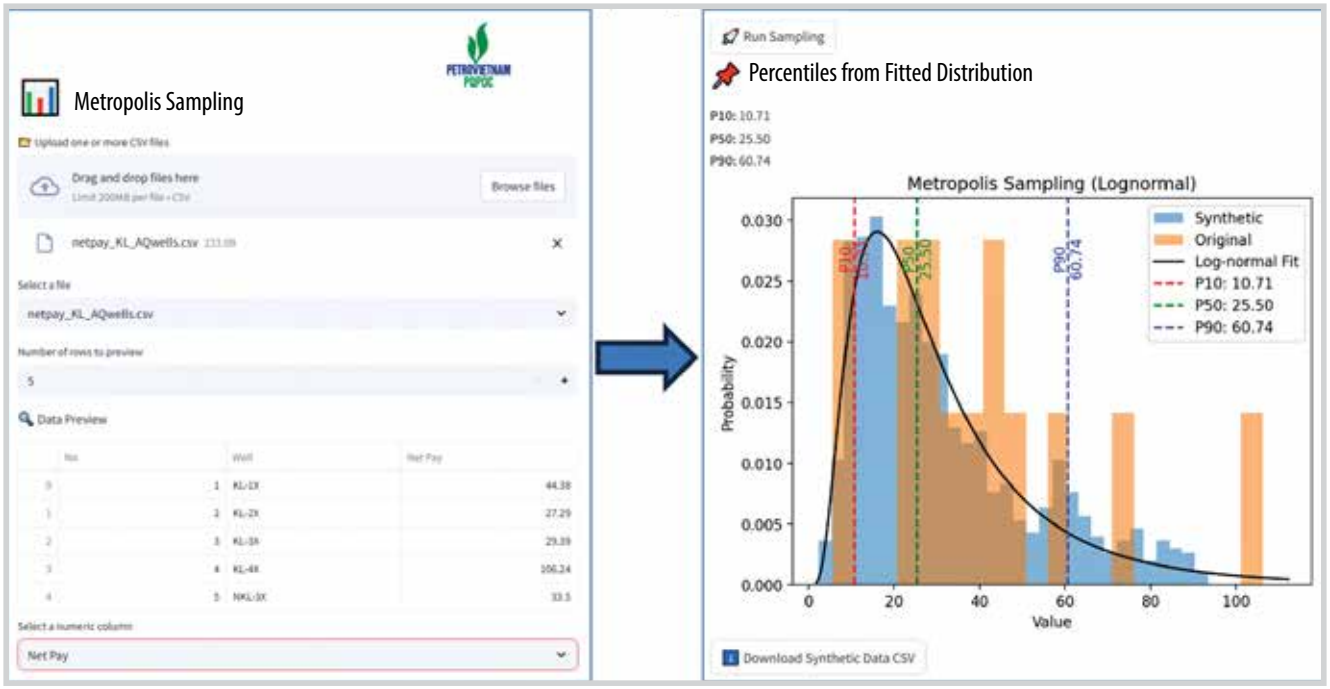

Figure 15. *Metropolis Sampling output.*

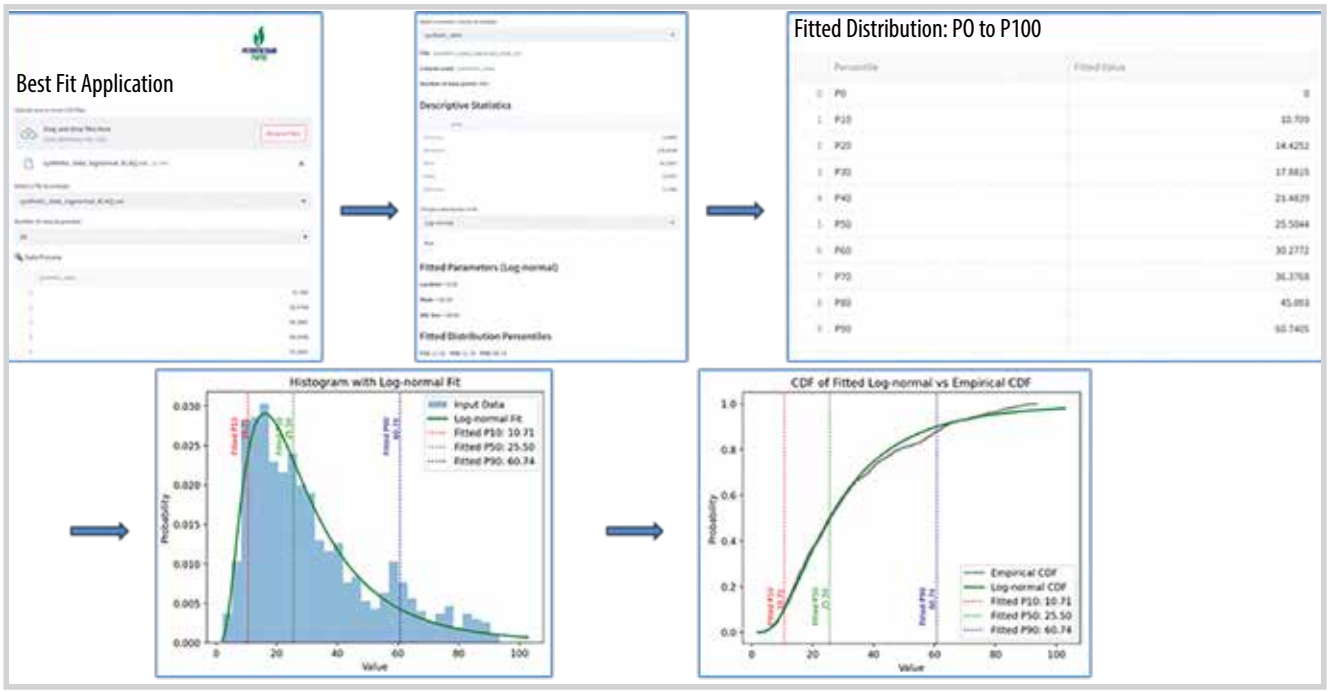

Figure 16. *Best Fit Application workflow.*

Parameter Selection: Users select a numeric column (e.g., "Net_Pay") and a distribution function (e.g., log-normal, normal, triangular) from a dropdown menu. The application displays descriptive statistical information and estimates distribution parameters.

Fit Process: A "Find best fit" button triggers the curve fitting process. The application finds the best fit parameters for the input population and the chosen distribution type.

Output and Validation: Results are displayed as a histogram of the input population alongside the fitted distribution. Cumulative density function (CDF) plot of the population and the fitted distribution is also presented. Users can download the output as a .csv file for further analysis.

5. Conclusions and recommendations

This study presents M-ADRC, an adaptive Metropolis-Hastings workflow with range constraints, adaptive tuning, and automatic distribution selection

designed to deliver representative synthetic population from datasets with few samples. The workflow is tailored for lognormal and Pearson III distribution, which are commonly used to model reservoir properties such as porosity, net pay, saturation. Range restriction of the population relies on opinion of domain experts or analogy from similar areas. There are multiple failsafe mechanism designed to prevent infeasible results within the workflow.

Applied to net pay dataset from Southeast Asian gas fields, the M-ADRC consistently outperforms traditional lognormal spreadsheet-based approach in term of Wasserstein distance and Swanson's mean for all sample size. The workflow is lightweight, reproducible, and runs on standard desktop hardware. Key limitations include its reliance on reasonable parameter bounds, resilience to extreme bias in sampling, and restriction to two distribution families, in addition to negligence of geospatial properties. Future extensions could incorporate broader distribution families (e.g., Johnson SU), censored/error models, hierarchical pooling across fields, spatial correlation, and advanced samplers.

References

[1] Taiwo Oludele Osunrinde, Iloka Chiamaka, and Yawale Ahmad, "Field developmental plan analysis: a case study of 'x' reservoir", *Journal of Petroleum Exploration and Production Technology*, Volume 9, pp. 2185 - 2203, 2019. DOI: 10.1007/s13202-019-0622-0.

[2] C. Karacaer and M. Onur, "Analytical probabilistic reserve estimation by volumetric method and aggregation of resources", *SPE Hydrocarbon Economics and Evaluation Symposium, Calgary, Alberta, Canada*, *24 - 25 September 2012*. DOI: 10.2118/162875-MS.

[3] B.C. Craft, M.F. Hawkins, and Ronald E. Terry, *Applied petroleum reservoir engineering, second edition*. Prentice Hall PTR, 1991.

[4] Paul F. Worthington, "Net pay: What is it? What does it do? How do we quantify it? How do we use it?", *SPE Reservoir Evaluation & Engineering*, Volume 13, Issue 5, pp. 812 - 822, 2010. DOI: 10.2118/123561-PA.

[5] Tian Yang, Yingchang Cao, Yanzhong Wang, Keyu Liu, Chen He, and Shaomin Zhang, "Determining permeability cut-off values for net pay study of a low-permeability clastic reservoir: A case study of the Dongying Sag, eastern China", *Journal of Petroleum Science and Engineering*, Volume 178, pp. 262 - 271, 2019. DOI: 10.1016/j.petrol.2019.03.030.

[6] Annan Boah Evans, Abraham Aidoo Borsah, Chukwugozie Jekwu Ejeh, Asamoah Emmanuel, and Daniel Ocran, "Mapping of porosity, permeability and thickness distribution: Application of geostatistical modeling for the Jubilee oilfield in Ghana", *Scientific & Academic Publishing*, Volume 9, Issue 2, pp. 27 - 49, 2019. DOI: 10.5923/j.geo.20190902.01.

[7] Biswajit Thander, Anirbid Sircar, and G.P. Karmakar, "Hydrocarbon resource estimation: Application of Monte Carlo simulation", *IJLTEMAS*, Volume III, Issue IV, pp. 30 - 47, 2014.

[8] P.F. Worthington, "An electrical analog facility for hydrocarbon reservoirs", *SPE Annual Technical Conference and Exhibition, Dallas, Texas, 9 - 12 October 2005*. DOI: 10.2118/96718-MS.

[9] Mohammad Bakhtiyari, Jafar Qajar, Amir Torghabeh, and Ali Dehghan Abnavi, "Rock typing and uncertainty assessment in geological and petrophysical properties by integrating electrofacies, hydraulic flow units, and geostatistical techniques in the Kangan gas field, Zagros basin", *Acta Geophysica*, Volume 72, pp. 2323 - 2347, 2023. DOI: 10.1007/s11600-023-01214-1.

[10] GhojehBeyglou and MohammadHossein, "Geostatistical modeling of porosity and evaluating the local and global distribution", *Journal of Petroleum Exploration and Production Technology*, Volume 11, pp. 4227 - 4241, 2021. DOI: 11. 10.1007/s13202-021-01308-w.

[11] Mattia Aleardi, "Analysis of different statistical models in probabilistic joint estimation of porosity and litho-fluid facies from acoustic impedance values", *Geosciences*, Volume 8, Issue 11, 2018. DOI: 10.3390/geosciences8110388.

[12] Nicholas Metropolis, Arianna W. Rosenbluth, Marshall N. Rosenbluth, Augusta H. Teller, and Edward Teller, "Equation of state calculations by fast computing machines", *The Journal of Chemical Physics*, Volume 21, Issue 6, pp. 1087 - 1092, 1953. DOI:10.1063/1.1699114.

[13] T. Cui, C. Fox, and M.J. O'Sullivan, "Bayesian calibration of a large-scale geothermal reservoir model by a new adaptive delayed acceptance Metropolis Hastings algorithm", *Water Resources Research*, Volume 47, Issue 10, 2011. DOI: 10.1029/2010WR010352.

[14] Zhe Ban, Ali Ghaderi, Nima Janatian, and Carlos

F. Pfeiffer, "Parameter estimation for a gas lifting oil well model using Bayes' rule and the Metropolis-Hastings algorithm", *Modeling, Identification and Control*, Volume 43, Issue 2, pp. 39 - 53, 2022. DOI: 10.4173/mic.2022.2.1.

[15] Silpakorn Dachanuwattana, Wei Yu, and Kamy Sepehrnoori, "An efficient MCMC history matching workflow using fit-for-purpose proxies applied in unconventional oil reservoirs", *Journal of Petroleum Science and Engineering*, Volume 176, pp. 381 - 395, 2019. DOI: 10.1016/j.petrol.2019.01.070.

[16] Sufia Khatoon, Jyoti Phirani, and Supreet Singh Bahga, "Accelerated Bayesian inference-based history matching of petroleum reservoirs using polynomial chaos expansions", *Inverse Problems in Science and Engineering*, Volume 29, Issue 13, pp. 3086 - 3116, 2021. DOI: 10.1080/17415977.2021.1973455.

[17] Zhen Zhang, Xupeng He, Marwah AlSinan, Hyung Kwak, and Hoteit Hussein, "Robust method for reservoir simulation history matching using bayesian inversion and long-short-term memory network-based Proxy", *SPE Journal*, Volume 28, pp. 983 - 1007. DOI: 10.2118/203976-PA.

[18] Eckhard Limpert, Werner A. Stahel, and Markus Abbt, "Log-normal distributions across the sciences: Keys and clues", *BioScience*, Volume 51, Issue 5, pp. 341 - 352, 2001. DOI: 10.1641/0006-3568(2001)051[0341:LNDATS]2.0.CO;2.

[19] A.G. Journel, "The lognormal approach to predicting local distributions of selective mining unit grades", *Mathematical Geology*, Volume 12, Issue 4, pp. 285 - 303, 1980. DOI: 10.1007/BF01029417.

[20] William W.S. Chen, and Samuel Kotz, "The riemannian structure of the three-parameter gamma distribution", *Applied Mathematics*, Volume 4, Issue 3, pp. 514 - 522, 2013. DOI: 10.4236/am.2013.43077.

[21] Abdalrhman Abrahim Milad, Ibrahim Adwan, Sayf A. Majeed, Zubair Ahmed Memon, Munder Bilema, Hend Ali Omar, Maher G.M. Abdolrasol, Aliyu Usman, and Nur Izzi Md Yusoff, "Development of a hybrid machine learning model for asphalt pavement temperature prediction", *IEEE Access*, Volume 9, pp. 158041 - 158056, 2021. DOI: 10.1109/ACCESS.2021.3129979.

[22] Jeffrey S. Rosenthal, "Optimal proposal distributions and adaptive MCMC", Handbook of Markov Chain Monte Carlo, 2011.

[23] Babak Naghavi, James F. Cruise, and Kishore Arora, "Comparative evaluation of three estimators of the log Pearson type 3 distribution", *Transportation Research Record 1279*, pp. 103 - 112.

[24] A. Hurst, G.C. Brown, and R. Swanson, "Swanson's 30-40-30 rule", *AAPG Bulletin*, Volume 84, Issue 12, pp. 1883 - 1891, 2000. DOI: 10.1306/8626C70D-173B-11D7-8645000102C1865D.

[25] Caoxiong Li, Mian Lin, Lili Ji, and Wenbin Jiang, "Multiphase flow in tight sandstone: An improved application for 3D intermingled fractal model", *Journal of Petroleum Science and Engineering*, Volume 177, pp. 403 - 414, 2019. DOI: 10.1016/j.petrol.2019.02.030.

[26] Sarah Lee, "Monte carlo simulation in petroleum engineering: A comprehensive guide to uncertainty analysis and risk assessment", 2025. [Online]. Available: www.numberanalytics.com/blog/monte-carlo-simulation-petroleum-engineering.

[27] Li Li, Jie Yu, Tao Huang, Lina Tang, Dan Wei, Mingyu Li, and Xin Nie, "Integrated net pay cut-off evaluation workflow for tight sandstone reservoirs: A case study of the linxing gas field, ordos basin", *Frontiers in Earth Science*, Volume 13, 2025. DOI: 10.3389/feart.2025.1488079.

[28] Kevin P. Murphy, *Machine learning: A probabilistic perspective*. The MIT Press Cambridge, Massachusetts London, England, 2012.

[29] Oracle, Crystal Ball User's Guide, 11.1.2.4.850, 2017[Online]. Available: https://docs.oracle.com/cd/E57185_01/CYBUG/CYBUG.pdf.

[30] Mehdi Qassamipour, Elnaz Khodapanah, and Seyyed Alireza Tabatabaei-Nezhad, "A comprehensive method for determining net pay in exploration/development wells", *Journal of Petroleum Science and Engineering*, Volume 196, 2021, DOI: 10.1016/j.petrol.2020.107849.

[31] Céline Scheidt and Jef Caers, "Uncertainty quantification in reservoir performance using distances and Kernel methods - Application to a West Africa deepwater turbidite reservoir", *SPE Journal*, Volume 14, Issue 4, pp. 680 - 692, 2009. DOI: 10.2118/118740-PA.

PETROVIETNAM
SCIENCE, TECHNOLOGY & INNOVATION PETROVIETNAM

EXPERIMENT SIMULATING THE WASHED-OUT BEHAVIOR OF ALKYLPHENOLS DURING WATERFLOODING

Huynh Thi Thu Huong[1], Nguyen Huu Quang[1], Le Van Son[1], Nguyen An Son[2]
[1]Centre for Applications of Nuclear Technique in Indusry, Vietnam Atomic Energy Institute
[2]Dalat University
Email: huonghtt@canti.vn
https://doi.org/10.47800/PVSI.2025.06-05

Summary

The contact of injection water and crude oil during the water injection process leads to the leaching of water-soluble phenolic compounds available in oil composition. The rate of decline in alkylphenol concentration in the injection water due to leaching depends on many factors related to the oil - water partition coefficient, oil saturation, interstitial velocity of phases, and dispersion coefficient.

This paper presents an experimental study combined with an analytical model to evaluate the relationship between washed-out rate and partition coefficients of some short-chain alkylphenols during oil - water interaction. The water - oil displacement experiment was carried out on a column packing glass beads, in which the packed column was initially saturated with Su Tu Nau crude oil at a temperature of 40°C. Our research results show that in a given flow regime the washed-out rate of alkylphenols differentiates from each other mainly due to the partition coefficient, thereby suggesting the possibility of using alkylphenols as a tracer to determine residual oil saturation in the sweeping area of the injection water.

Key words: Alkylphenol, partition coefficient, washed-out rate, oil saturation.

1. Introduction

Short-chain alkylphenols (C_0 - C_3) are commonly found in organic sedimentary compounds, including crude oil. In the 1990s, the initial presence of alkylphenols in crude oil was believed to originate from alkylation reactions and isomerization of precursor compounds in source rocks during the petroleum formation process. However, this approach did not explain the origin of all the observed alkylphenols in crude oil [1 - 3]. Recently, a wealth of experimental evidence suggests that the formation of alkylphenols may be linked to the hydroxylation of alkylbenzenes catalyzed by Lewis acids in sedimentary environments [4 - 6]. Accordingly, depending on the source of organic matter, the concentration of alkylphenols in crude oil varies significantly [7, 8]. After formation, the concentration and relative proportions of alkylphenol isomers are primarily controlled by partitioning between phases [9, 10]. The presence of the hydroxyl group in the molecule makes alkylphenols readily distribute from the oil phase to the water phase and mineral matrix both at the surface and subsurface conditions. The concentration of phenol (C_0) and cresols (C_1) in water tends to dominate over C_2 - C_3 alkylphenols, while higher isomers are typically more abundant in oil. Laboratory studies on the oil - water partition properties of alkylphenols had been conducted by Taylor, Bennett, and Larter [11, 12].

The impact of partitioning on the concentration of alkylphenols during the interaction of oil with injected water in the exploitation process, more specifically, results in alkylphenols being washed away from the oil phase into the water phase at the oil - water interface, leading to a gradual decrease over time in their concentration in both phases [13]. The rate of decrease in concentration (or wash-out rate) of alkylphenols in the produced water provides information about fluid velocity, oil - water interaction process, and oil saturation. The efforts to harness the potential use of alkylphenols as natural tracers in assessing oil saturation and determining the contribution of injection wells to production wells have been carried out by the Tracer Laboratory at the Center

Date of receipt: 23/2/2024.
Date of review and editing: 23/2/2024 - 27/1/2025.
Date of approval: 27/1/2025.

for Applications of Nuclear Technique in Industry (CANTI) for several years [14, 15]. Recently, an analytical model describing the transport of alkylphenols as they leach from oil phase into water phase during waterflooding has been proposed by Huong et al [16]. Currently, this study investigates the correlation between the wash-out rate and the partition coefficient of alkylphenols regarding their concentration history using both analytical and experimental models. Validating the above correlation will form the basis for proposing a methodology to determine residual oil saturation by matching the production profiles of alkylphenols with a mathematical model.

2. Materials and methods

2.1. Laboratory column experiment

A laboratory experiment to simulate the leaching process of alkylphenols was conducted through a water - oil displacement regime on a column packing glass beads. The experimental setup is presented in Figure 1, under experimental conditions at a temperature of 40°C and atmospheric pressure.

The physical model used in this study is a stainless steel column (SS316L) with a length of 30.5 cm and an inner diameter of 1.57 cm. The column is packed with laboratory-grade glass beads with an average diameter of 100 - 150 µm and a bulk density of 2.7 g/cm^3. The porosity of the packed column is 41.2%, corresponding to a pore volume (PV) of 24.3 cm^3.

At the initial conditions, the packed column is saturated with Su Tu Nau crude oil (°API = 39.8). The density of the crude oil under experimental conditions is 0.82 g/cm^3. The crude oil contains six alkylphenol compounds, including phenol (P), 4-methylphenol (4MP), 2-methylphenol (2MP), 3,4-dimethylphenol (34DMP), 2,4-dimethylphenol (24DMP), and 4-ethylphenol (4EP), with initial concentrations ranging from 100 to 500 mg/L. Laboratory-grade deionized water is used as the injection fluid in this experiment. The density of the water under experimental conditions is 0.992 g/cm^3. The partition coefficients (K_d) of the alkylphenol compounds (APs) are measured under static contact between the oil - water phases at the experimental conditions.

The deionized water is pumped into the saturated oil column at a flow rate of 0.3 mL/min, and the water sample is collected separately over time until it almost reaches the state of residual oil saturation (66.8%) at a cumulative injection volume of 11 PV (pore volume). The concentration of alkylphenols in water samples is analyzed using a Dionex UltiMate 3000 high-performance liquid chromatography (HPLC) system with a DAD detector and a C_{18} column at the Laboratory of Physical Chemistry (VILAS-609) of the Center for Applications of Nuclear Technique in Industry (CANTI). The detection limit is approximately 10^{-7}, with a 95% confidence level and a measurement error of 3 - 5%. The analysis procedure for these alkylphenols was researched and completed by CANTI as part of the project funded by Vietnam's Ministry of Science and Technology [17]. Under the analytical conditions, the chromatogram on HPLC/DAD shows good separation for the six alkylphenol compounds, including phenol (P), 4-methylphenol (4MP),

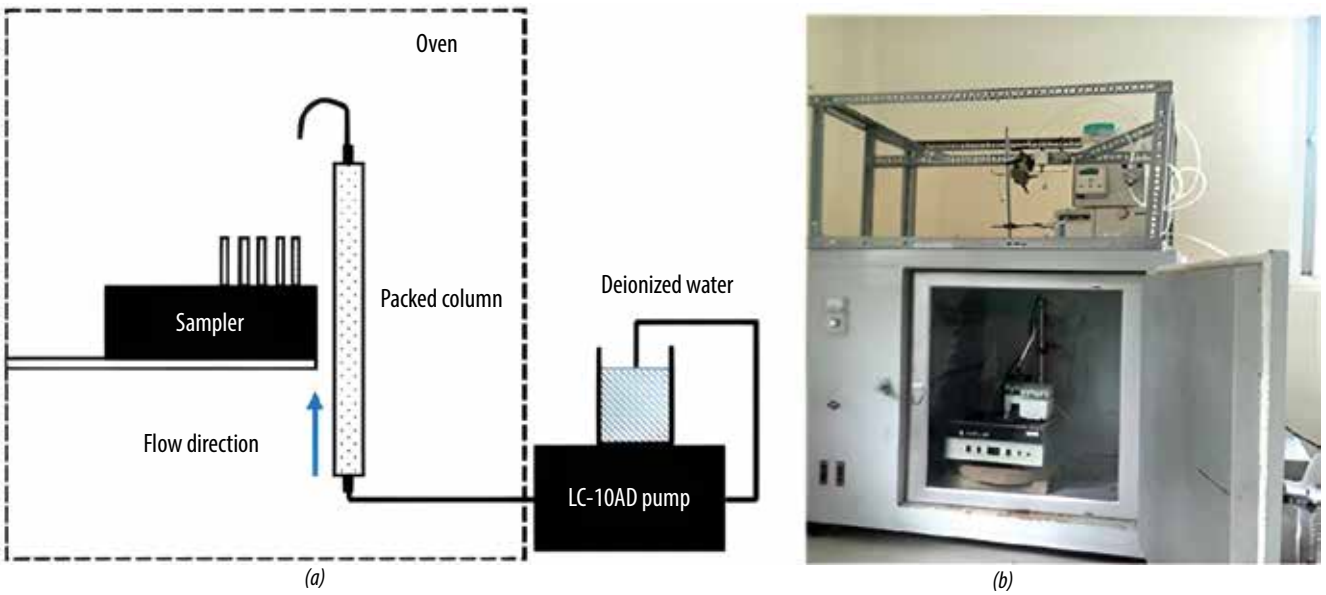

Figure 1. *Experimental setup diagram (a) and the experimental system at the Tracer Laboratory (CANTI) (b).*

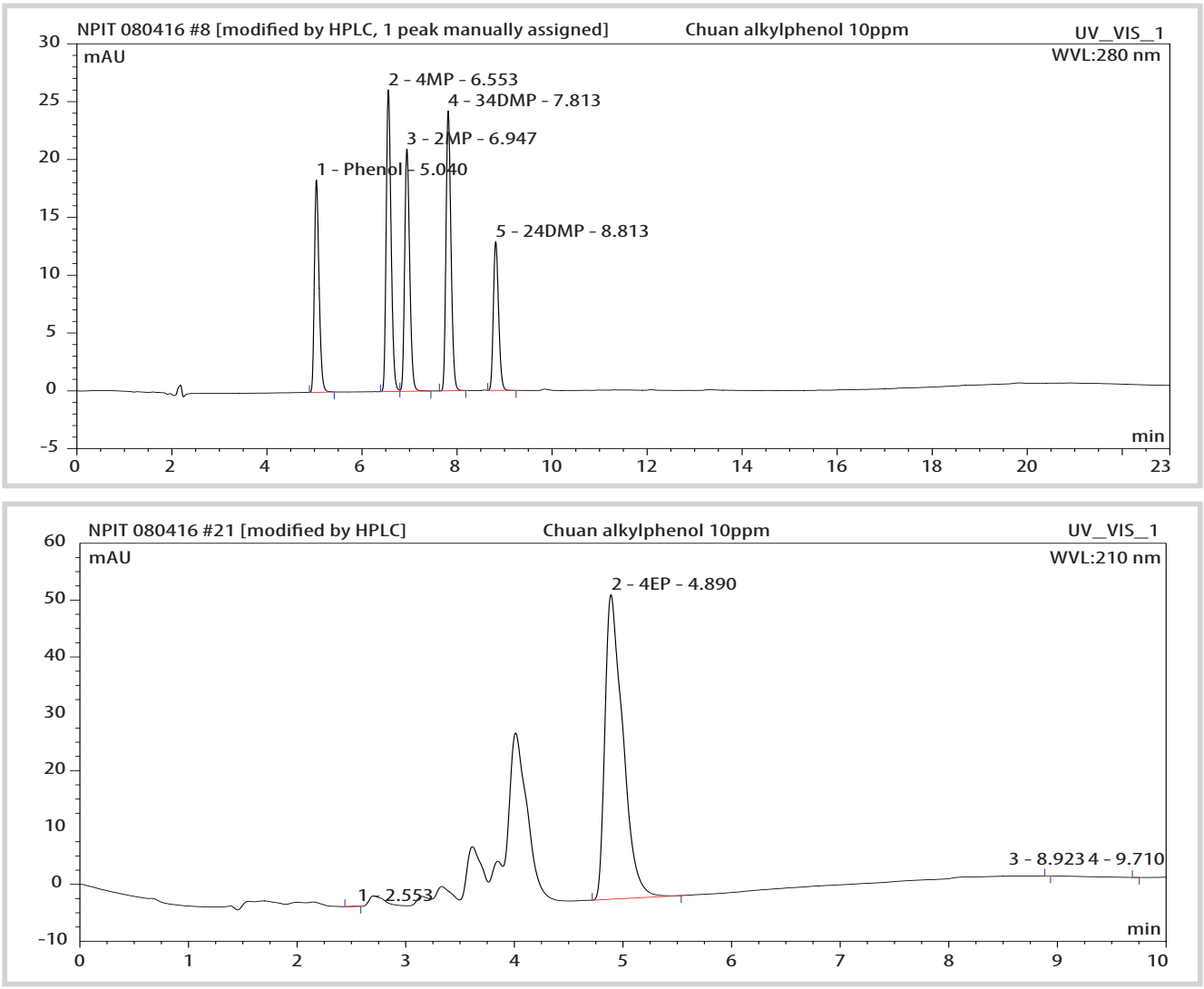

Figure 2. *Chromatographic analysis of standard samples of six alkylphenol compounds, including phenol (P), 4-methylphenol (4MP), 2-methylphenol (2MP), 3,4-dimethylphenol (34DMP), 2,4-dimethylphenol (24DMP), and 4-ethylphenol (4EP), on HPLC/DAD.*

2-methylphenol (2MP), 3,4-dimethylphenol (34DMP), 2,4-dimethylphenol (24DMP), and 4-ethylphenol (4EP), as illustrated in Figure 2.

2.2. Analytical model

Analytical model is used to analyze the leaching process of alkylphenols obtained from the experiment.

The transport of alkylphenols in porous media can be modeled using the advection-dispersion equation with a term of partitioning instantaneously between oil and water phases [18]. Suppose that the porous media is infinite homogeneous, the saturation of the two phases is constant, and the interstitial velocity of phases is constant in the pore, a one-dimensional (1D) analytical solution describing the concentration of alkylphenols in water phase $C_w(x, t)$ is expressed as equation (1) [16]:

$$\frac{C_w(x,t)}{C_0} = \frac{1}{2} \times \left[1 + Erf\left(\frac{x - \frac{C^*}{A} \times t}{2 \times \sqrt{\frac{B \times t}{A}}} \right) \right] \quad (1)$$

In which, C_0 is the initial concentration of alkylphenol in water phase [M/L^3]; A, B and C* are parameters depending on alkylphenol partition coefficient, oil saturation, dispersion coefficient in phases, and pore velocity of water and oil:

$$A = 1 + (K_d - 1) \times S_o$$

$$B = (1 - S_o) \times D_{Lw}^* + K_d \times S_o \times D_{Lo}^*$$

$$C^* = (1 - S_o) \times v_{wx}^* + K_d \times S_o \times v_{ox}^*$$

C_w is the alkylphenol concentration in water phase [M/L^3]; So is the saturation of oil phase (S_w = 1 - S_o is the saturation of water phase); K_d is the alkylphenol

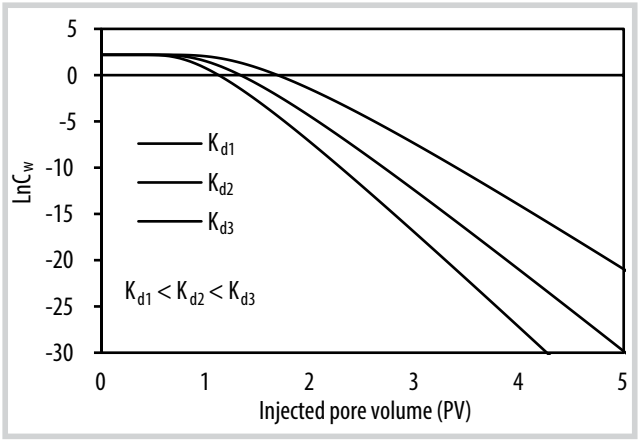

(a)

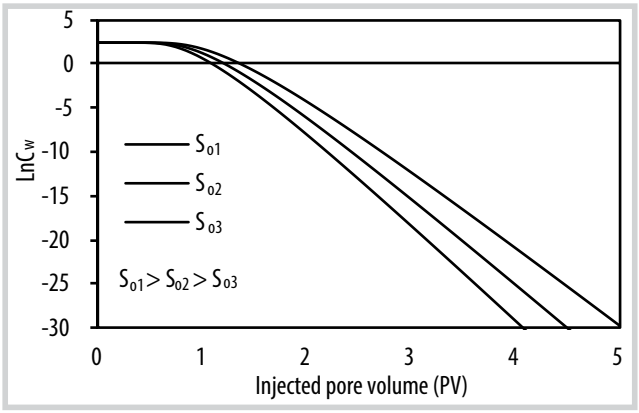

(b)

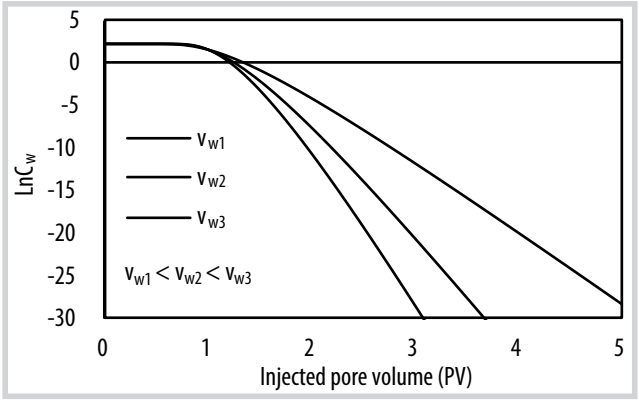

(c)

Figure 3. *Influence of the partition coefficient (a), oil saturation (b) and water interstitial velocity (c) on the decrease of LnCw according to the injected pore volume.*

partition coefficient defined as the ratio of alkylphenol concentration in oil phase and water phase at equilibrium conditions; v_w and v_o are the interstitial velocity of water phase and oil phase, respectively [L/T]; D_{Lw} and D_{LO} are the dispersion coefficient of alkylphenol in water phase and oil phase, respectively [L^2/T]; t is time [T]. When the injected volume is sufficiently large, LnC_w becomes nearly linear over time, with the slope of $\frac{C^{*2}}{4 \times A \times B}$ $[T^{-1}]$ representing the wash-out rate (a) of alkylphenols during water sweeping.

The analytical solution above shows a good agreement with the results of the numerical simulation of ¼ 5-spot model using the UTCHEM simulator [16]. The wash-out rate is inversely proportional to the partition coefficient of alkylphenols and the oil amount within the sweep zone of the injection water (as shown in Figure 3a, 3b). The increase in interstitial velocity of the water phase enhances the bulk movement of alkylphenols and mechanical dispersion related to local velocity variations in pore space. As a result, alkylphenols can be washed away more rapidly, as illustrated in Figure 3c. The typical interstitial velocity of the water phase during waterflooding in an oil field is approximately 10^{-5} m/s; under these circumstances, molecular diffusion does not significantly influence the transport of solutes within the reservoir [19, 20].

3. Results and discussion

Initial concentrations of six alkylphenol compounds in the oil phase and their partition coefficients (K_d) at the experimental conditions are detailed in Table 1.

The process of displacing oil by water occurs over more than 14 hours, corresponding to an injection volume of 11 PV (pore volume). The water cut and oil saturation are plotted as functions of time in Figure 4a. The state of residual oil saturation is considered the condition where the remaining oil is trapped in the pore space and cannot be further recovered under the same injection conditions. In this experiment, the residual oil saturation is considered to reach 66.8% when there is a 1% difference between two consecutive oil saturation values.

The relative concentration (C/C_0) of six alkylphenols in water phase at the column outlet over injection time are shown in Figure 4b; C is the alkylphenol concentration and C_0 is the alkylphenol concentration at the beginning of water injection. The data show that the concentration of alkylphenols in the water phase gradually decreases during the injection, as depicted in Figure 4b. In a such clear representation, the decrease in the concentration of alkylphenols differentiates from each other. This washed-out rate characterizes the interaction between oil and water and can be analyzed using analytical model.

The relative concentrations C/C_0 obtained from both the experiment and the analytical model in equation (1) are compared and contrasted, as expressed in Figure 5a. In equation (1), interstitial velocity and dispersion coefficient are defined as follow:

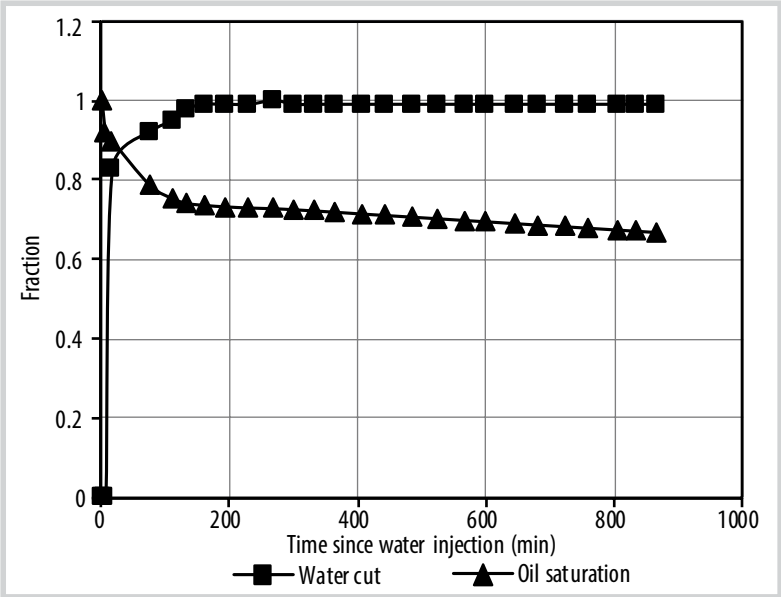

(a)

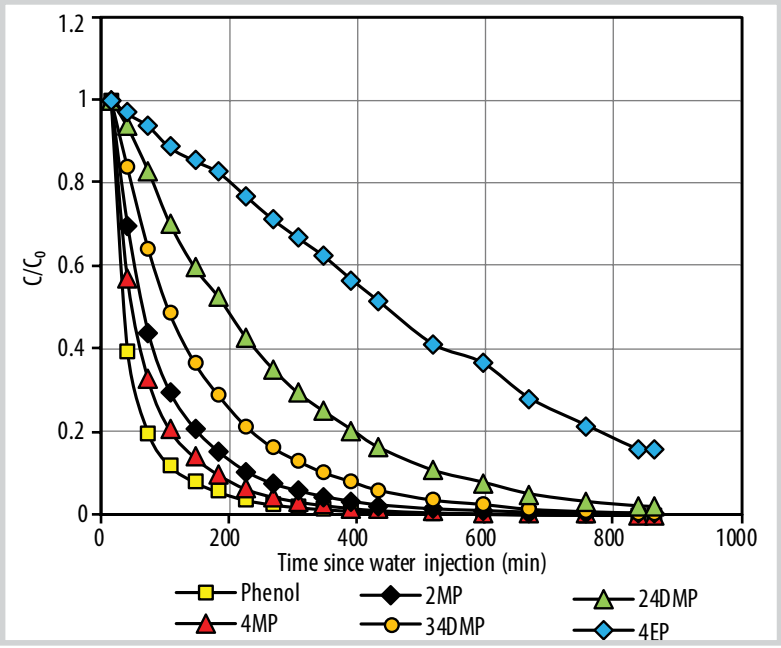

(b)

Figure 4. *Experimental results: Water-cut and oil saturation in fraction (a), and alkylphenol relative concentration in water phase at the column outlet over injection time (b).*

- Interstitial velocity of water phase (i = w) and oil phase (i = o) are determined as a function of flow rate (Q), phase fraction (f_i), cross-sectional area (A_s), porosity (ϕ) and phase saturation (S_i):

$$v_{xi}^{*} = \frac{Q \times f_i}{A_s \times \varphi \times S_i} \quad (2)$$

- Hydrodynamic dispersion of alkylphenols in water phase (i = w) and water phase (i = o) are expressed as equation (3):

$$D_{Li}^{*} = \frac{D_{m,i}}{F \times \varphi} + \alpha \times v_{xi}^{*1.2} \quad (3)$$

In which, $F = \phi^{-m}$ is the formation factor (m = 1.3 for glass-bead [21]); α is the dispersivity; v_i^* is the interstitial velocity of phase. This study utilizes the molecular diffusion coefficients of alkylphenol in water phase of $D_{m,w} = 7.8 \times 10^{-10}$ (m^2/s) and in oil phase of $D_{m,o} = 3.8 \times 10^{-10}$ (m^2/s) which are referenced from O. Huseby [18].

The root mean square error (RMSE) between the relative concentrations (C/C_0) obtained from the experiment and the analytical model falls within the range of 0.02 to 0.2 when the water cut, f_w, is close to unit (2 - 11 PV, corresponding to 162 - 864 minutes). Detailed results are presented in Table 2. The matching result also indicates the dispersivity of the porous media as α = 10 cm.

In the late stage of waterflooding (f_w is close to 1), the wash-out rate of alkylphenols (a) is quantified through the slope coefficient representing the linear relationship of $Ln(C_w)$ over time, with a maximum value of 0.009

Table 1. *The concentration of alkylphenols in the oil phase and their corresponding partition coefficients under experimental conditions*

APs	Partition coefficient $K_d = C_o / C_w$	Initial concentration in oil phase (mg/L)	Detection limit of APs in water phase (mg/L)
Phenol	1.0	134	0.03
4-methylphenol (4MP)	1.3	128	0.06
2-methylphenol (2MP)	1.5	137	0.03
3,4-dimethylphenol (34DMP)	2.1	194	0.10
2,4-dimethylphenol (24DMP)	3.1	291	0.04
4-ethylphenol (4EP)	7.5	491	0.05

(1/s) for phenol (K_d = 1.0) and a minimum value of 0.002 (1/s) for 4EP (K_d = 7.5). Thus, when examining the transport process of alkylphenols under identical conditions, a higher partition coefficient corresponds to a lower wash-out rate. The experimental results demonstrate a relationship of $a = 0.009 \times K_d^{-0.807}$ with a correlation coefficient $R^2 > 0.999$ (Figure 5b).

According to the above results, the analytical solution proposed by Huong et al. (2021) [16] provides a good description of the leaching process of alkylphenols from the oil phase to the water phase. The transport of alkylphenol compounds was experimentally studied by O. Huseby et al. (2003) [18], focusing on the diffusion process of these compounds from immobile bypassed oil during waterflooding. However, they demonstrated a collapse of the relative concentration data (C/C0) for the various compounds onto a single curve. Although the authors proposed semi-empirical equations describing the concentration decline of alkylphenol compounds over time during water injection using exponential functions, they did not clarify the contribution of dynamic parameters affecting this decline. Different from the above approach, the present experiment focuses on the leaching process of alkylphenols from residual oil in the sweeping area of the injection water. Based on the excellent agreement between the experimental data and the mentioned analytical solution [16], this study provides a clearer understanding of the factors influencing the decline in alkylphenol compared to the previous semi-empirical formula. This suggests that the residual oil saturation can be completely determined by matching the trendline of the wash-out rate of alkylphenols and their partition coefficients measured in the laboratory under reservoir conditions.

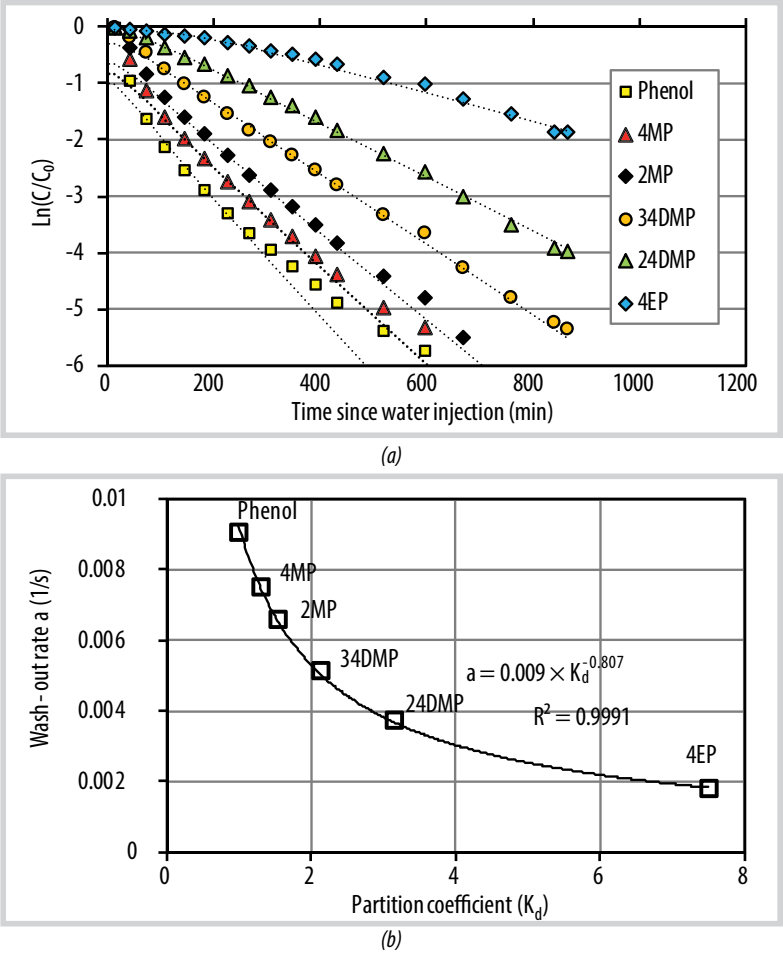

Figure 5. *The analytical solution (dashed line) describing the leaching process of alkylphenols in comparison to the experimental data points (a) and the wash-out rate of alkylphenols under experimental conditions (b).*

4. Conclusions

The leaching process of six alkylphenols naturally existing in crude oil into water has been studied experimentally in integration with analytical modeling. Initially, the packed glass-bead column was saturated with crude oil. During experimental water - oil displacement, the reduction rate of

Table 2. *The root mean square error (RMSE) between the relative concentrations (C/C_0) obtained from the experiment and the analytical solution during the injection stage (PV)*

PV	Phenol (K_d = 1.0)	4MP (K_d = 1.3)	2MP (K_d = 1.5)	34DMP (K_d = 2.1)	24DMP (K_d = 3.1)	4EP (K_d = 7.5)
0-2	0.46	0.48	0.47	0.43	0.33	0.22
2-4	0.06	0.06	0.06	0.20	0.10	0.20
4-6	0.06	0.07	0.05	0.09	0.06	0.13
6-8	0.05	0.05	0.04	0.06	0.05	0.05
8-11	0.03	0.02	0.02	0.02	0.02	0.06

alkylphenols concentration in water phase, acting as the wash-out rate, depends on the effect of partitioning the oil - water phases.

The experimental results are well-explained by a simple 1D analytical model when taking into account the partitioning process, especially at the late stage of waterflooding. The analytical model shows a clear relation between the wash-out rate of alkylphenols, partition coefficients, oil saturation, dispersion coefficients, and interstitial velocities. With the help of analytical model, the wash-out rate of alkylphenols under the experimental conditions shows an excellent agreement with partition coefficient in the form of a negative power function.

This shows that in cases where the wash-out rate of alkylphenols and their partition coefficients under reservoir conditions are known, the residual oil saturation in the sweeping area of the injection water can be estimated using the analytical model. The results here represent a first step toward a practical approach in using alkylphenols as natural tracers for estimating phase saturations in oil reservoirs. One of the key issues in the application is the analysis of the concentration of alkylphenols in the water phase under reservoir conditions at production wells. However, in reality, the water sample collected at the wellhead is under surface conditions, causing the concentration of alkylphenols in the collected sample to not reflect their actual value under reservoir conditions. Therefore, developing a method to convert the alkylphenol concentration in the wellhead sample to the concentration under reservoir conditions will be conducted and presented in future research, aiming to apply this method at a field-scale.

References

[1] P.N. Taylor, *"Thesis: the petroleum geochemistry of phenols"*, University Newcastle upon Tyne, 1994.

[2] Marisa Ioppolo-Armanios, Robert Alexander, and Robert I. Kagi, "Geosynthesis of organic compounds: I. Alkylphenols", *Geochimica et Cosmochimica Acta*, Volume 59, Issue 14, pp. 3017 - 3027, 1995. DOI: 10.1016/0016-7037(95)80001-8.

[3] Marisa Ioppolo - Armanios, *The occurrence and origins of some alkylphenols in crude oils*. Curtin University of Technology, 1996.

[4] Trevor P. Bastow, Ben G.K. van Aarssen, Geoff E. Chidlow, Robert Alexander, and Robert I. Kagi, "Small-scale and rapid quantitative analysis of phenols and carbazoles in sedimentary matter", *Organic Geochemistry*, Volume 34, Issue 8, pp. 1113 - 1127, 2003. DOI: 10.1016/S0146-6380(03)00066-4.

[5] Michael J. Borda, Alicia R. Elsetinow, Daniel R. Strongin, and Martin A. Schoonen, "A mechanism for the production of hydroxyl radical at surface defect sites on pyrite", *Geochimica et Cosmochimica Acta*, Volume 67, Issue 5, pp. 935 - 939, 2003. DOI: 10.1016/S0016-7037(02)01222-X.

[6] Trevor P. Bastow, Ben G.K. van Aarssen, Rober Alexander, and Rober I. Kagi, "Origins of alkylphenols in crude oils: Hydroxylation of alkylbenzenes", *Organic Geochemistry*, Volume 36, Issue 7, pp. 991 - 1001, 2005. DOI: 10.1016/j.orggeochem.2005.03.007.

[7] S. Zhou, H. Huang, "Controls on alkylphenol occurrence and distribution in oils from lacustrine rift basins in East China", *Science in China Series D: Earth Science*, Volume 51, Issue 7, pp. 976 - 983, 2008. DOI: 10.1007/s11430-008-0066-8.

[8] Li Su-mei et al., "Oxygenic compounds in crude oils-phenols", *Acta Petrol Sin (in Chinese)*, Volume 21, Issue 1, pp. 44 - 48, 2000. DOI: 10.7623/syxb200001008.

[9] Sandra O.Lucach, Bernard F.J.Bowler, Neil Frewin, and Steve R.Larter, "Variation in alkylphenol distributions in a homogeneous oil suite form the Dhahaban petroleum system of Oman", *Organic Geochemistry*, Volume 33, Issue 5, pp. 581 - 594, 2002. DOI: 10.1016/S0146-6380(02)00014-1.

[10] Trevor P. Bastow, Ben G.K. van Aarssen, Robert Herman, Robert Alexander, and Robert I. Kagi, "The effect of oxidation on the distribution of alkylphenols in crude oils", *Organic Geochemistry*, Volume 34, pp. 1103 -1111, 2003. DOI: 10.1016/S0146-6380(03)00067-6.

[11] Dennis Taylor, A. E. Kotorovich, A.I. Larichev, and M. Glikson, "Petroleum source rocks in the Roper Group of the McArthur Basin: Source characterization and maturity determinations using physical and chemical method", *APEA*, Volume 34, pp. 279 - 296, 1994. DOI: 10.1071/AJ93026.

[12] B. Bennett and S.R. Larter, "Partition behaviour of alkylphenols in crude oil/brine systems under subsurface conditions", *Geochimica et Cosmochimica Acta*, Volume 61, Issue 20, pp. 4393 - 4402, 1997. DOI: 10.1016/S0016-7037(97)88537-7.

[13] R.Sinha,K.Asakawa,G.A.Pope,andK.Sepehmoori, "Simulation of natural and partitioning interwell tracers to calculate saturation and swept volumes in oil reservoirs", *SPE/DOE Symposium on Improved Oil Recovery, Tulsa, Oklahoma*, 17 - 21 April, 2004. DOI: 10.2118/89458-MS.

[14] To Ba Cuong, Nguyen Hong Phan, and Nguyen Huu Quang, "Interwell tracer method using partitioning compounds naturally existing in crude oil for determination of residual oil saturation", *Petrovietnam Journal*, Volume 10, pp. 38 - 43, 2016.

[15] Huynh Thi Thu Huong, Le Thanh Tai, Nguyen Huu Quang, and Le Van Son, "Determination of contribution proportion of injection wells in oil production by interwell tracer method using partitioning organic compounds from crude oil", *Petrovietnam Journal*, Volume 6, pp. 24 - 29, 2019.

[16] Huynh Thi Thu Huong, Nguyen Huu Quang, Le Van Son and Tran Trong Hieu, "Transport of oil/water partitioning components during water injection", *Petrovietnam Journal*, Vol. 6, pp. 37 - 42, 2021. DOI: 10.47800/PVJ.2021.06-03.

[17] Nguyễn Hồng Phan, Nguyễn Hữu Quang, Tô Bá Cường, Huỳnh Thị Thu Hương, và nnk, *"Phát triển mô hình mô phỏng quá trình vận động của các chất chỉ thị tự nhiên (NPIT) để đánh giá trữ lượng dầu trong khai thác"*, Viện Năng lượng Nguyên tử Việt Nam, 2015.

[18] O. Huseby, A. Haugan, J. Sagen, J. Muller, B. Bennett, S.R. Larter, E.S. Kikkinides, A.K.Stubos, and F. Yousefian, Jean-Francois Thovert, and P.M. Adler, "Transport of organic components from immobile and bypassed oil in porous media", *Applied Chemical Engineering*, Volume 49, Issue 5, pp. 1085 - 1094, 2003. DOI: 10.1002/aic.690490504.

[19] Ann Muggeridge, Andrew Cockin, Kevin Webb, Harry Frampton, Ian Collins, Tim Moulds and Peter Salino, "Recovery rates, enhanced oil recovery and technological limits", *Philosophical Transactions of the Royal Society A*, Volume 372, Issue 2006, 2014. DOI: 10.1098/rsta.2012.0320.

[20] L. Lake, R.T. Johns, W.R. Rossen, and G.A. Pope, *Fundamentals of enhanced oil recovery*. Texas: Society of Petroleum Engineers, 2014.

[21] P. Martínez-Pagán, A. Jardani, A. Revil, and A. Hass, "Self-potential monitoring of a salt plume", *Geophysics*, Volume 75, Issue 4, 2010. DOI: 10.1190/1.3475533.

PETROVIETNAM SCIENCE, TECHNOLOGY & INNOVATION PETROVIETNAM

INCREASING THE FLASH POINT TEMPERATURE OF DCO OIL PRODUCTS TO MEET THE FO (FP) BASELINE STANDARD OF DUNG QUAT REFINERY

Nguyen Hoang Tri, Nguyen Chanh Quoc, Huynh Cong Vinh, Bui Anh Khanh, Ho Quang Xuan Nhan
Nguyen Huu Trung, Bui Van Vuot, Nguyen Thanh Bong
Binh Son Refining and Petrochemical Joint Stock Company
Email: Trinh@bsr.com.vn
https://doi.org/10.47800/PVSI.2025.06-06

Summary

The flash point temperature of decanted oil (DCO) has been consistently low since the Dung Quat refinery commenced operations in 2009. This issue is attributed to the absorption of trace amounts of light gases such as H_2, CH_4, and C_2H_6 by the liquid stream at the bottom of the tower. These gases cannot be effectively separated through distillation at T-1501, and neither modifications to hardware nor adjustments to the angle of the fifth packing layer have proven effective. The separation of these light gases can only be achieved by applying the stripping method to the DCO product stream emanating from the bottom of the tower and at D-1515. This method must ensure no alterations to existing hardware and utilize current equipment solely. The technique involves injecting N_2 directly into the liquid drum to remove light gases by reducing the partial pressure of hydrocarbons. This solution successfully increased the DCO flash point temperature from 49°C to 84°C in July 2018, and has been maintained to date. Furthermore, the flash point temperature can be regulated by the N_2 stream to exceed 100°C, thereby meeting and surpassing the technical requirement of 66°C.

Key words: DCO, flash point (FP), stripping, BSR, fuel oil, result, light component.

1. Introduction

The RFCC unit at the Dung Quat refinery, operated by Binh Son Refining and Petrochemical Joint Stock Company, is a key unit that converts residue fractions from the crude distillation unit (CDU) or the atmospheric distillation unit into lower-boiling point and higher-economic value products through catalytic cracking process.

The products of the RFCC unit include:

Primary products:

- LPG;
- Naphtha;
- Light cycle oil (LCO).

Secondary products:

- Fuel gas;
- Clarified oil (CLO) (or decanted oil (DCO));
- Coke.

Date of receipt: 24/9/2025
Date of review and editing: 24/9 - 6/11/2025
Date of approval: 6/11/2025

The reactor effluent from the disengager in the reaction section is sent to the main fractionator T-1501. The bottom slurry pumparound is circulated by pumps P-1519A/B/C, the residual heat from this recycle stream is utilized to heat the feedstock stream and generate medium- and high-pressure steam. Most of this cooled slurry pumparound is returned to the grid section (Bed #5), where the reactor effluent is desuperheated and the bottom slurry product is condensed. Part of the cooled slurry is returned to the bottom of the column to quench the temperature and minimize coking.

The slurry product stream is drawn and sent to drum D-1515. The slurry product is then pumped and cooled in the low-pressure steam generator before being routed to separator X-1504 to remove fine catalyst particles. Decanted oil (DCO) exiting the separator is again cooled before being transferred to the storage tank.

Since the RFCC unit was commissioned in April 2009, the flash point temperature of DCO has failed to reach the design value of 100°C. In numerous instances, it even fell below the standard value of 49°C in storage tanks. Specifically, at the end of June 2018, this value dropped

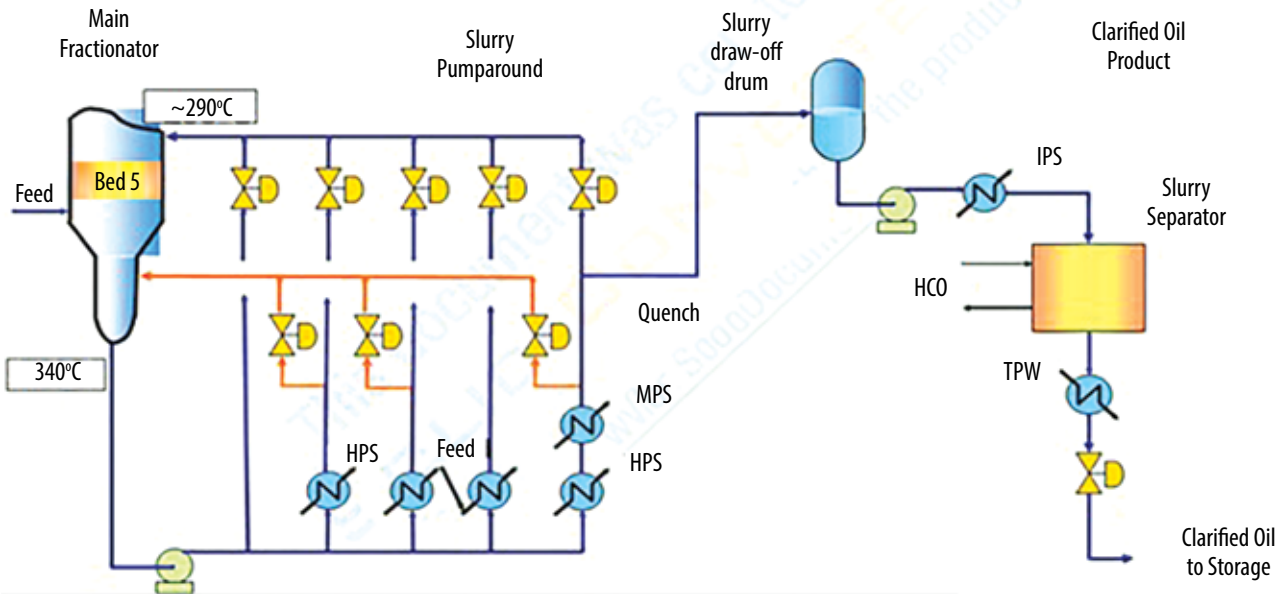

Figure 1. *The main fractionator bottom T-1501.*

below 46°C. To ensure the safe storage of DCO in product tanks (P3) and to meet the commercial standards, high-flash point residue has to be blended to increase the flash point of the FO product. Nevertheless, blending high-value residue into DCO to produce FO and selling it at a lower price reduces the economic efficiency of the refinery. Various solutions were evaluated, including technological parameter adjustments, replacement of the #5 packing layer, and change of the packing arrangement angle as recommended by the vendor in 2014, to enhance light fraction separation efficiency. However, the flash point did not improve. Most recently, the technology licensor was requested to design and install a steam ring at the bottom of the tower, but the licensor's assessment indicated that the effectiveness was uncertain and did not recommend its use.

In response to this urgent issue, the authors have researched, evaluated, and proposed a solution to increase the flash point temperature of fuel oil (FO) products. This is to ensure operational safety, meet FO sale standards, and reduce the cost of blending high-value products, while utilizing existing equipment and minimizing major changes to the equipment.

2. Theoretical framework/methods

2.1. Mechanism of separating light fractions from the liquid in the current configuration

The stripping process is a physical separation method in which one or more components are removed from the liquid stream by a vapor stream. In industrial applications, the liquid and vapor streams can flow concurrently or counter-currently, and the stripping process is typically carried out in packed or tray tower structures. Inert gases, steam, and hydrocarbon gases are commonly used as the stripping media to remove unwanted light components from the liquid stream based on reducing partial pressure as light gases absorb heat from the liquid and evaporate from the liquid stream.

In practice, D-1515 drum, containing liquid which is the DCO product, is an empty vessel without any internal structure. Therefore, converting this D-1515 into a light-fraction separation tower equipped with a tray or packed structure is extremely complex. The downstream equipment of vessel D-1515 is the X-1504 separator, which operates at approximately 35 kV to remove solid catalyst particles from the DCO stream, ensuring compliance with the ash content specification of 100 ppm wt maximum. Therefore, steam cannot be used as the stripping medium. Additionally, pump P-1504 transfers liquid from D-1515 at an operating temperature of nearly 200°C. If steam were used, any condensation during the stripping process may cause cavitation in the pump.

Due to these constraints, the authors applied nitrogen gas directly into the liquid in D-1515 vessel to separate the absorbed light fractions from the DCO product. This solution ensures the use of existing equipment and safe operation while being effective.

Table 1. *N_2 product quality using injection at D-1515*

	Analyst	Result	Units
1	Nitrogen	100	mol%
2	Trace oxygen	3.5	ppm vol
3	Carbon dioxide	< 0.2	ppm vol
4	Carbon monoxide	0.2	ppm vol

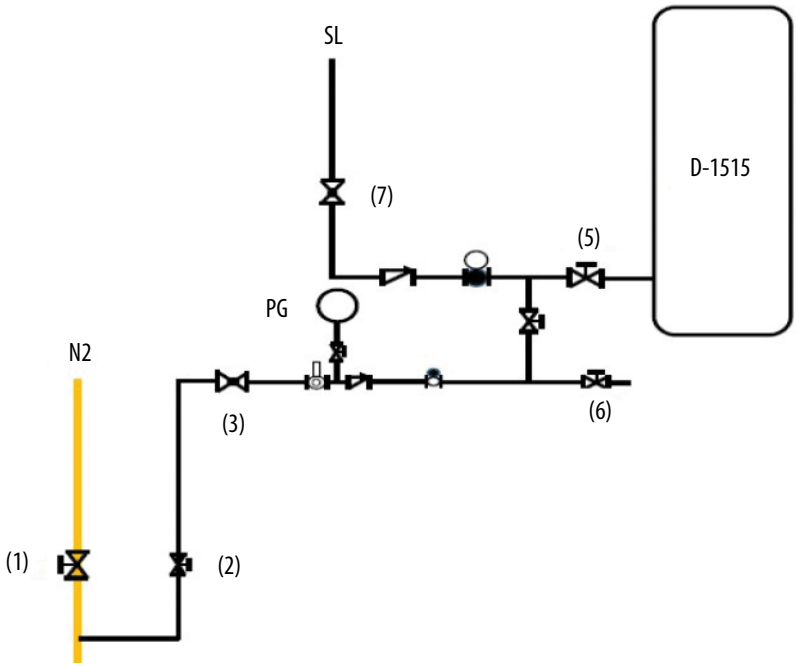

Figure 2. *Sketch of the nitrogen injection point into the D-1515 liquid drum.*

2.2. Site survey and evaluation of existing equipment system, proposal of the nitrogen injection point, and implementation of the modification

The authors surveyed the existing equipment at BSR to propose a nitrogen injection point that aligns with the goal of utilizing the existing equipment configuration at the lowest cost. After the proposal was approved by the company leadership, the authors issued "028-APR-R&D on Approval for N_2 injection service with flexible", allowing the installation of flexible hoses to connect and inject nitrogen into the liquid phase in vessel D-1515. This resulted in the flash point temperature of DCO soaring to 84°C, surpassing the product sales standard of 66°C for the first time since the refinery began operation. Based on the high effectiveness of this temporary system in improving the flash point of DCO, the team implemented MOC-15-18-318. After evaluating the equipment condition during the fourth overall maintenance of the Dung Quat refinery in 2020, the system was integrated into the permanent configuration.

3. Results and discussion

3.1. Practical application of the solution

The trial process initially started injecting nitrogen at a point above the liquid surface in vessel D-1515, at a flow rate of approximately 200 m^3/hour. However, this approach did not result in any improvement in the flash point of the DCO product. Only when nitrogen was directly injected into the liquid phase of vessel D-1515 did the flash point temperature significantly increase. During the initial phase of the trial, the nitrogen flow rate was set at 200 m^3/hour, but subsequent optimization and flash point sampling indicated that a much lower flow rate of approximately 70 m^3/hour was sufficient to raise the flash point temperature to meet the DCO product specification.

Since the nitrogen injection system has been operational, it has significantly improved the flash point of DCO, which had previously been unattainable. Additionally, with this system, the flash point temperature can be adjusted as required. Thanks to the installed system, the refinery no longer needs to blend valuable components like residue into DCO to increase the flash point temperature to meet the commercial product sales standard for FO.

The successful handling of the DCO flash point has increased the competitiveness of BSR FO product in the market, while also opening new directions for the production and sale of marine fuel oil (MFO) at higher values.

The operating conditions of vessel D-1515 remain unchanged in the temperature range of 190 - 194°C and with operating pressure maintained at 1.2 - 1.3 kg/cm^2. When nitrogen is injected into the vessel, the pressure will increase. Since the drum pressure is automatically adjusted by the pressure controller, the valve on the flare line opens wider to maintain stable pressure at the set value of 1.2 - 1.3 kg/cm^2.

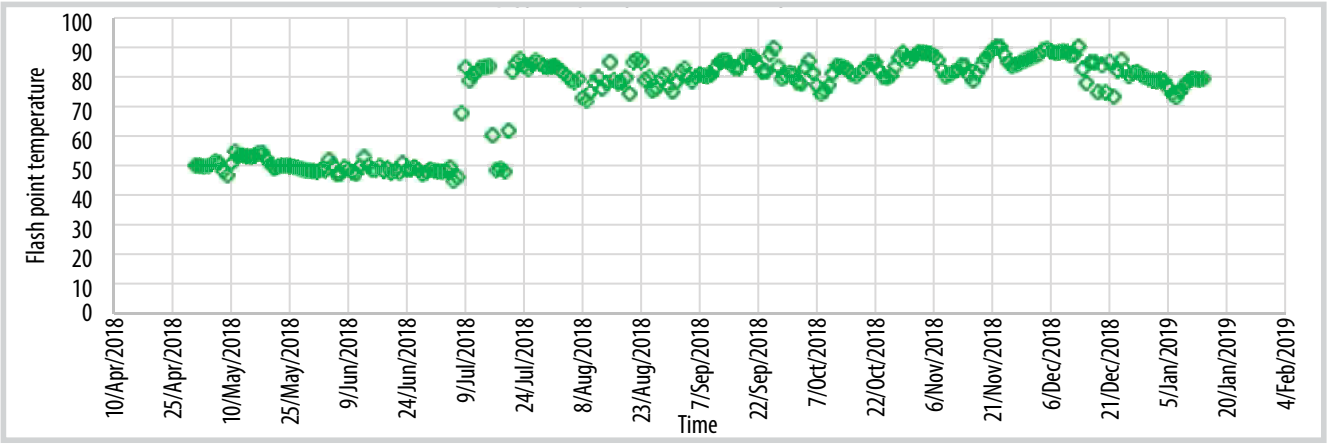

Figure 3. *The flash point temperature of DCO has improved since July 2018.*

Table 2. *Analysis results of the gas sample after performing N_2 stripping*

Sample name	Date/time of sample	Component	Method	Unit	Result	Note
Gas from D-1515 to fare	15H00 - 01/09/2021	Hydrogen	UOP539-12	%mol	19.46	
		C_6+		%mol	0.69	
		Methane		%mol	2.6	
		Ethane		%mol	1.44	
		Ethylene		%mol	1.32	
		Carbon dioxide		%mol	0.06	
		Propane		%mol	0.7	
		Cyclopropane		%mol	0.0	
		Propylene		%mol	1.59	
		n-Butane		%mol	0.85	
		i-Butane		%mol	0.26	
		Propylene		%mol	0	
		Acetylene		%mol	0	
		Hydrogen Sulfide		%mol	0.42	
		t-2-Butene		%mol	0.3	
		1-Butene		%mol	0	
		i-Butene		%mol	0.43	
		c-2-Butene		%mol	0.32	
		Cyclopropene		%mol	0.01	
		i-Pentane		%mol	0.54	
		n-Pentane		%mol	0.08	
		1,2 Butadiene		%mol	0	
		1,3 Butadiene		%mol	0	
		Methyl Acetylene		%mol	0	
		3-methyl-1-butene		%mol	0.06	
		t-2-Pentene		%mol	0.2	
		2-methyl-2-butene		%mol	0.36	
		1-Pentene		%mol	0.08	
		2-methyl-1-butene		%mol	0.14	
		c-2-Pentene		%mol	0.09	
		Ethyl Acetylene		%mol	0.02	
		Oxygen		%mol	2.84	
		Nitrogen		%mol	65.08	
		Carbon monoxide		%mol	0.06	

Table 3. *Comparison of benefits: N_2 stripping vs. residue blending to achieve required flash point temperature*

	Average price index*
BH crude oil price, USD/bbl **(C44)**	62
BH crude oil price, USD/ton **(C45)**	= C44 × 6.28981/0.825 = 62 × 6.28981/0.825 = 472.6**
FO price, USD/ton **(C46)**	369.67
FO export VAT, % **(C47)**	8.2%
FO price (including non-refundable VAT due to export), USD/ton (C48)	= C46 × (1 - C47) = 369.67 × (1 - 8.2%) = 339.36
DO price, USD/bbl **(C49)**	67.44
DO price, USD/ton **(C50)**	= C49 × 6.28981/0.83 = 67.44 × 6.28981/0.83 = 511.1

** From August 1, 2018 to August 10, 2020; ** 1 m^3 = 6.28981 bbl*

The analysis results of the venting gas stream at the top of D-1515 to the flare after nitrogen injection to separate the light fractions from the liquid are shown in Table 2.

Thus, the issue causing the low flash point of DCO oil is largely due to the amount of hydrogen gas, with a smaller contribution from C1, C4 and C5 gases being absorbed in the liquid. These gases are routed to the flare system for combustion. Any heavier fractions carried over with the gas stream will be stripped and collected in the flare system's knock-out drum, provided such equipment is installed. The process of separating light gases does not affect the liquid yield of DCO oil because these components are not permitted in the DCO product specification and must be removed from the product stream.

3.2. Economic and technical efficiency

By avoiding the installation of a steam ring at the bottom of tower T-1501, approximately USD 300,000 in installation costs and USD 177,390 in annual operating costs are saved.

Operating costs: Steam price: USD 27/ton (refinery steam price); Steam amount: 750 kg/hour (0.75 tonnes/hour); Total steam rate: 18 tonnes/day; Daily cost: 486 USD/day; Yearly cost: 177,390 USD/year; Material, fabrication & installation costs: USD 300,000 (estimated cost of installing a steam ring).

With the DCO flash point above 84°C and without continuous blending of residue to increase the DCO flash point from 1/8/2018 to 10/8/2020, the benefit is approximately USD 11,134,562.

DCO flow rate and flash point:

- DCO flowrate: 28 m^3/hour (26.7 tonnes/hour);
- DCO flash point: 50.7°C;
- DCO rundown temperature: 77.7°C;
- DCO flash spec min: 47°C;
- Atmospheric residue density: 0.884 g/cm^3.

Blending AR to DCO:

- AR blend ratio to increase 1°C FP: 4%;
- AR blend to reduce FP: 4.11 m^3/hour (3.632 tonnes/hour).
- AR, USD/ton = DO, USD/ton (C53) = C50 = 511.1
- Delta AR vs FO, USD/ton (C54) = (C53 - C48) = 511.1 - 339.36 = 171.7
- AR blend cost, USD/hour (D16) = D14 × C54 = 3.632 × 171.7 = 623.6.

Operating Cost:

- N_2 stripping, Nm^3/h (D29): 20 m^3/h
- N_2 stripping price, USD/Nm^3 (D30): 0.021
- N_2 stripping cost, USD/h (D31): = D30 × D29 = 0.021 × 20 = 0.42
- Reducing heating up for storage tank at P3 (D32): = -(20 × 37.5) / (10 × 24 + 20) = -2.9
- Total operating cost, USD/h (D35): = D32 + D31 = -2.9 + 0.42 = -2.5

Table 4. *Overall efficiency compared to AR mixture*

Annual price index	Average price index*
Overall efficiency compared to AR mixture, USD/hour (D38)	= D16 - D35 = 623.6 + 2.5 = 626.1
Overall efficiency compared to AR mixture, USD (D39)	= D38 × D40 × 24 = 626.1 × 741 × 24 **= 11,134,562**
Number of days solution applied (D40)	= 741 days (from August 1, 2018, to August 10, 2020)

** From August 1, 2018 to August 10, 2020*

Implementation Funding:

The solution does not require retrofitting and incurs no costs.

Benefits:

- Cost savings from not retrofitting and not blending residue into DCO amount to approximately USD 300,000 + USD 177,390 + USD 11,134,562 = USD 11,611,952.

- It facilitates the plant's ability to produce MFO products from 2020. The estimated production of MFO from 2020 increases the plant's efficiency by approximately USD 19.5 million per year compared to the production of FO 180 cSt.

- The long-standing issue of DCO's flash point temperature is resolved, ensuring stable operation of the T-1501 distillation tower in the RFCC unit.

- DCO flash point temperature can be adjusted by regulating the nitrogen stream in the D-1515.

- DCO flash point is enhanced to meet TCVN/MFO product standards.

4. Conclusion

BSR has implemented a nitrogen injection system to ensure that the flash point of commercial FO consistently exceeds the standard value. This method has proven effective, eliminating the need for blending with high-flash point residues.

Major refineries worldwide, including those operated by Shell, SK, and O&M, as well as facilities licensed by Axens, have encountered persistent challenges with low low or unstable flash points in their DCO. These refineries have invested substantial capital in system retrofits, however, such modifications have generally failed to yield satisfactory results.

In contrast, BSR has successfully addressed this issue through the innovative application of engineering principles, achieving DCO flash point improvements that meet the specifications for commercial FO.

The nitrogen injection system developed by BSR represents a significant technological advancement in flash point control for commercial FO production. This approach not only ensures compliance with safety standards but also offers considerable advantages in terms of cost reduction and operational efficiency compared to conventional blending methods.

References

[1] Norman P. Lieberman, and Elizabeth T. Lieberman, *A working guide to process equipment*. McGraw-Hill, 2014.

[2] Reza Sadeghbeigi, *Fluid catalytic cracking handbook*. Butterworth-Heinemann, 2019.

PETROVIETNAM
SCIENCE, TECHNOLOGY & INNOVATION

CONVERSION OF SUSTAINABLE AGRICULTURAL RESIDUES INTO MCC FOR PLA-BASED BIODEGRADABLE PLASTIC APPLICATIONS

Vu Thi Thu Ha, Nguyen Thi Bay, Nguyen Thanh Trung , Pham Nam Phong, Pham Van Bac, Nguyen Thi Thu Trang
National Key Laboratory for Petrochemical and Refinery Technologies
Email: ptntd2004@yahoo.fr
https://doi.org/10.47800/PVSI.2025.06-07

Summary

Microcrystalline cellulose (MCC) was extracted from cassava stems, banana pseudostems, pineapple leaves, and spent coffee grounds through an optimized acid hydrolysis process. Comprehensive structural, morphological, and thermal characterization revealed distinct differences among sources, with cassava stem-derived MCC identified as the most feasible and sustainable option due to its high crystallinity, uniform particle size, processing stability, ready availability, and large-scale supplypotential. This MCC was incorporated into thermoplastic starch (TPS) and polylactic acid (PLA) matrices to fabricate fully biodegradable composites. X-ray diffraction (XRD) confirmed the preservation of MCC crystalline structure, scanning electron microscopy (SEM) revealed homogeneous dispersion within the TPS phase, and thermogravimetric/differential thermal analyses (TGA/DTA) demonstrated improved thermal stability. Mechanical testing showed that the optimized PLA:MCC:TPS ratio of 70:4.5:25.5 (with 15% MCC relative to (MCC/TPS)) provided the best balance between tensile strength, modulus, and biodegradability.These composites exhibited mechanical strength for sustainable packaging and food service applications while maintaining full compostability. Overall, the results highlight cassava stems as a sustainable, locally available MCC source and confirm that PLA/(MCC/TPS) composites can replace petrochemical-based plastics in targeted sectors, contributing to global energy transition strategies and CO_2 emission reduction targets.

Key words: Agricultural residues, biomass-derived chemicals, biodegradable composites, cassava stems, energy transition, microcrystalline cellulose, polylactic acid.

1. Introduction

Agricultural residues such as cassava stems, banana pseudostems, pineapple leaves, and spent coffee grounds are abundant biomass resources that remain largely underutilized. These lignocellulosic wastes are rich in cellulose, a renewable biopolymer that can be transformed into microcrystalline cellulose (MCC) through relatively simple extraction processes. MCC is widely recognized for its high crystallinity, excellent reinforcing potential, and biodegradability, making it suitable for integration into biobased polymer composites [1 - 5]. Experimental studies have shown that incorporating microcrystalline cellulose (MCC) into PLA can significantly improve mechanical properties and thermal stability of PLA/MCC composites [6, 7]. These improvements demonstrate the potential of MCC as a sustainable reinforcement in PLA matrices, supporting development of renewable and eco-friendly bioplastics. Such composites align with global goals toward low-carbon, circular economies and enhanced performance of biodegradable materials in packaging and other applications.

In this study, MCC was extracted from four agricultural residues: cassava stems, banana pseudostems, pineapple leaves, and spent coffee grounds. A systematic comparison of their structural, morphological, and thermal properties identified cassava stem-derived MCC as the most feasible source, considering its high crystallinity, uniform particle morphology, thermal stability, abundant availability, and large-scale supply potential. This MCC was then incorporated into PLA/TPS blends to produce fully biodegradable biocomposites.

Given the global imperative to transition toward renewable, biomass-derived materials for both energy transition and CO_2 emission reduction, developing high-

Date of receipt: 19/8/2025
Date of review and editing: 19/8 - 15/10/2025
Date of approval: 15/10/2025

performance PLA/(MCC/TPS) composites from agricultural residues offers significant environmental and industrial advantages. This work aims to (i) valorize agricultural waste into value-added MCC; (ii) enhance the mechanical and thermal performance of PLA/TPS composites; and (iii) propose a sustainable pathway to replace petrochemical plastics in packaging and food service applications.

2. Materials and methods

2.1. Raw materials

Cassava stems, banana pseudostems, pineapple leaves, and spent coffee grounds were used for the extraction of microcrystalline cellulose (Figure 1). Cassava stems, banana pseudostems, and pineapple leaves were collected from local sources in Phu Tho and Thanh Hoa provinces, whereas spent coffee grounds were provided by Trung Nguyen Instant Coffee Joint Stock Company (Vietnam). After washing, cassava stems, banana pseudostems, and pineapple leaves were cut into 1 - 2 cm pieces; spent coffee grounds were used directly without further pretreatment. Thermoplastic starch was prepared in-house from avocado seeds (an agricultural waste source) by plasticization with glycerol and water, and was used without additional purification. Commercial PLA, glycerol (≥ 99%), and maleic anhydride (MA, ≥ 98%) were used as received.

2.2. MCC preparation

The extraction and isolation of MCC from the raw materials were carried out using the method described in [8], with process conditions modified for this study. Washed biomass was dried at 70 - 80°C, for 24 hours, milled, and sequentially treated with 0.1 N acetic acid and 15% NaOH (solid-to-liquid ratio of 1:20 g/ml, 105°C, 2 hours each), with washing to neutral pH. Bleaching with 3% H_2O_2 (1:10, 70°C, 4 hours) was followed by hydrolysis with 1.5 M HNO_3 (1:25, 70°C, 3 hours). MCC was washed to pH = 7, dried at 50°C for 24 hours, then milled, and stored.

2.3. MCC/TPS blends

The experimental preparation of thermoplastic starch and the MCC/TPS compound was conducted following the procedure described in [9]. Based on the components and mixing ratios reported in [9], the formulation and processing conditions were modified and optimized to obtain MCC/TPS composites suitable for the materials investigated and to achieve optimal performance. TPS was obtained by heating starch, glycerol, and water (30:40:30 wt%) at 120 - 130°C for 15 minutes with stirring. MCC (5 - 20 wt%) was incorporated, mixed at 80°C for 10 minutes, dried at 60°C for 6 hours), and cut for PLA blending.

2.4. PLA/(MCC/TPS) composites

PLA-MA was prepared by reactive melt-grafting of maleic anhydride (MAH, 3 wt% relative to PLA) in the presence of dicumyl peroxide (DCP, 0.2 wt%) at 190°C for 3 minutes in an internal mixer, following the procedure reported for PLA/MCC composites [10]. PLA-MA and MCC/TPS were dried at 60°C for 6 hours, weighed to the desired compositions (20 - 40 wt% MCC/TPS), and dry-mixed. Blending was carried out at 160 - 180°C for 10 - 15 minutes under stirring. The molten mixture was cast into non-stick aluminum molds, lightly pressed, cooled, demolded, cut, and dried at 50°C to remove residual moisture.

2.5. Characterization

FTIR spectra were recorded on a Nicolet 6700 (Thermo Electron) using KBr pellets (4000 - 400 cm^{-1}). XRD was performed on a D8 Advance (Bruker AXS) with Cu Kα radiation (λ = 1.5406 Å, 40 kV, 30 mA), 2θ = 5 - 40°, step size 0.02°, and the crystallinity index (CrI) was calculated using the Segal method. TG-DTA was conducted on a Diamond TG-DTA (Perkin Elmer) under nitrogen (RT-600°C, 10°C/min). SEM images were obtained using a Hitachi S-4800 at 10 - 15 kV after sputter-coating with gold.

2.6. Evaluation of performance and material properties

The actual yield of MCC relative to the raw material was calculated according to Equation (1).

$$Actual\ yield\ (\%) = \frac{M_2}{M_1} \times 100 \quad (1)$$

Where:

M_1 is the initial dry mass of raw material (g),

M_2 is the mass of MCC obtained (g).

The collection efficiency of MCC relative to the theoretical yield was determined using Equation (2).

$$Collection\ efficiency\ (\%) = \frac{M_2}{M_o} \times 100 \quad (2)$$

Where:

M_o is the theoretical mass of MCC in the raw material (g),

M_2 is the obtained mass of MCC (g).

The crystallinity of MCC was determined using the crystallinity index (CrI), calculated according to Equation (3).

$$CrI\ (\%) = \frac{(I_{200} - I_{am})}{I_{200}} \times 100 \quad (3)$$

Where:

CrI is the relative degree of crystallinity (%),

I_{200} is the maximum intensity of the (200) crystalline plane,

I_{am} is the intensity of the amorphous region.

2.7. Mechanical properties

Tensile strength and elongation at break were determined following TCVN or ASTM D638. Elastic modulus was measured using a universal testing machine under tensile-compressive loading. Standard dog-bone specimens were used.

3. Results and discussion

3.1. Recovery yield and structural characterization of MCC

The analytical results evaluating the composition and properties of the four biomass sources - pineapple leaves, banana pseudostems, cassava stems, and spent coffee grounds - are summarized in Table 1. The MCC recovery efficiency obtained from these biomass sources is presented in Table 2.

The results showed that the actual MCC yields obtained from pineapple leaves, banana pseudostems, cassava stems, and spent coffee grounds were 22.7%, 18.5%, 22.2%, and 10.4%, respectively. Corresponding collection efficiencies relative to the theoretical values ranged from 95.5% to 98.3%. Among the studied biomass sources, pineapple leaves and cassava stems exhibited the highest MCC yields (over 22%), followed by banana pseudostems (18.5%), whereas spent coffee grounds produced the lowest yield (10.4%). These differences can be attributed to the variations in the initial cellulose content and the extent of lignin and hemicellulose removal achieved during the chemical treatment process.

SEM micrographs further support these findings (Figure 3). Raw biomass samples such as pineapple leaf fibers and banana pseudostems (Figures 3a and 3c) display

Figure 1. *Raw material sources for MCC production: cassava stem, banana pseudostems, pineapple leaf, spent coffee grounds.*

Table 1. *Composition and properties of raw biomass materials (dry weight basis)*

Raw material sample	Cellulose (%)	Hemicellulose (incl. extractives) (%)	Lignin (%)	Ash (%)	Moisture content (%)
Pineapple leaves	23.7	56.0	16.4	3.9	5.7
Banana pseudostems	20	67.4	10	2.6	8
Cassava stems	23	45.9	26		7
Spent coffee grounds	11	56.3	27	5.7	8

Table 2. *MCC recovery yield from different biomass sources*

Raw material	Dry mass of raw material (g)	Mass of MCC obtained (g)	Actual MCC yield (%)	MCC collection efficiency compared to theory (%)
Pineapple leaves	102	23.2	22.7	97.8
Banana pseudostems	104	19.2	18.5	96.1
Cassava stems	102	22.6	22.2	98.3
Spent coffee grounds	101	10.5	10.4	95.5

compact, heterogeneous surfaces with visible impurities, indicative of lignin and hemicellulose coverage. After the isolation process, the corresponding MCC samples (Figures 3b and 3d) exhibit cleaner and smoother surfaces, and a more fibrillated morphology, confirming the removal of non-cellulosic components and exposure of cellulose microfibrils. Pineapple leaf-derived MCC retains a layered fracture pattern, while banana pseudostem-derived MCC shows greater fibril separation, suggesting variations in fiber structure and treatment efficiency.

The SEM image of cassava stem raw material (Figure 3e) reveals a heterogeneous surface morphology, characterized by irregularly arranged small fragments. This structure is indicative of the presence of non-cellulosic components such as hemicellulose, lignin, and pectin, which encapsulate the cellulose fibers. In contrast, the SEM image of MCC derived from cassava stems (Figure 3g) exhibits a well-organized, highly-ordered fibrous structure, characteristic of purified cellulose. This morphological transition provides clear evidence of the high crystallinity achieved in the cassava stem-derived MCC sample.

In the SEM image of the raw spent coffee grounds (Figure 3h), the surface appears rough and heterogeneous, with no visible typical lignocellulosic fiber structures, thus evidencing surface impurities and non-cellulosic residues.

In contrast, the SEM image of the microcrystalline cellulose obtained from spent coffee grounds (Figure 3k)

Figure 2. *MCC extraction steps from various raw materials: from top to bottom - pineapple leaves, banana pseudostems, cassava stems, spent coffee grounds; from left to right - raw material powder, after lignin removal, after bleaching, and final MCC product.*

reveals a much smoother surface morphology with less densely packed microfibrils. These fibrils appear to be well-isolated from each other, indicating the breakdown into discrete cellulose microcrystals after chemical treatment. This morphological change confirms effective removal of hemicellulose, lignin, and surface impurities, while preserving a smooth, ordered cellulose structure.

According to the literature, acid hydrolysis attacks the amorphous regions of cellulose, breaking down the polymer into isolated microcrystals. The penetration of acid ions into fiber interiors promotes depolymerization, particularly in the amorphous regions, while the crystalline domains remain intact.

The average diameter of chemically treated cellulose microcrystals has been reported to be approximately 2 - 3 µm [11]. However, precise length measurements remain challenging due to irregular fragment shapes and overlapping fibrils observed in SEM images.

Notably, the microcrystals extracted from spent coffee grounds are smaller in diameter compared to those reported from other biomass sources. For instance, MCC derived from durian rind shows particle sizes ranging from 6.2 to ~25.4 µm [12], while MCC from date seeds can reach up to 65.3 µm in peak size [13]. The significantly smaller size extracted from spent coffee grounds suggests a more effective hydrolytic breakdown, likely due to a less rigid cell wall structure and efficient chemical processing.

Overall, the morphological changes observed in the SEM images confirm the successful breakdown of the complex lignocellulosic structure and the enrichment of the cellulose phase, which is essential for obtaining MCC suitable for polymer composites or biodegradable plastic applications.

The FTIR spectra of MCC from all four sources (Figure 4) show characteristic cellulose bands, including broad O–H stretching (~3,270 – 3,333 cm^{-1}), C–H stretching (~2,900 cm^{-1}), C–O–C and C–O stretching (1,150 - 1,030 cm^{-1}), and crystalline cellulose peaks at ~1,420 and 895 cm^{-1}. The raw materials display additional signals from non-cellulosic components, such as hemicellulose, lignin, and pectin, which are significantly diminished or absent in the MCC samples, confirming effective purification. Notably, the O–H stretching band in spent coffee ground MCC appears at a lower wavenumber (~3,112 cm^{-1}) compared to ~3,270 – 3,333 cm^{-1} in other MCCs, indicating stronger hydrogen bonding within the cellulose network. This red shift is likely due to the smaller crystallite size and denser packing of cellulose fibrils after treatment, promoting more extensive intermolecular hydrogen bonding.

Figure 5 presents the thermogravimetric (TG) and differential thermal analysis (DTA) curves of MCC derived from pineapple leaves, banana pseudostems, cassava stems, and spent coffee grounds. The thermal degradation profiles of all samples exhibit three distinct mass-loss stages, consistent with previous reports on MCC extracted from lignocellulosic biomass [14, 15].

The first stage, occurring between 30 and 200°C, corresponds to the removal of adsorbed moisture and loosely bound volatiles, with mass losses of 2.37%, 3.88%,

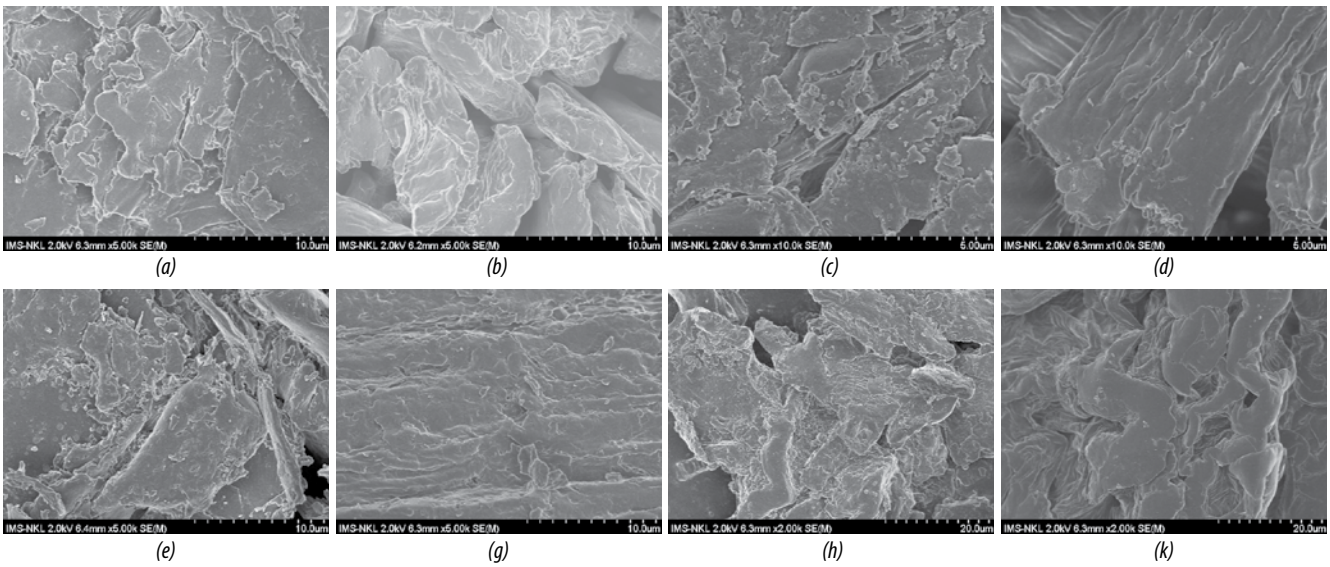

Figure 3. *SEM images of raw materials - pineapple leaves (a), banana pseudostems (c), cassava stems (e), spent coffee grounds (h) - and their corresponding MCC products: pineapple leaves (b), banana pseudostems (d), cassava stems (g), and spent coffee grounds (k).*

4.92%, and 9.77% for MCC from pineapple leaves, banana pseudostemss, cassava stems, and spent coffee grounds, respectively. These variations reflect differences in hydrophilicity and moisture content among the biomass sources.

The second stage, observed between 200 and 400°C, represents the major decomposition region of cellulose, primarily due to the cleavage of β-1,4-glycosidic linkages in the glucose polymer chain. The corresponding mass losses were 76.54%, 72.20%, 64.47%, and 58.04% for MCC from pineapple leaves, banana pseudostems, cassava stems, and spent coffee grounds, respectively. Sharp DTG peaks appeared at 332.39°C, 336.04°C, 330.65°C, and 316.68°C for these samples, indicating the main pyrolysis temperatures of cellulose. The absence of peaks in the regions of 200 - 280°C (typical of hemicellulose) and 380 - 450°C (typical of lignin) confirms that most hemicellulose and lignin impurities were effectively removed.

The third stage, occurring between 400 and 600°C, involves the secondary decomposition of residual carbonaceous matter and thermally stable lignin fractions, reflecting the remaining non-cellulosic content. The residual mass beyond 600°C was very low (only a few percent), indicating a low ash and inorganic content.

The TGA/DTG profiles indicate that the main decomposition temperatures of MCC isolated from the four biomass sources ranged from 316 to 336°C, with very low residual ash contents. These values are comparable to those reported for MCC derived from other lignocellulosic materials in the literature [16, 17].

Collectively, the TG-DTA results confirm that the applied preparation processes effectively removed non-cellulosic organic matter and inorganic components, producing MCC with high thermal stability and purity across all four biomass sources.

The XRD patterns of the raw materials and the MCC

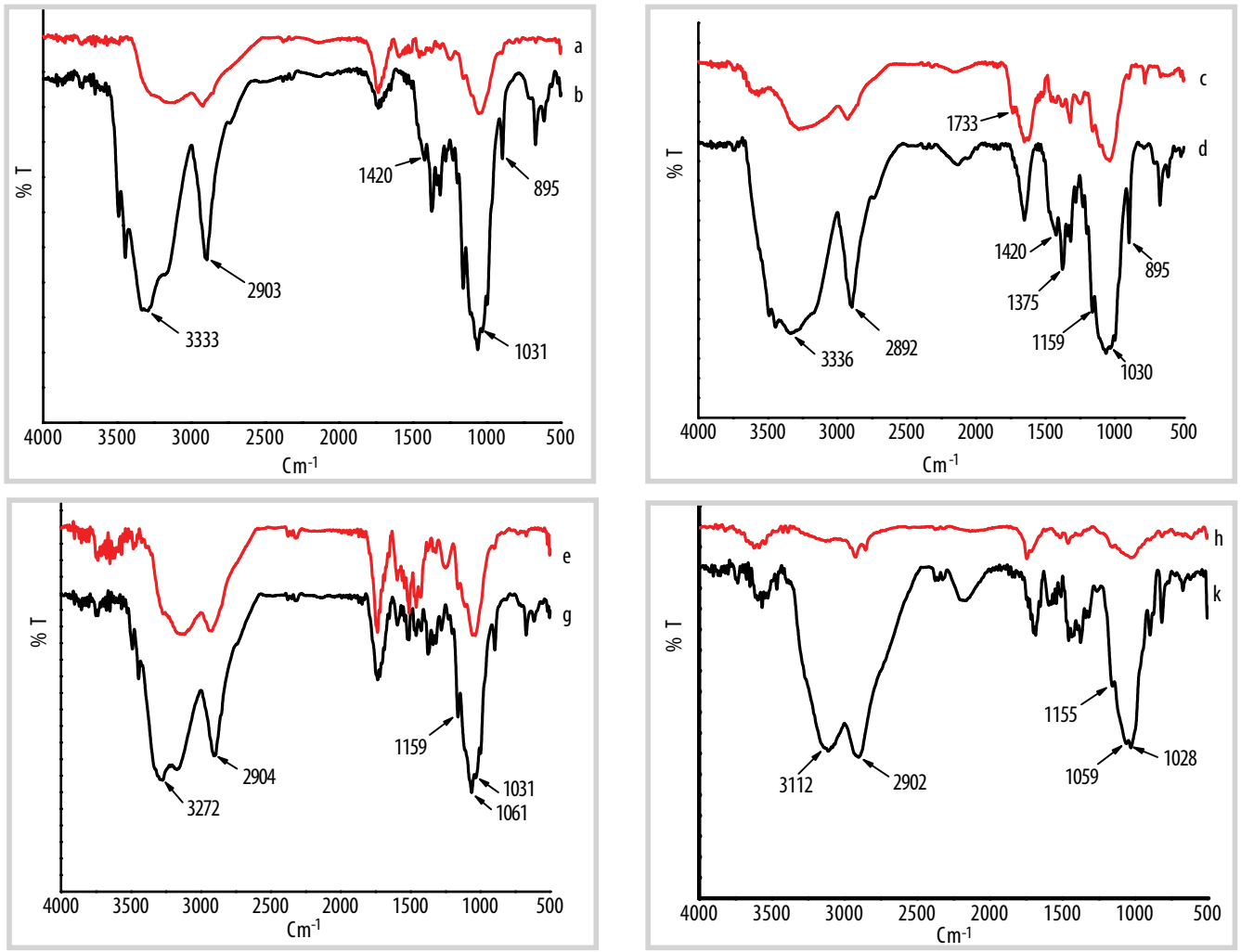

Figure 4. *FTIR spectra of raw materials - pineapple leaves (a), banana pseudostems (c), cassava stem (e), and spent coffee grounds (h) - and their corresponding MCC samples.*

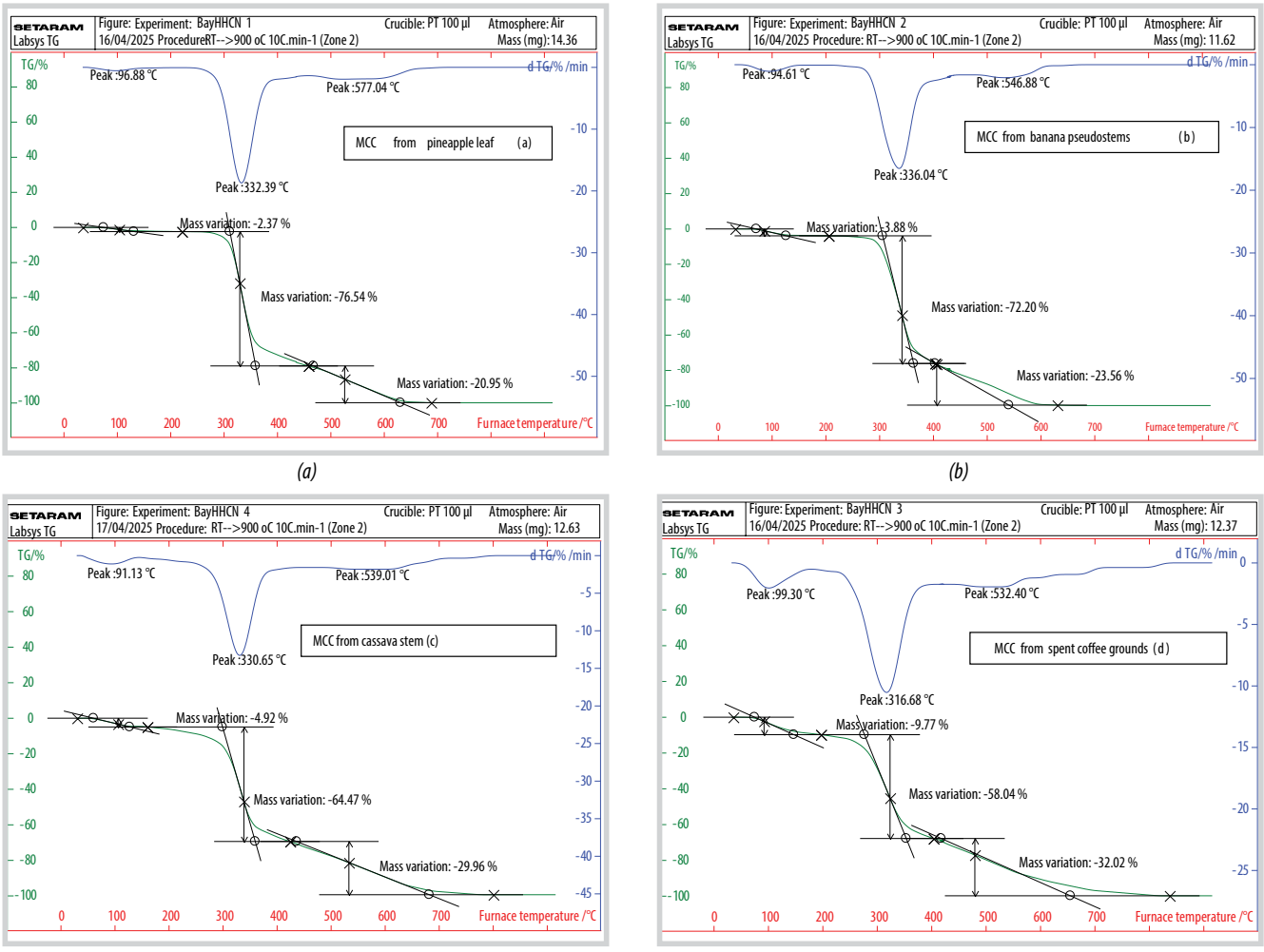

Figure 5. *Thermogravimetric (TG) and differential thermal analysis (DTA) curves of MCCs derived from four biomass sources: (a) pineapple leaves, (b) banana pseudostems, (c) cassava stem, and (d) spent coffee grounds.*

Table 3. *Crystallinity index (CrI) and crystal size of raw biomass samples and corresponding MCC*

No.	Sample name	Crystalline index (CrI, %)	Crystal size (nm)
1	Raw pineapple leaves	37.5	2.19
	MCC from pineapple leaves	73.1	4.58
2	Raw banana pseudostems	48.1	2.09
	MCC from banana pseudostems	63.4	4.61
3	Raw cassava stems	56.7	2.31
	MCC from cassava stems	74.8	4.18
4	Raw spent coffee grounds	29.4	2.82
	MCC from spent coffee grounds	69.2	4.34

obtained from four biomass sources - (a) pineapple leaves, (b) banana pseudostems, (c) cassava stems, and (d) spent coffee grounds - are shown in Figure 6. The corresponding crystallinity index (CrI) and crystal size values of the samples are summarized in Table 3.

The amorphous (I_{am}) and crystalline (I_{002}) diffraction peaks were observed in the 2θ ranges of 16.01° - 16.8° and 22.1° - 22.8°, respectively (Figure 6). As shown in the results table, all samples exhibited increased crystallinity index and crystal size after the preparation process. The variations in peak height and width among the samples reflected differences in crystallinity degree and crystal size [18]. The higher CrI value of the MCC samples compared to their corresponding raw materials can be attributed to

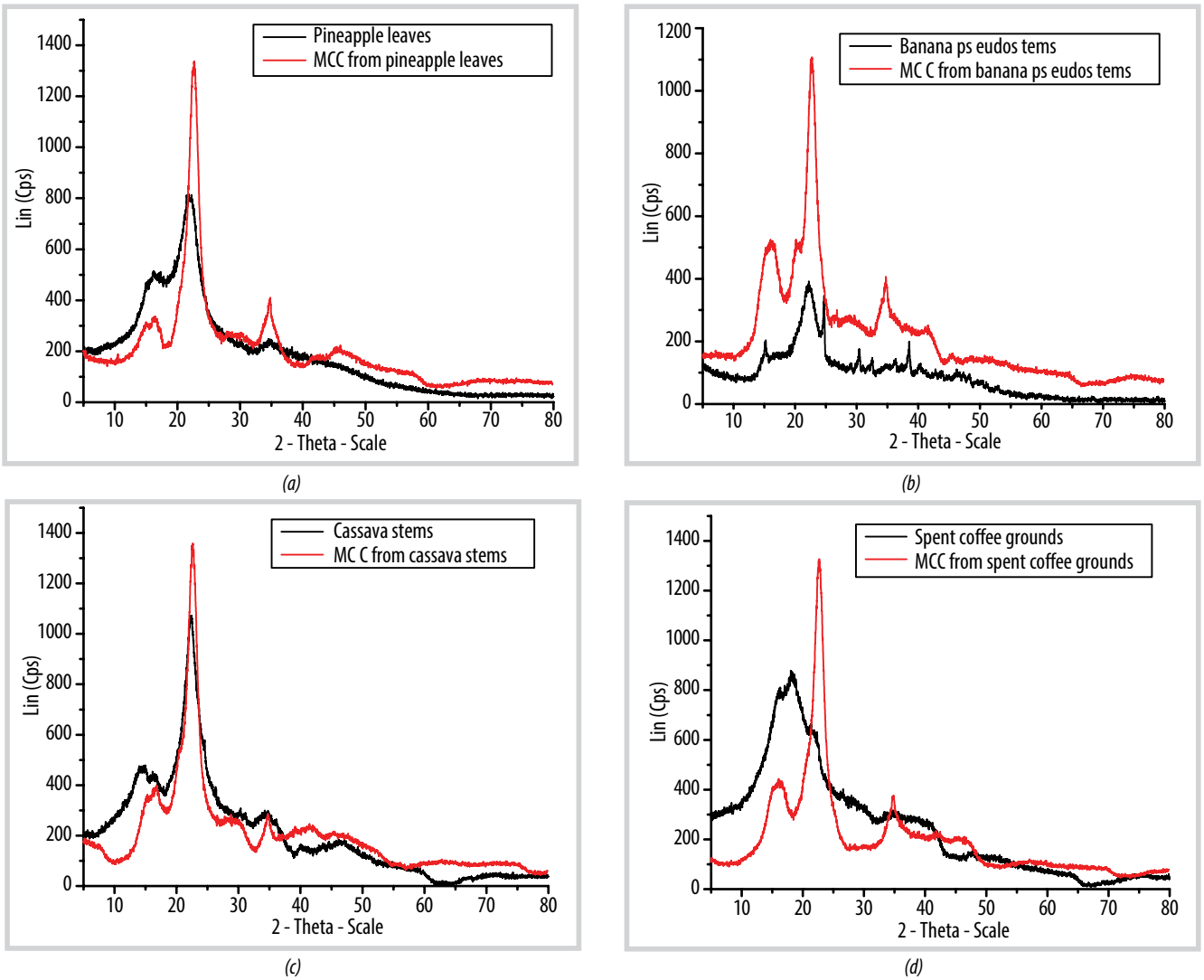

Figure 6. *XRD patterns of raw materials and the corresponding MCC obtained from four biomass sources: pineapple leaves (a), banana pseudostems (b), cassava stems (c), and spent coffee grounds (d).*

the removal of amorphous cellulose regions during acid hydrolysis, which cleaves the 1,4-glycosidic bonds.

Overall, the MCC extracted from cassava stems, banana pseudostems, pineapple leaves, and spent coffee grounds demonstrated distinct differences in yield, particle morphology, crystallinity, and thermal stability. Among these, cassava stems possessed a relatively high cellulose content and MCC recovery efficiency, second only to pineapple leaves. Moreover, cassava stems are widely available across Vietnam - from North to South - particularly in provinces such as Tay Ninh province, Gia Lai province, Dak Lak province, Quang Ngai province, Dong Nai province, Nghe An province, Phu Tho province, and Son La province. Therefore, MCC derived from cassava stems offers the most favorable combination of recovery yield, particle uniformity, crystallinity index, and thermal stability. Given both its material performance and the abundance of feedstock, cassava stem-derived MCC is the most practical and sustainable source for large-scale production. Consequently, it was selected for subsequent composite fabrication with TPS and PLA to ensure optimal reinforcement efficiency and processing stability.

3.2. Structural, thermal, and morphological analysis of MCC-reinforced TPS/PLA composites

3.2.1. X-ray diffraction

The XRD pattern of the PLA sample (Figure 7a) exhibited characteristic diffraction peaks at 2θ ≈ 16.8°, 19.1°, 22.6°, and 28.9°. The most intense diffraction peak at 2θ = 16.8° corresponds to the (200)/(110) lattice planes, confirming the predominance of the α-form crystalline phase of PLA, which is known to be the thermodynamically most stable crystalline modification of polylactic acid.

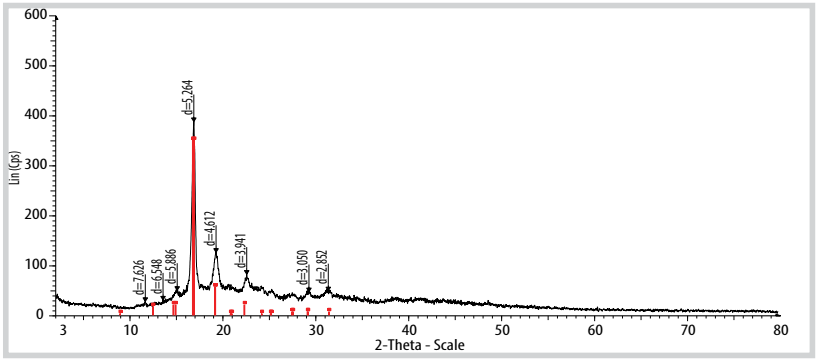

(a)

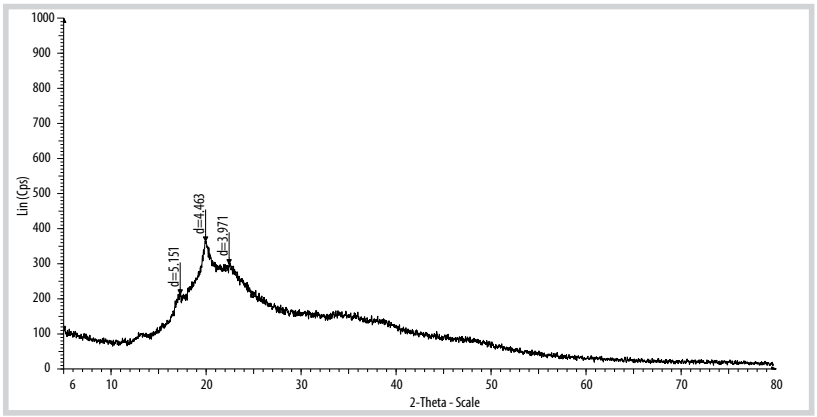

(b)

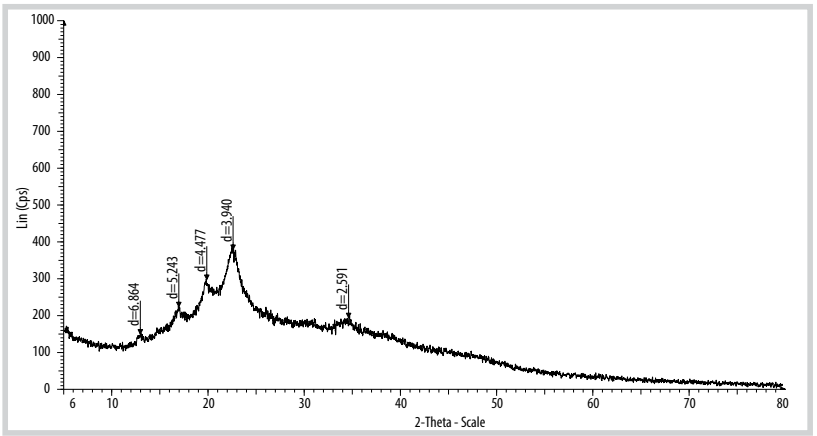

(c)

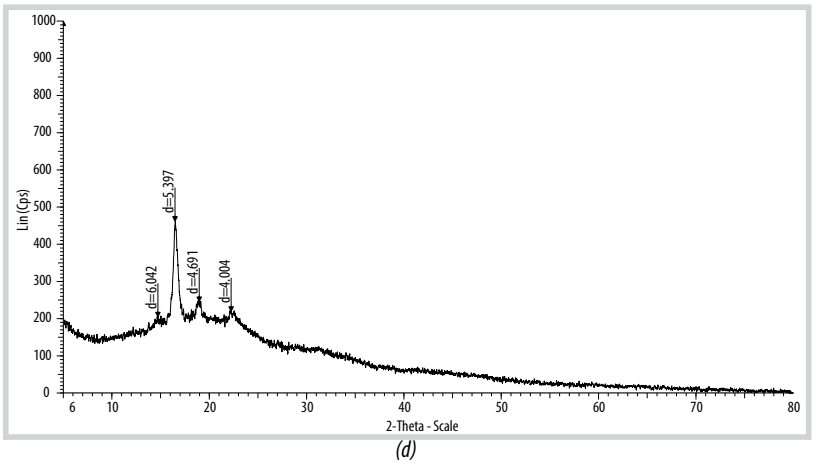

(d)

Figure 7. *X-ray diffraction patterns of (a) PLA, (b) thermoplastic starch (TPS), (c) MCC/TPS, and (d) PLA/(MCC/TPS) composites.*

Upon thermoplasticization with glycerol and water, the TPS (Figure 7b) sample showed a substantial reduction or complete disappearance of these crystalline peaks, replaced by a broad amorphous halo at 2θ ≈ 17° - 22.5°, confirming the disruption of the semi-crystalline starch structure during gelatinization and melt processing.

In the MCC/TPS composite (Figure 7c), the amorphous halo of TPS remained, while characteristic cellulose I peaks of MCC at 2θ ≈ 16.0°, 22.5°, and 34.5° appeared with increased intensity, resulting in a higher overall crystallinity. This confirms MCC's role as a crystalline reinforcing phase dispersed within the amorphous TPS matrix.

For PLA/(MCC/TPS) composites (Figure 7d), diffraction peaks at 2θ ≈ 15°, 16.5°, 19°, and 22.5° were observed, corresponding to PLA's crystalline structure alongside the amorphous halo of TPS and MCC peaks. The coexistence of these crystalline and amorphous domains suggests a multiphase morphology without complete miscibility among the components.

3.2.2. Thermal analysis

The TGA/DTG results revealed that the TPS, MCC/TPS, and PLA/(MCC/TPS) samples exhibited two main stages of mass losss with increasing temperature. The first stage (below 200°C) corresponds to the evaporation of moisture and partial volatilization of glycerol-rich phases, with weight losses of 11.39%, 10.55%, and 15.16% for TPS, MCC/TPS, and PLA/(MCC/TPS), respectively. In contrast, the mass of the PLA sample remained nearly constant in this region, confirming its high thermal stability and the absence of chemical degradation.

The second stage (200 - 600°C) is associated with the thermal degradation of starch-rich phases, overlapping with the decomposition of MCC. The major

weight losses were 88.56% for TPS, 89.03% for MCC/TPS, and 84.78% for PLA/(MCC/TPS), with corresponding DTA peaks at 315.02°C, 326.84°C, and 348.55°C. This stage highlights the difference in degradation mechanisms between PLA and starch/cellulose-based systems. Pure PLA underwent a single major decomposition step at 355.69°C, resulting in a mass loss of approximately 87.99%. The lower degradation temperatures observed for TPS, MCC/TPS, and PLA/(MCC/TPS) compared to pure PLA indicate that incorporating MCC/TPS into the PLA matrix increased the residual char yield and slightly reduced the decomposition temperature. These effects reflect the influence of interfacial interactions and the degree of MCC dispersion within the PLA matrix on the overall thermal stability of the composites.

3.2.3 Morphological analysis (SEM)

The SEM image of neat PLA (Figure 9a) shows a relatively smooth and dense surface with slight roughness, indicating the coexistence of amorphous and crystalline regions. No visible cracks or phase separation are observed, confirming the good morphological stability of pure PLA.

In contrast, the TPS sample (Figure 9b) displays a rough and irregular surface with micro-voids and discontinuities, suggesting incomplete gelatinization and partial incompatibility between starch and the plasticizer. For the MCC/TPS composite (Figure 9c), bright particles corresponding to MCC are observed partially embedded in the starch matrix, indicating non-uniform dispersion and partial aggregation of MCC.

The PLA/(MCC/TPS) composites (Figure 9d) exhibit smoother and more compact fracture surfaces, implying finer dispersion and improved compatibility between PLA and TPS. This enhancement is likely due to branching and crosslinking reactions between maleic anhydride–modified PLA (PLA-MA) and hydroxyl groups of starch, which reduce interfacial tension and improve miscibility at the polymer–filler interface.

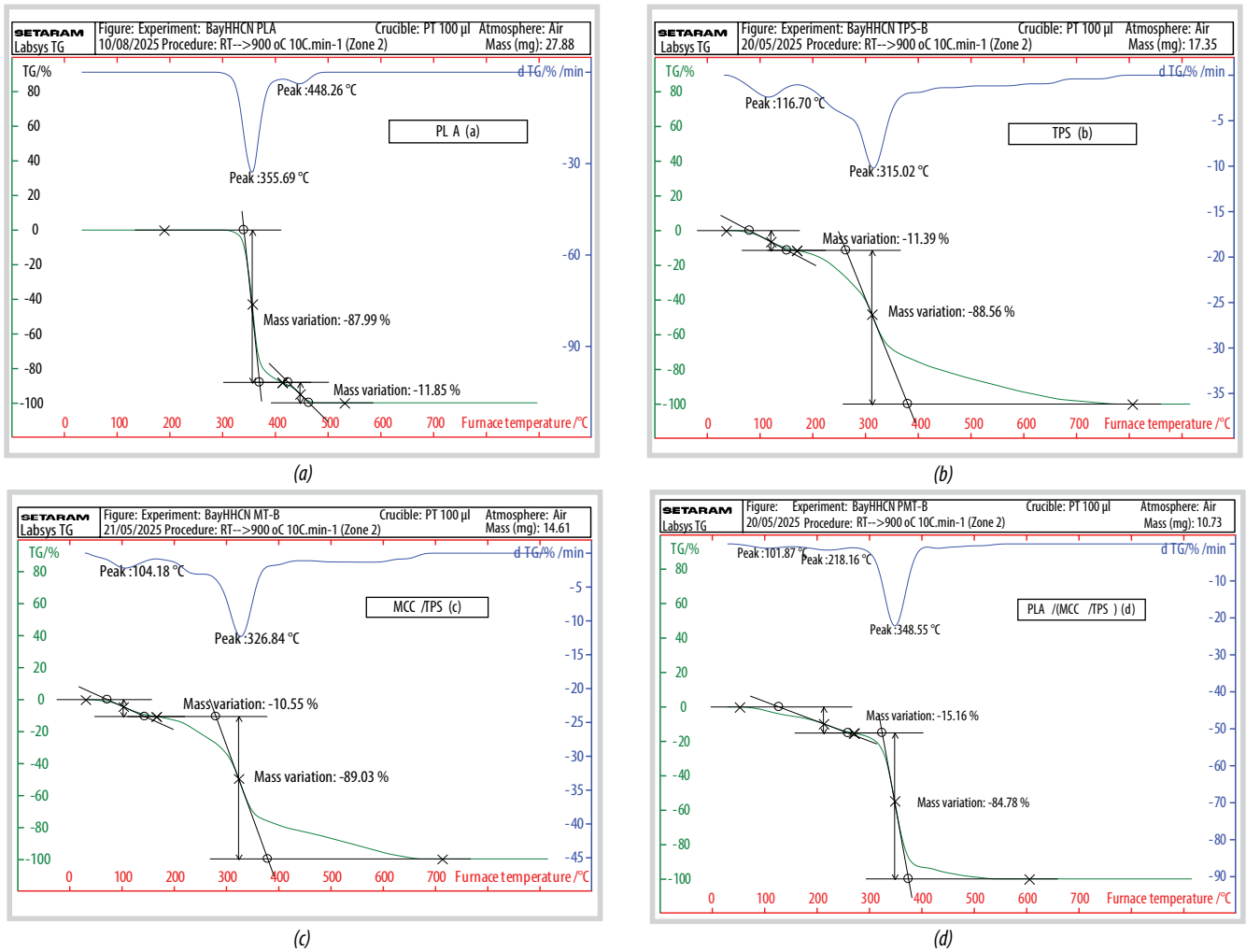

Figure 8. *TG-DTA thermal analysis curves of (a) PLA, (b) TPS, (c) MCC/TPS, and (d) PLA/(MCC/TPS) composites.*

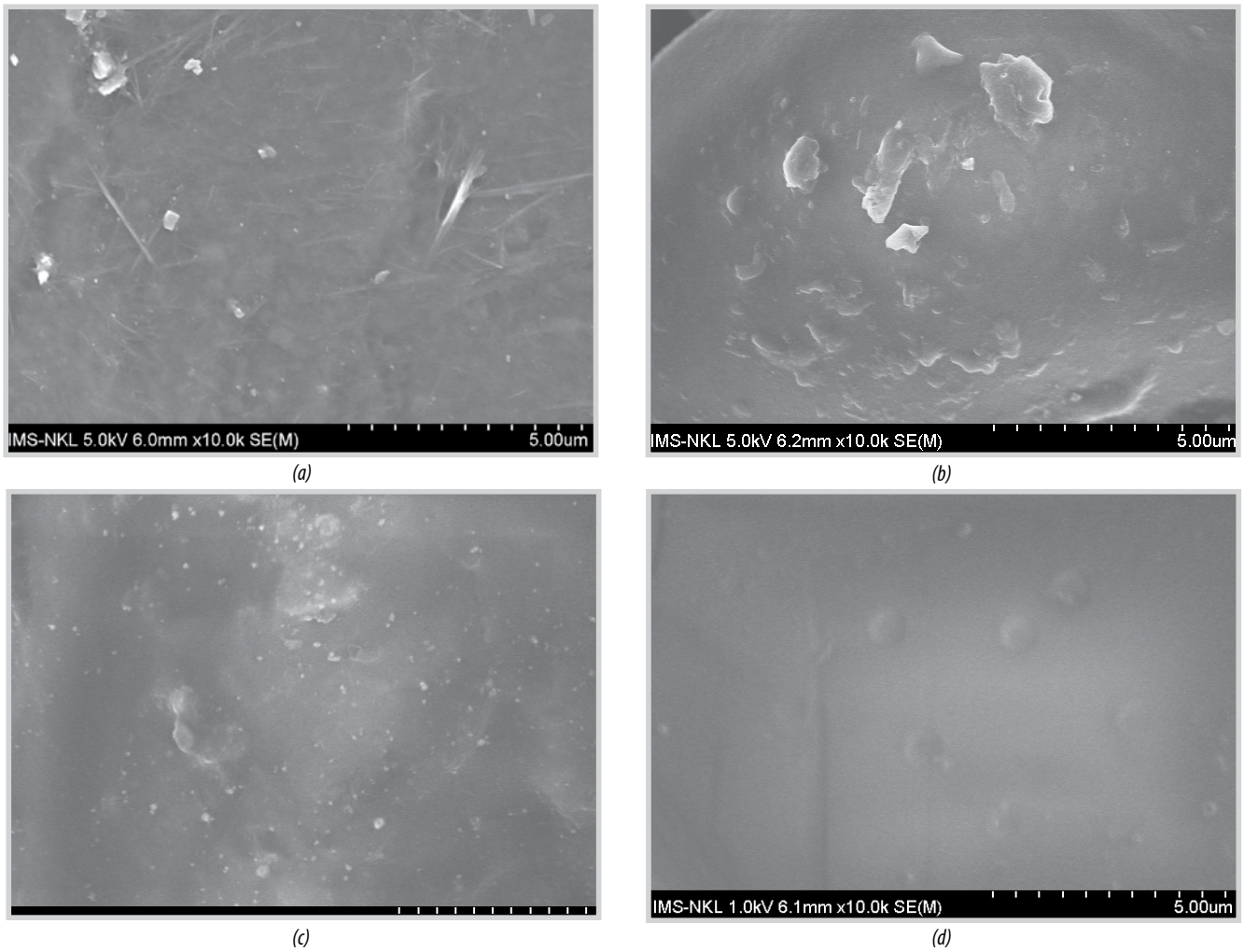

Figure 9. *Scanning electron microscopy (SEM) images of (a) PLA, (b) TPS, (c) MCC/TPS, and (d) PLA/(MCC/TPS) composites.*

These morphological findings support the hypothesis that well-dispersed MCC (≤15 wt%) enhances interfacial bonding and mechanical reinforcement, whereas excessive MCC loading (≈20 wt%) tends to induce particle agglomeration, decreasing composite uniformity and ductility.

3.3. Mechanical properties of PLA/(MCC/TPS) composites

Table 4 summarizes the tensile strength, elongation at break, and elastic modulus of the composites. Increasing TPS and MCC content led to a progressive decrease in tensile strength and elongation, consistent with the reduction of PLA's reinforcing fraction.

The B70:4.5:25.5 formulation (PLA:MCC:TPS = 70:4.5:25.5), corresponding to 15 wt% MCC in the MCC/TPS blend, exhibited the best balance of mechanical performance and biodegradability, making it suitable for packaging or food tray applications. The observed mechanical trends were consistent with the structural and morphological analyses, where SEM images revealed that improved MCC dispersion enhanced the tensile strength relative to pure PLA. TGA/DTA results indicated greater thermal stability, contributing to improved durability during melt processing. XRD analysis confirmed the presence of crystalline MCC, which increased the stiffness of the composites. However, excessive MCC loading led to embrittlement, emphasizing the need for optimized filler content.

4. Conclusions

Microcrystalline cellulose was extracted from cassava stems, banana pseudostems, pineapple leaves, and spent coffee grounds. Among these sources, cassava stem MCC was identified as the most feasible and sustainable source due to its high crystallinity, uniform particle dimensions, processing stability, ready availability, and large-scale supply potential. This MCC was subsequently incorporated into thermoplastic starch and polylactic acid matrices

Table 4. *Mechanical properties of the composite materials.*

Sample	Tensile strength (MPa)	Elongation at break (%)	Elastic modulus (MPa)
A80:2:18	41.2	7.1	1980
A70:3:27	35.0	6.3	1725
B70:4.5:25.5	32.5	5.5	1850
B60:6:34	29.2	4.1	1900
C60:8:32	25.5	3.2	2000
PLA	45	3.5	2500

to produce fully biodegradable composites. Structural, morphological, and thermal analyses confirmed that well-dispersed MCC acts as an effective reinforcing phase, enhancing tensile strength, elastic modulus, and thermal stability. The optimized PLA:MCC:TPS ratio of 70:4.5:25.5 (corresponding to 15 wt% MCC in the MCC/TPS blend) achieved the best balance between mechanical performance and biodegradability, making the resulting composites suitable for sustainable packaging and food service applications. These findings align with global energy transition strategies and CO_2 mitigation objectives, offering a viable pathway to replace petrochemical-based plastics in targeted sectors.

References

[1] K.O. Reddy, C. Uma Maheswari, E. Muzenda, M. Shukla, and A.V. Rajulu, "Extraction and characterization of cellulose from pretreated ficus (peepal tree) leaf fibers", *Journal of Natural Fibers*, Volume 13, Issue 1, pp. 54 - 64, 2016.

[2] Naved Azum, Mohammad Jawaid, Lau, Kia Kian, Anish Khan, and Maha Moteb Alotaibi, "Extraction of microcrystalline cellulose from Washingtonia fibre and its characterization", *Polymers*, Volume 13, Issue 18, 2021. DOI: 10.3390/polym13183030.

[3] C. Uma Maheswari, K. Obi Reddy, E. Muzenda, B. Guduri, and A. Varada Rajulu, "Extraction and characterization of cellulose microfibrils from agricultural residue - Cocos nucifera L", *Biomass and Bioenergy*, Volume 46, pp. 555 - 563, 2012. DOI: 10.1016/j.biombioe.2012.06.039.

[4] P. Nehra and R.P. Chauhan, "Facile synthesis of nanocellulose from wheat straw as an agricultural waste", *Iranian Polymer Journal*, Volume 31, Issue 6, pp. 771 - 778, 2022. DOI:10.1007/s13726-022-01040-0.

[5] Mohd Yussni Hashim, Azriszul Mohd Amin, Omar Mohd Faizan Marwah, Mohd Hilmi Othman, Mohd Radzi Mohamed Yunus, and Ng Chuan Huat, "The effect of alkali treatment under various conditions on physical properties of kenaf fiber", *Journal of Physics: Conference Series*, Volume 914, 2017. DOI: 10.1088/1742-6596/914/1/012030.

[6] Selwin Maria Sekar, Rajini Nagarajan, Ponsuriyaprakash Selvakumar, Nadir Ayrilmis, Kumar Krishnan, Faruq Mohammad, Hamad A. Al-Lohedan, and Sikiru O. Ismail, "3D-printed green biocomposites from poly(lactic acid) and pine wood-derived microcrystalline cellulose: Characterization and properties", *BioResources*, Volume 20, Issue 4, pp. 8473 - 8492, 2025. DOI: 10.15376/biores.20.4.8473-8492.

[7] M.K. Mohamad Haafiz, Azman Hassan, Zainoha Zakaria, I.M. Inuwa, M.S. Islam, M. Jawaid, "Properties of polylactic acid composites reinforced with oil palm biomass microcrystalline cellulose", *Carbohydrate Polymers*, Volume 98, Issue 1, 15, pp. 139 - 145, 2013.

[8] Nanang Triyono, Fatma Sari, Ika Kurniaty, Ratri Ariatmi Nugrahani, Tri Yuni Hendrawati, and Susanty, "Characterization of microcrystalline cellulose from cassava stems through acid hydrolysis process using H_2SO_4 with variation concentration", *International Conference on Engineering, Construction, Renewable Energy, and Advanced Materials, Fakultas Teknik Universitas Muhammadiyah Jakarta, 30 April 2024*.

[9] Jie Chen, Xia Wang, Zhu Long, Shuangfei Wang, Jingxian Zhang, and Lei Wang, "Preparation and performance of thermoplastic starch and microcrystalline cellulose for packaging composites: Extrusion and hot pressing", *International Journal of Biological Macromolecules*, Volume 165, pp. 2295 - 2302, 2020. DOI: 10.1016/j.ijbiomac.2020.10.117.

[10] Daniele Rigotti, Luca Fambri, Alessandro Pegoretti, "Bio composites for fused filament fabrication: effects of maleic anhydride grafting on poly(lactic acid) and microcellulose", *Progress in Additive Manufacturing*, Volume 7, pp. 765 - 783, 2022. DOI: 10.1007/s40964-022-00264-z.

[11] Nehemiah Mengistu Zeleke, Devendra Kumar Sinha, and Getinet Asrat Mengesha, "Chemical composition and extraction of micro crystalline cellulose from outer skin isolated coffee husk", *Advances in Materials Science and Engineering*, 2022. DOI: 10.1155/2022/7163359.

[12] Wei Sing Yong, Yee Lee Yeu, Ping Ping Chung, and Kok Heng Soon, "Extraction and characterization of microcrystalline cellulose (MCC) from durian rind for biocomposite application", *Journal of Polymers and the Environment*, Volume 32, pp. 6544 - 6575, 2024. DOI: 10.1007/s10924-024-03401-7.

[13] Yanlan Liu, Jingfeng Ran, Ziyang Xu, Hao Cheng, Benping Lin, Tianran Deng, and Cuiping Yi, "Preparation and characterization of microcrystalline cellulose from rice bran", *Journal of the Science of Food and Agriculture*, Volume 105, Issue1, pp. 218 - 226, 2025. DOI: 10.1002/jsfa.13820.

[14] Xutong Wang, Xiaoqiang Cui, Yuechi Che, Shengquan Zhou, Zeng Dan, Beibei Yan, Guanyi Chen, and Ting Wang, "Gasification of Tibetan herb residue: Thermogravimetric analysis and experimental study", *Biomass and Bioenergy*, Volume 146, 2021. DOI: 10.1016/j.biombioe.2020.105952.

[15] Raquel S. Reis, Lucas G.P. Tienne, Diego de H.S. Souza, Maria de Fátima V. Marques, and Sergio N. Monteiro, "Characterization of coffee parchment and innovative steam explosion treatment to obtain micro - brillated cellulose as potential composite reinforcement", *Journal of Materials Research and Technology*, Volume 9, Issue 4, pp. 9412 - 9421, 2020. DOI: 10.1016/j.jmrt.2020.05.099.

[16] Putri Nawangsari, Warman Fatra, Aryandi Kusuma, Muftil Badri, Dedi Rosa P.C, and Dedy Masnur, "Microcellulose from pineapple leaf Fiber as a potential sustainable material: Extraction and characterization", *Journal Polimesin*, Volume 22, Issue 1, 2024.

[17] Sataporn Malarat, Dilawin Khongpun, Kanokkorn Limtong, Napasin Sinthuwong, Pornpinun Soontornapaluk, Chularat Sakdaronnarong, and Pattaraporn Posoknistakul, "Preparation of nanocellulose from coffee pulp and its potential as a polymer reinforcement", *ACS Omega*, Volume 8, Issue 28, pp. 25122 - 25133, 2023. DOI: 10.1021/acsomega.3c02016.

[18] Djalal Trache, André Donnot, Kamel Khimeche, Riad Benelmir, and Nicolas Brosse, "Physico-chemical properties and thermal stability of microcrystalline cellulose isolated from alfa fibres", *Carbohydrate Polymers*, Volume 104, pp. 223 - 230. 2014. DOI: 10.1016/j.carbpol.2014.01.058.

PETROVIETNAM
SCIENCE, TECHNOLOGY & INNOVATION PETROVIETNAM

URBAN MOTORCYCLE EXHAUST EMISSIONS IN VIETNAM: STATUS AND TECHNICAL SOLUTIONS

Phan Vu Anh, Nguyen Van Tu, Hoang Linh Lan, Le Quang Hung
Vietnam Petroleum Institute (VPI)
Email: anhpv@vpi.pvn.vn
https://doi.org/10.47800/PVSI.2025.06-08

Summary

Vietnam's major cities experience severe air pollution with Hanoi recording $PM_{2.5}$ concentration of approximately 45 µg/m^3, nearly 9 times higher than the WHO guideline value. This situation is driven by 77 million motorcycles, of which 70% are over 10 years old and 94% lack emission control systems. Motorcycles account for about 76% of urban CO, 68% of HC, and 54% of NO_x. The transition toward electric vehicles faces critical challenges, including 10 - 15 years of infrastructure development versus an 18-month policy deadline, battery production emissions (60 - 100 kg CO_2/kWh), and coal-thermal electricity transferring pollution. This paper analyzes emission control technologies and reveals that electronic fuel injection and E10 achieve only 30 - 40% reductions while increasing NO_x, whereas three-way catalytic converters demonstrate more than 85% reduction across all pollutants at significantly lower cost than immediate electric vehicle conversion. A two-phase framework is proposed: i) immediate retrofitting (2025 - 2028) supported by clean fuel supply and gas power expansion, and ii) a systematic transition (2028 - 2040) enabled by diversified clean energy infrastructure, metro networks, and green hydrogen ecosystem. Throughout both phases, coordination with the petroleum sector is emphasized to ensure energy security during the transformation.

Key words: Catalytic converter, motorcycle emissions, air pollution, Vietnam, emission control technology.

1. Current air pollution status and motorcycle contribution

Vietnam's major cities confront unprecedented air pollution, with $PM_{2.5}$ concentrations persistently reaching hazardous levels. Throughout early December 2025, Hanoi experienced severe episodes with AQI ranging 187 - 275 citywide, corresponding to $PM_{2.5}$ concentrations of 110 - 170 µg/m^3 (22 - 34 × WHO guideline). The 2024 annual average $PM_{2.5}$ concentration reached 45 µg/m^3 (9 × WHO guideline), placing Hanoi among Asia's most polluted capitals [1].

According to World Bank analysis using the GAINS model for Hanoi's PM2.5 emissions in 2015, the transportation sector contributed 15% from vehicle exhaust and 23% from road dust, representing a combined 38% of total air pollution. Other major sources included industrial activities (29%), open burning of rice straw (26%), and residential/commercial combustion (7%) [2].

However, the transportation contribution may have increased substantially since 2015. Vietnam's motorcycle fleet has grown from approximately 44 million units in 2015 to over 77 million by 2024 - a 75% increase. This dramatic expansion in motorcycle ownership, representing one of the world's highest rates at 770 motorcycles per 1,000 people, suggests that transportation's share of air pollution has likely increased beyond the 38% recorded in 2015. Motorcycles are the dominant emission source within the transportation sector. Studies demonstrate that motorcycles are responsible for 60% of transport-related PM2.5 in Ho Chi Minh City and contribute 68 - 70% of PM2.5 emissions from the transportation sector across major Vietnamese cities. The high emissions stem from widespread use of aging gasoline-powered motorcycles with inadequate emission controls and limited public transportation infrastructure [3 - 5].

Date of receipt: 2/12/2025.
Date of review and editing: 2 - 15/12/2025.
Date of approval: 15/12/2025.

Figure 1. *Hanoi air quality spatial distribution in December 2025.*

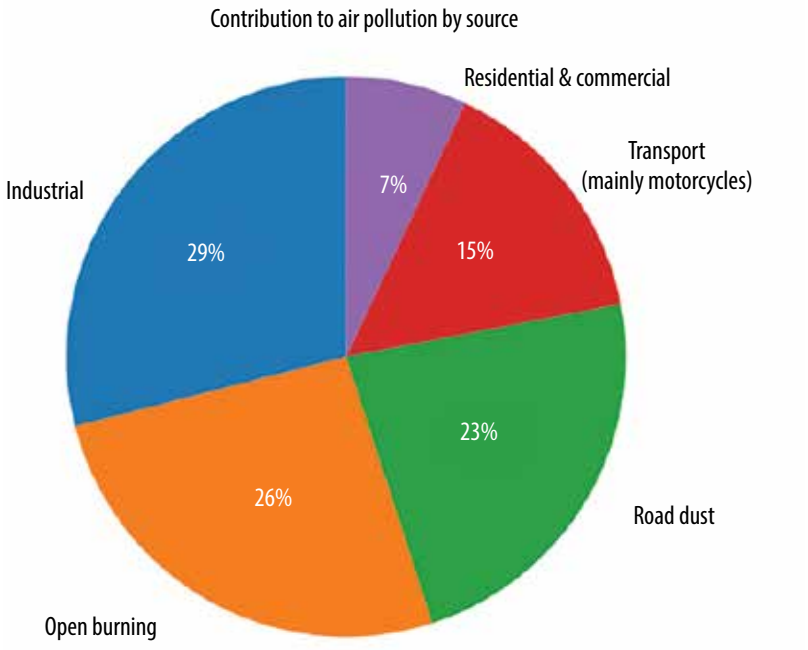

Figure 2. *Illustrative $PM_{2.5}$ source contribution breakdown for Hanoi (conceptual schematic).*

2. Government policies and electric vehicle transition challenges

2.1. Emission standards and geographic restrictions

Vietnam's regulatory response employs dual strategies: emission standards tightening and accelerated electrification. Decision 19/2024/QĐ-TTg mandates Euro 4 compliance (CO ≤ 1.14 g/km, HC ≤ 0.38 g/km, NO_x ≤ 0.07 g/km) for new motorcycles by July 2026 and mopeds by July 2027 [6]. However, these standards apply only to new vehicle sales, creating a regulatory gap with the existing 77 million-unit fleet where 70% exceed 10 years of age.

Implementation employs graduated geographic restrictions. Hanoi's resolution dated November 26, 2025, establishes low-emission zones centered on Ring Road 1, with time-based restrictions taking effect on July 1, 2026, and affecting approximately 450,000 motorcycles. The zone will expand progressively through Ring Roads 2 and 3 by 2028 and 2030, respectively. Ho Chi Minh City pursues a parallel phased implementation targeting the complete prohibition of gasoline motorcycles in downtown by 2032.

2.2. Electric vehicle transition barriers

The electric vehicle transition represents the primary long-term compliance solution but it confronts severe barriers across three dimensions:

Infrastructure: Ho Chi Minh City's 600 charging points serve fewer than 10,000 EVs, requiring expansion to 3,000 stations by December 2028-a 400% increase in 36 months. More critically, Vietnam's 2023 electricity crisis caused USD 1.4 billion in economic losses. Converting millions of motorcycles would demand substantial generating capacity, with coal-thermal sources (47% of electricity) merely transferring emissions from urban to rural areas without net pollution reduction.

Economic: Electric motorcycles are priced at VND 20 - 40 million versus equivalent gasoline models at VND 15 - 25 million, representing a 30 - 60% premium. Battery replacement (VND 8 - 12 million after 5 - 7 years) eliminates operational savings, creating total ownership costs exceeding conventional motorcycles over a typical 10-year lifespan. Current subsidies address only 14% of targeted fleets.

Environmental: Lithium-ion battery production generates significant upstream emissions through energy-intensive mining (lithium, cobalt, nickel) causing water/soil pollution and manufacturing processes, with 60 - 100 kg CO_2 emissions per kWh battery capacity. A typical electric motorcycle battery (1.5 - 2 kWh) embeds 90 - 200 kg CO_2 before first use, requiring 5,000 - 10,000 km operation to offset manufacturing emissions-negating short-term air quality benefits in emission-constrained scenarios. Downstream, batteries require specialized recycling facilities absent at commercial scale in Vietnam. The VinES-Li-Cycle partnership

Figure 3. *Motorcycle scrapyard.*

targets facility commissioning in 2025, which is obviously insufficient for current policy deadlines. With 8- to 10-year battery lifespans, large-scale adoption would generate massive waste streams from 2031 onward, while current facilities landfill 85% of 400,000 tons of annual motorcycle waste without treatment. This lifecycle pollution burden - from mining regions to manufacturing zones to disposal sites - often transfers environmental costs to less developed regions rather than eliminating them [2, 6].

2.3 Public transport infrastructure gaps

Public transportation development in both Hanoi and Ho Chi Minh City remains insufficient to support the immediate motorcycle phase-out. Hanoi operates 2 metro lines (Line 2A since November 2021 and partial Line 3 since August 2024) with plans for 8 lines totaling 318 km under Prime Minister Decision 519/QĐ-TTg. Ho Chi Minh City inaugurated Line 1 (19.7 km) in December 2024, with the city's urban railway master plan targeting approximately 510 km total system length requiring an estimated USD 24 billion investment under Decision 1711/QĐ-TTg dated December 31, 2024. Even with aggressive development timelines, completing these metro networks extends beyond 2027. Existing diesel bus fleets compound the pollution challenge rather than offering solutions. Hanoi's public transport system comprises 2,279 buses, of which 86.8% (over 2,000 vehicles) remain diesel-powered, with only 277 buses (13.6%) using green energy. Ho Chi Minh City operates 2,209 buses with 546 green energy vehicles. Both cities target 100% green energy bus conversion by 2030, but current diesel operations contribute to, rather than mitigate, urban air pollution. Combined metro-bus systems cannot absorb 77 million motorcycles within policy timeframes, creating implementation gaps between emission reduction targets and infrastructure readiness [7, 8].

2.4. Timeline mismatch and international lessons

Chinese cities provide instructive precedent. Over 160 cities implemented motorcycle restrictions by 2009, substantially increasing travel costs for low-income workers and collapsing China's motorcycle market from 26.9 million (2014) to 15.5 million (2018) sales. Shanghai's success required over 20 years of sustained infrastructure investment combined with effective restrictions, rather than rapid policy implementation.

Timeline analysis reveals a fundamental mismatch: systematic EV transition and public transport development require 10 - 15 years, yet policy deadlines allow only 18 months before Euro 4 enforcement. Given that comprehensive metro completion and bus electrification cannot be achieved within this timeline, interim emission control solutions for the existing motorcycle fleet become essential. Bridge solutions must meet four criteria: proven emission reduction achieving Euro 4 compliance (>75% reduction across all pollutants), economic accessibility (VND 2 - 5 million), technical compatibility with an aging fleet regardless of mechanical condition, and social equity protecting livelihoods while advancing environmental objectives [9].

3. Technical solutions for the existing motorcycle fleet

Emission control strategies are divided into primary methods (combustion optimization) and secondary methods (exhaust aftertreatment). Primary methods target pollutant formation at source through improved fuel-air mixing and combustion completeness. Secondary methods chemically convert already-formed pollutants before atmospheric release. While primary methods offer measurable improvements, their reduction magnitudes prove insufficient for Euro 4 compliance, particularly for aging engines where degradation limits optimization potential.

3.1. Primary methods: Combustion efficiency enhancement

Electronic fuel injection (EFI) retrofitting: Replacing carburetors with electronic fuel injection delivers precise fuel metering

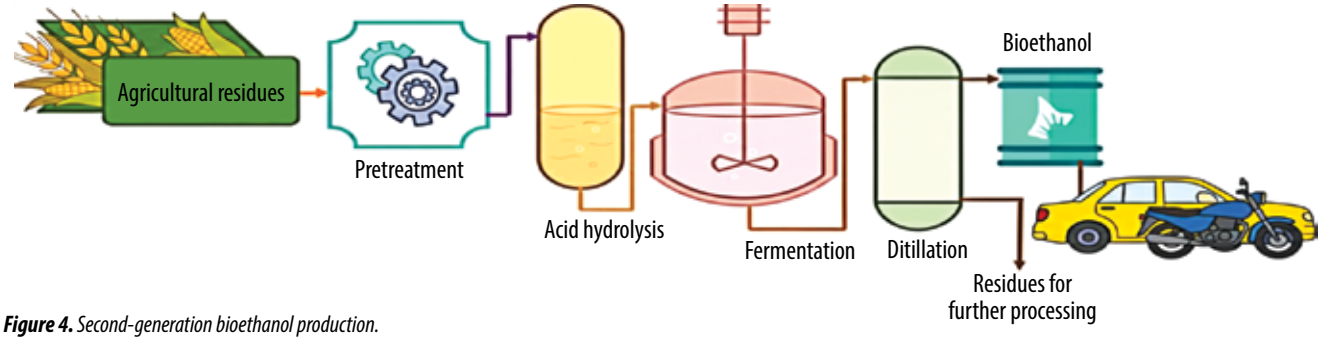

Figure 4. *Second-generation bioethanol production.*

through oxygen sensor feedback. Field studies on 125cc motorcycles documented 82 - 96% CO and 36 - 55% HC reduction but paradoxically doubled NO_x emissions through elevated cylinder temperatures [10]. Retrofit costs of VND 3 - 5 million with 4 - 6 hour installation limit practical applicability to ~40% of Vietnam's fleet, only well-maintained post-2010 motorcycles with adequate electronic infrastructure.

Biofuel (E10) integration: Laboratory studies document 10 - 13% CO and 10 - 15% HC reduction but 40% NOx increase and 51% particle number concentration rise. Vietnam mandates nationwide E10 deployment from June 1, 2026 (Decision 46/2025/QĐ-TTg, Circular 50/2025/TT-BCT), transitioning to E15 by January 2031. However, critical constraints persist that domestic production (450,000 m^3/year from 2 operating plants) meets only 30 - 40% of demand (1.2 - 1.5 million m^3/year), requiring 60% imports. Cassava feedstock causes severe soil erosion (20 - 40 tons/hectare annually) and demands high fertilizer inputs. Second-generation lignocellulosic facilities require USD 100 - 200 million investment per plant with only 2 of 6 planned facilities currently in operation [11, 12].

Fuel additives: Commercial additives claim 5 - 15% emission reductions but independent testing demonstrates minimal benefits. Indonesian studies found bio-additives increased CO_2 emissions (0.28 - 8.01 ppm/ml) versus synthetic additives (0.88 - 13.17 ppm/ml) [13]. Annual costs (VND 1.2 - 3.6 million) approach catalytic converter capital costs without proven emission reductions for aging motorcycles.

Although EFI optimization and E10 fuel adoption can achieve up to 30 - 40% emission reductions, these measures alone do not reliably ensure compliance with applicable motorcycle emission standards (Level 2-3) across the legacy fleet, as emission performance among very old and carbureted motorcycles remains highly variable and difficult to control in the absence of exhaust after-treatment.

3.2. Secondary methods: catalytic converter technology - Application scope and global market

Catalytic emission control technology has evolved into a global industry with two main segments:

Transportation: Market reached USD 169.5 billion (2024) and is forecasted to grow to USD 387.8 billion (2034), corresponding to a CAGR of 8.6%/year. This segment includes three-way catalysts for gasoline engines, diesel oxidation catalysts (DOC) and selective catalytic reduction (SCR) for trucks, ships, and mobile machinery. The Asia-Pacific region accounts for 49.8% of the global market share.

Stationary industrial: Market reached USD 24.5 billion (2024) and is forecasted to attain USD 33.1 billion (2033), corresponding to a CAGR of 3.3%/year. Applications include coal/gas power plants (67.8% market share), refineries (FCC, hydrotreating), cement (kiln DeNOx), steel (blast furnaces), chemicals (VOC treatment), and large marine vessels.

The total global catalytic emission control market exceeded USD 194 billion in 2024, reflecting its essential role in global air pollution control [14, 15].

Operating principles of three-way catalysts

Three-way catalysts (TWC) operate through heterogeneous catalysis on ceramic/metallic substrates (400 - 900 cells/$inch^2$) coated with Al_2O_3-CeO_2-ZrO_2 washcoat containing nano-sized precious metals (Pt, Pd, Rh). At 350 - 900°C, three simultaneous reactions occur:

Oxidation (Pt, Pd):

$$2CO + O_2 \rightarrow 2CO_2$$

$$C_3H_8 + 5O_2 \rightarrow 3CO_2 + 4H_2O$$

Reduction (Rh):

$$2NO + 2CO \rightarrow N_2 + 2CO_2$$

$$C_3H_8 + 10NO \rightarrow 5N_2 + 3CO_2 + 4H_2O$$

Figure 5. *Catalytic converter installation and various product configurations.*

Performance: Reduction achieves >95% for CO, >90% for HC, >85% for NOx at λ = 0.97 - 1.03, exceeding Euro 4 requirements. Lifespan exceeds 100,000 km with fuel <10 ppm sulfur [16, 17].

- Research achievements and technology gaps for motorcycles

Developed markets: Euro 4 (2016) and Euro 5 (2021) drove advanced technologies-metallic substrates 600 - 900 cpsi for rapid light-off, Pt:Pd:Rh = 5:5:1 cost optimization, CeO_2-ZrO_2 washcoat thermal stability, close-coupled positioning reducing light-off time to <60 seconds. India (BS-VI 2020) achieved a 70% reduction in particulates, while China (GB14622-2016) applied Pd-Rh systems with HC+NOx ≤0.12 g/km [13, 14]. However, these technologies serve premium new motorcycles (>VND 100 million), while European aftermarket exhaust systems cost VND 15 - 30 million, which is therefore unsuitable for low-cost used motorcycle retrofits.

Vietnamese research: Prof. Le Minh Thang (Hanoi University of Science and Technology) developed MnO_2-Co_3O_4-CeO_2 catalysts on cordierite substrates (Vietnam Patent 20257/2018) without precious metals, achieving > 90% CO/HC at 350 - 400°C with ~50% lower cost, indicating strong potential to reduce import dependence [15]. Challenges: NOx performance has not yet reached the >85% level required for full Euro 4 compliance; long-term testing under tropical conditions (25 - 35°C, 80 - 95% humidity), high-sulfur fuels (50 - 150 ppm vs < 10 ppm in the EU), and aged engines with oil consumption have not been conducted. The technology has not yet been commercialized, and would require about 3 - 5 years and tens of billions of VND investment for market readiness.

Critical gaps: OEMs (Bosch, Denso) serve only new vehicles. European aftermarket products are costly. Asian aftermarket alternatives often exhibit poor quality (Pt/Pd/Rh 30 - 50% below standards, lifespan <30,000 km, and counterfeits widespread). There is a lack of products that are suitable for tropical climates, compatible with aged motorcycles, while affordable for Vietnam's 77 million fleet.

- Feasibility potential for Vietnamese used motorcycles

With Euro 4 standards applying to new motorcycles from July 2026, Vietnam must also address emissions from an existing fleet of approximately 77 million motorcycles, of which around 70% are over 10 years old and 94% lack exhaust after-treatment. While Euro 4 requirements do not apply to legacy vehicles, their age and technical heterogeneity significantly limit the effectiveness of primary emission control measures.

Among the evaluated technologies, exhaust catalytic after-treatment emerges as one of the most feasible short- to medium-term options for emission control in used motorcycles, as it enables the simultaneous reduction of CO, HC, and NO_x while delivering more consistent performance across heterogeneous and aging vehicle conditions. This assessment refers to improving compliance with applicable in-use emission standards and reducing real-world emissions, rather than retrofitting legacy motorcycles to Euro 4 requirements.

Support requirements: (i) the establishment of a clear regulatory framework for vehicle inspection following exhaust system modifications; (ii) the progressive availability of ultra-low sulfur fuels to ensure catalyst durability; (iii) the development of quality standards and certification mechanisms to prevent counterfeit products; and (iv) supportive fiscal policies, such as tax exemptions or reductions for catalyst-related components and materials, to facilitate cost-effective deployment. In parallel, continued research on domestically developed catalyst technologies, including non-precious metal systems, should be encouraged to improve NOx conversion efficiency, validate field performance, and advance commercialization, thereby reducing long-term costs [18].

4. Strategic assessment and implementation pathways

4.1. Short-term strategy (2025 - 2028): Controlling current emissions

Objective: To reduce emissions from 77 million motorcycles by 60 - 70% through a two-tier strategy: mandatory Euro 4 with integrated three-way catalysts for new vehicles from January 2027 (fundamental solution), retrofitting old vehicles with aftermarket catalysts during a 10 - 15 year transition. Three-way catalysts uniquely achieve Euro 4 simultaneously (>95% CO, >90% HC, >85% NOx), superior to EFI and E10.

Three-phase deployment: Ring Road 1 (approximately 600,000 vehicles, 2026 - 2027) → Ring Road 2-3 (~1.5 million vehicles, 2028 - 2029) → nationwide (from 2030 onward), with VND 1 – 2 million subsidies prioritizing low-income households, and a 50% corporate tax reduction for domestic catalyst manufacturers. Mandatory use of clean fuel E10 from June 2026, and gasoline with sulfur content <10 ppm from 2027 to prevent catalyst poisoning. Compulsory SCR systems with DEF for heavy-duty diesel vehicles from January 2027, reducing 80 - 95% NOx. Public transport is electrifying 50% of the bus fleet by 2027, completing Hanoi Metro Line 3, and expanding Ho Chi Minh City Lines 1 - 2.

Petrovietnam's role: Assigns member units with relevant functions to implement the following integrated solutions:

- Producing/distributing E10 and <10 ppm sulfur gasoline through refineries;

- The domestic production of ISO 22241–compliant diesel exhaust fluid (DEF), exemplified by Phu My Xanh, combined with distribution via existing fuel retail networks, provides an enabling foundation for large-scale deployment of SCR systems without relying on imported DEF supplies;

- Developing integrated clean agriculture–biorefinery hubs, leveraging Petrovietnam's existing gas-power-fertilizer infrastructure to convert agricultural residues into high-value products (essential oils, nanosilica, bio-based chemicals, biofuels), while strengthening control over informal open-field burning and reducing $PM_{2.5}$ and NH_3 emissions;

- Replicating Nhon Trach 3&4 model (1,624 MW, >62% efficiency) to O Mon IV and Long Phu 1, expanding capacity to 12,000 - 15,000 MW;

- Converting urban coal plants to gas, retrofitting aging plants with SCR/ESP/FGD reducing 20 - 30% industrial $PM_{2.5}$;

- Collaborating with universities developing non-precious metal catalysts for tropical climate, testing on 10,000+ vehicles, industrializing monazite-based cerium oxide washcoat, reducing costs 50 - 70%;

- Converting 5,000+ stations into catalyst sales/installation points;

- Optimizing refinery operations (BSR 95.6% reliability), environmental investment (for NSRP about USD 300 million), piloting clean hydrogen;

- Establishing centralized recycling treating 200,000 - 500,000 tons/year of plastics, 100,000 tons/year of waste oil.

4.2 Long-term strategy (2028 - 2040): Fundamental system transformation

Replace internal combustion engines achieving an 80 - 90% reduction by 2040. Prerequisites include 10,000 - 20,000 EV charging stations, grid upgrades, tropical-safe batteries, industrial-scale recycling, and cost reduction to 70 - 80% of gasoline vehicles. Hydrogen is designated for heavy-duty applications, while hybrids are for transition. The target is 30 - 50% electric/hydrogen vehicle new sales by 2035 (conservative scenario: 5 - 7 years extension).

Energy foundation: Renewables - solar and offshore wind (160 GW potential, with 6 GW pilot by 2030) targeting 30 - 40% of electricity generation; nuclear - deployment of Gen III/III+ reactors plus thorium reactor research utilizing ~600,000 tons of domestic monazite; and smart grid integration. Metro expansion (318 km in Hanoi, 85 km in Ho Chi Minh City by 2030) targets a 40 - 50% public transport share (realistically 30 - 35%). Green fuel ecosystem is envisaged when renewable electricity is sufficient, including green hydrogen from electrolysis, green ammonia for maritime applications, $CO_2 + H_2$ pathway to methanol/DME/synthetic diesel, and second-generation biofuels with E15 introduced from January 2031.

Petrovietnam's role: Coordinates member units leading transformation, including: Converting 5,000+ stations into integrated energy hubs (EV charging, H_2/ammonia fueling); Leveraging offshore expertise to provide EPCI/logistics services for offshore wind projects (GWO-certified workforce, major project bidding), partnering for renewable energy exports, integrating offshore wind with at-sea green hydrogen production;

Transitioning refineries toward high-value chemicals (e.g., benzene, paraxylene, polypropylene at Nghi Son), scaling clean hydrogen from pilot projects (2025 - 2030) to commercial deployment (beyond 2030) to serve refineries/fertilizer production/exports; Producing blue hydrogen from gas integrated with CCS, capturing 2 - 5 million tons CO_2/year in depleted fields and combining with EOR; Exporting green ammonia to Japan and Korea; Advancing CO_2 utilization and second-generation biofuels; Participating in the nuclear power program; Research on thorium molten-salt reactor (MSR) and rare-earth refining; Developing lithium/sodium battery; and expanding recycling systems.

Transition logic: Producer → Supporter (clean fuels, domestic catalysts, infrastructure, gas power, refinery greening, recycling, and DEF) → Leader (green energy, high-value chemicals, clean hydrogen, circular economy, and advanced technologies), ensuring national energy security throughout a 15 - 20 year transition.

References

[1] IQAir, *"World air quality report 2024"*, IQAir AG, Zurich, Switzerland, 2024.

[2] World Bank, "Air quality in Hanoi: Current situation & policy intervention", 2021.

[3] Vietnamnet, "Vietnam leads the world in motorcycle usage with over 77 million registered", 2024

[4] "Motorcycle industry in Vietnam", 2025.

[5] International Council on Clean Transportation, "Promoting the development of electric vehicles in Vietnam", 2022.

[6] Prime Minister of Vietnam, "Decision providing the roadmap for application of exhaust emission to manufactured, assembled and imported motorcycles vehicles", Decision No. 19/2024/QĐ-TTg, November 15, 2024.

[7] Southeast Asia Infrastructure, "Transforming urban mobility: The development of urban rail in Vietnam", 2024.

[8] Vietnam Briefing, "HCMC metro planning and transit-oriented development: Opportunities for foreign investment", 2025.

[9] Yuntao Guo, Jian Wang, Srinivas Peeta, and Panagiotis Ch. Anastasopoulos, "Personal and societal impacts of motorcycle ban policy on motorcyclists' home-to-work morning commute in China", *Travel Behaviour and Society*, Volume 19, pp. 137 - 150, 2020. DOI: 10.1016/j.tbs.2020.01.002.

[10] Teoh Say Lai and Horizon Gitano-Briggs, "Development of a small motorcycle EFI retrofit system", *SAE Technical Paper*, 2009. DOI: 10.4271/2009-32-0034.

[11] Pham Huu Tuyen, Pham Minh Tuan, Kazuhiro Yamamoto, and Preechar Karin, "Updating emission factors for in-use motorcycles fueled by gasoline, E5 and E10 in Vietnam", *ASEAN Engineering Journal*, Volume 11, Issue 3, pp. 199 - 206, 2021. DOI: 10.11113/aej.v11.17055.

[12] Vietnamnet, "Vietnam mandates nationwide E10 fuel from June 2026", 2025.

[13] Arinto Y.P. Wardoyo, Johan, A.E. Noor, Mohammad Hisyam Alwansyah, Eko T.P. Adi, and Arif Budianto, "The impact of additive usage on motorcycle CO and CO_2 emission", *Journal of Physics: Conference Series*, Volume 2193, 2022. DOI: 10.1088/1742-6596/2193/1/012023.

[14] Precedence Research, "Automotive catalytic converter market size and forecast 2025 to 2034", 2024.

[15] IMARC Group, "Industrial catalyst market size, share, trends and forecast by type, raw material, application, and region, 2025 - 2033", 2024.

[16] Le Minh Thang, Pham Thi Mai Phuong, Nguyen The Tien, and Isabel Van Driessche, "Mixed oxide catalytic converter on cordierite ceramic to treat exhaust gases of internal engines", Vietnam Patent No. 20257, 2018.

[17] California Air Resources Board, *"Frequently asked questions: New aftermarket catalytic converters installation requirements"*, 2009.

[18] Insight, *"Emissions regulations impact motorcycles"*, 2019.

PETROVIETNAM SCIENCE, TECHNOLOGY & INNOVATION PETROVIETNAM

ASSESSMENT OF THE GREENHOUSE GAS AND SULFUR DIOXIDE EMISSION REDUCTIONS RESULTING FROM THE TRANSITION OF GASOLINE AND DIESEL IN VIETNAM

Van Dinh Son Tho[1], Nguyen Ngoc Tu[2, 3]
[1]School of Chemistry and Life Science - Hanoi University of Science and Technology (HUST)
[2]ThuongMai University
[3]Vietnam National Petroleum Group (Petrolimex)
Email: tho.vandinhson@hust.edu.vn
https://doi.org/10.47800/PVSI.2025.06-09

Summary

Vietnam has committed to a national voluntary emission reduction target of 15.8% by 2030 relative to the 2014 baseline, with the goal of achieving net-zero emissions by 2050. Currently, 48 million motorbikes and 2.4 million cars are registered nationwide. Domestic market supplies gasoline and diesel in Grades II, III and V, which differ in their sulfur content. In 2023, total gasoline and diesel consumption reached 15.8 million tons, resulting in the emission of 50 million tons of GHG and 9,800 tons of SO_2. In response, the government issued Decision No. 876/QĐ-TTg to gradually transition the transport sector toward cleaner, greener fuels or electricity, targeting Vietnam's net-zero by 2050. In this paper, the 2030 scenario, which involves switching to ethanol fuel and transitioning gasoline engines to electric vehicles, will be considered and discussed as a strategy to reduce both GHG and SO_2 emissions. The results will be compared to the commitment of the Government.

Key words: Petroleum fuel, gasoline, diesel, ethanol, greenhouse gas, GHG, SO_2 emission, electric vehicles.

1. Introduction

Vietnam, as a developing country, has a high energy demand driven by electricity generation, industrial activities, and transportation. According to the Ministry of Natural Resources and Environment (MONRE), the country's greenhouse gas (GHG) emissions reached 371 million tons of CO_2 equivalent in 2016, with the transport sector accounting for 35.8 million tons [1]. In its efforts to reduce GHG emissions, Vietnam updated its Nationally Determined Contribution (NDC) to the United Nations Framework Convention on Climate Change (UNFCCC) in September 2022, committing to a 15.8% overall emission reduction by 2030. Specifically, the energy sector is assigned a reduction target of 7%, equivalent to 64.8 million tons of CO_2 equivalent [2]. Oh J.Y predicts that road transport alone could emit up to 71.7 million tons of GHG by 2030 [3].To address these challenges, the Government enacted Decision No. 876/QĐ-TTg on Approving the Action Program on Green Energy Transition, Reduction of Carbon and Methane Emissions in the Transport Sector. This program aims for net-zero emissions in transport sector by encouraging the use of electric vehicles (EVs), requiring all road vehicles to use E5 fuel from 2022 to 2030, and accelerating the shift toward public transportation powered by electricity or compressed natural gas (CNG) in urban areas.

In Vietnam, the transport sector remains heavily reliant on gasoline and diesel. To ensure petroleum fuel quality, the national standard QCVN 01:2022/BKHCN was issued to define quality specifications for gasoline, including RON92/95 Grades II, III, and V, as well as for ethanol-blended fuels such as E5 and E10. It also regulates the quality of diesel (DO Grades II, III, and V), including biodiesel blends (e.g., B5 and B10). The sulfur content in Vietnam's petroleum fuels is comparable to that of EURO standards.

Currently, Binh Son and Nghi Son refineries supply petroleum fuels to the domestic market. Binh Son refinery, operating since 2009, has a capacity of 150,000

Date of receipt: 11/3/2025
Date of review and editing: 11/3 - 25/4/2025
Date of approval: 25/4/2025

barrels/day (6.5 MTPA). Binh Son's gasoline and diesel products comply with Grade II criteria of the QCVN 01:2022/BKHCN. Capacity expansion to 171,000 barrels/day and product upgrading to meet Grade V standards under QCVN 01:2022/BKHCN are underway and expected to be completed by the first quarter of 2028. Nghi Son refinery began operations in 2018 with a capacity of 200,000 barrels/day (8.4 MTPA). According to the product specifications, the sulfur content of gasoline and diesel might be controlled at 50 ppm, which is higher than the requirement for Grade V fuel under the QCVN 01:2022/BKHCN standards.

The distribution of petroleum fuels in Vietnam involves both state-owned and private companies. Three major state-owned companies, including Vietnam National Petroleum Group (Petrolimex - PLX), Petrovietnam Oil Corporation (PVOIL), and Military Petrochemical JSC (Mipec), dominate the retail market. These companies actively import fuels from domestic refineries and international sources to meet local market demand.

To mitigate emissions in the road transport sector, Decision No. 49/2011/QĐ-TTg mandates that all manufactured, assembled, and imported vehicles must comply with Euro 5 emission standards as of January 1, 2022. However, Circular No. 16/2022/TT-BKHCN allows the continued utilization of gasoline and diesel fuels that comply with Grade II, III, and IV criteria until 2024. Variations in fuel quality directly impact emissions such as GHG as well as air pollutants like SO_2. This report focuses on quantifying the GHG and SO_2 emissions from the transport sector in recent years and estimating the emission levels for 2030.

According to Wang B. research, if Vietnam deploys 4,490,000 EVs by 2030 pursuant to Decision No. 876/QĐ-TTg, it will reduce GHG emissions by 5.3 million tons, equivalent to a 9% reduction compared to the NDC target for the energy sector [4]. In our view, the most effective approach to reduce emissions is the utilization of biofuels and the transition of gasoline to electric power. Using biofuels is the most convenient solution, as it does not require changing the infrastructure for petroleum fuel distribution. The transition from gasoline engines to electric ones is also a practical solution, particularly for personal motorbikes and cars. Motorbikes, in particular, require minimal charging infrastructure modifications. However, for electric cars, it is essential to develop a robust charging network, such as the one currently being expanded by VinFast.

The objective of this study is to analyze two scenarios: (1) the nationwide adoption of E5 biofuel pursuant to Decision No. 876/QĐ-TTg, and (2) the transition from gasoline vehicles to EVs. The projected GHG reductions for these scenarios are calculated and evaluated against Vietnam's commitments to national climate goals.

2. Methodology

A realistic approach for quantifying GHG emissions is based on national petroleum consumption. This article estimates national petroleum consumption and calculates the corresponding GHG emissions. Additionally, it predicts emissions for the transport sector under different scenarios for 2030. Non-transportation engines also use gasoline and diesel, but their consumption is much lower than that of the transport sector, so their contribution to total emissions is considered negligible. Petroleum consumption data and market share ratios were gathered through interviews with local companies. Additionally, petroleum quality standards were reviewed based on existing literature.

Decision No. 2826/QĐ-BTNMT, issued on October 25, 2022, establishes emission factors for GHG inventories and sets regulatory norms for CO_2, NOx, and CH_4 emissions in the transport sector. CO_2 emissions from road vehicles, railways, and water transport are nearly identical, with only slight variations in NOx emissions. Given that road transportation accounts for the largest share of traffic, its emission norms are used as the basis for calculations. Since the Decision does not specify emission factors for ethanol fuel, data from the Asian Development Bank is referenced [5]. Additionally, due to the sulfur content in petroleum fuels, combustion releases not only GHGs but also sulfur dioxide (SO_2) pollutants. SO_2 emissions are estimated based on the sulfur content in the fuel. For blended fuels, which combine mineral fuels and biofuels, GHG and SO_2 emissions are calculated using a ratio-based method.

3. Results and discussion

3.1. Petroleum fuel consumption in Vietnam

In Vietnam, local distributors purchase petroleum fuels both domestically and internationally to supply the domestic market. According to annual reports, PLX and PVOIL hold 47% and 26% of the retail market share, respectively [6, 7]. PLX supplies three types of gasoline: E5 (5% ethanol blended with RON92-II), RON95-III, and RON95-V, along with two types of diesel: DO-II and DO-V.

Table 1 summarizes the typical properties of its gasoline and diesel products, which comply with TCCS 03:2023/PLX. The results indicate that the three RON gasoline types have similar specific gravity but differ in octane number and sulfur content. Specifically, RON92/95-II contains 500 mg/kg of sulfur, RON92/95-III has 150 mg/kg, and RON92/95-V has 10 mg/kg. Similarly, DO-II has a sulfur content of 500 mg/kg, while DO-V contains only 10 mg/kg. Other fuel distributors, such as PVOIL and Mipec, also supply gasoline and diesel with the same sulfur content, ensuring compliance with the QCVN 01:2022/BKHCN petroleum fuel standards.

Decision No. 2626/QĐ-BTNMT establishes GHG emission norms for fossil fuel combustion. Based on the fuel's heating value and specific gravity, GHG emissions per ton of fuel can be calculated. The result shows that gasoline and diesel emit 3.11 tons CO_2eq/ton and 3.28 tons CO_2eq/ton, respectively (Table 1). These figures are approximately in line with data from the Asian Development Bank [5]. However, Decision No. 2626/QĐ-BTNMT does not specify GHG emission norms for biofuels. To quantify emissions from E5 fuel, ADB's GHG emission norms were used, which estimate 1.93 tons CO_2eq/ton for E100.

In addition to GHG emissions, SO_2 emissions vary depending on fuel quality. The combustion of Grade II and Grade III gasoline or diesel releases approximately 1 kg SO_2/ton and 0.3 kg SO_2/ton, respectively. In contrast, using Grade V gasoline or diesel significantly reduces SO_2 emissions to just 0.02 kg SO_2/ton, a 50-fold decrease compared to Grade II. These results highlight the environmental benefits of using higher-quality fuels.

Based on the gasoline and diesel volumes of PLX and PVOIL from 2021 to 2023 and their respective market shares, the country's total gasoline and diesel consumption can be estimated, as shown in Figure 1. During this period, gasoline consumption increased from 5.5 million tons in 2021 to 8.3 million tons in 2023 and diesel consumption rose

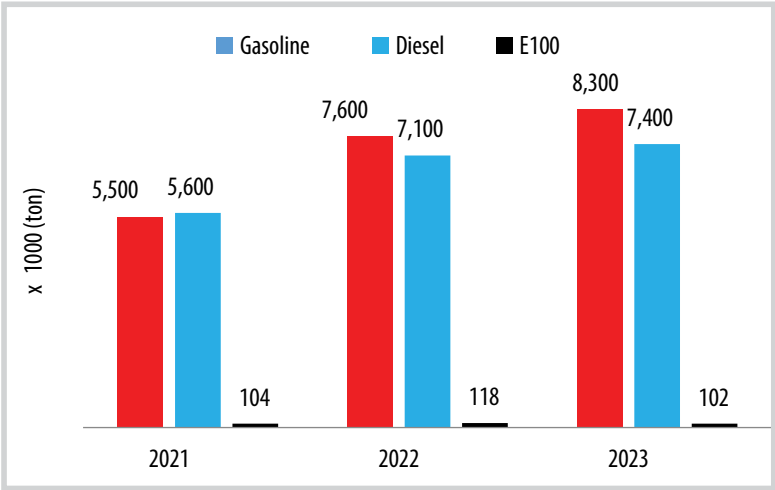

Figure 1. *Sales volume of gasoline, diesel, and ethanol in 2021, 2022, and 2023.*

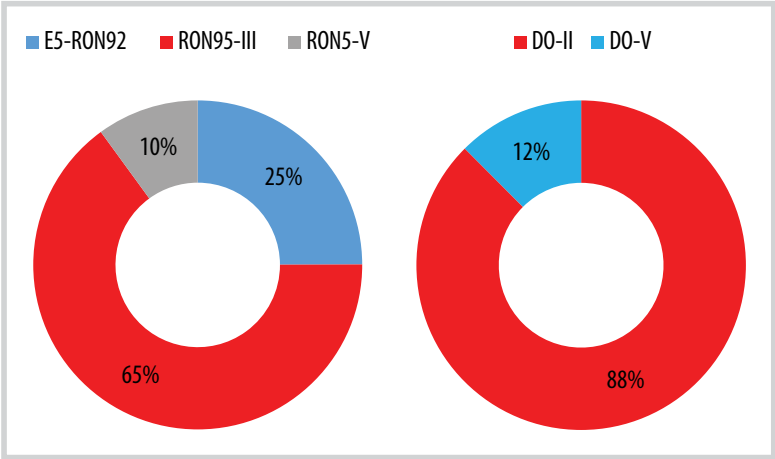

Figure 2. *Proportion of gasoline and diesel quality grades in 2023.*

Table 1. *Quality specification of gasoline and diesel and their emission factor*

Fuel	Specific gravity 15°C (kg/m³)	Sulfur content (mg/kg)	GHG (ton CO_2eq/ton)	SO_2 emission (kg/ton)
Fossil fuel TCCS 03:2023/PLX				
RON92/95-II	730	500	3.11	1.0
RON92/95-III	730	150	3.11	0.3
RON92/95-V	730	10	3.11	0.02
DO-II	820 - 860	500	3.28	1.0
DO-V	Max 845	10	3.28	0.02
Biofuel [5]				
Ethanol	0.79	-	1.93	-

from 5.6 million tons to 7.4 million tons. Despite the high demand for petroleum fuels, ethanol adoption remained limited, with E100 consumption averaging approximately 100,000 tons per year during this period. Figure 2 illustrates the proportion of PLX's fuel types in 2023. RON95-III accounted for over 65% of gasoline sales, E5 contributed 25%, and RON95-V made up 10%. Meanwhile, DO-II dominated diesel sales with an 88% share, while DO-V accounted for the remaining 12%.

In general, the retail price of Grade V fuel is always higher than that of Grade III fuel. For example, on December 28, 2023, the retail prices of Zone 1 were as follows: E5 at 21,180 VND/liter, RON95-III at 22,140 VND/liter, RON95-V at 22,700 VND/liter, DO-II at 19,780 VND/liter, and DO-V at 20,760 VND/liter [8]. The price difference between RON95-III and RON95-V was 560 VND/liter, while the gap between DO-II and DO-V was 630 VND/liter. For petroleum fuel, the end-users tend to prefer competitively priced products. It suggests that RON95-III and DO-II were priced competitively, which resulted in the highest sales volume recently. Although the E5 was priced 960 VND/liter lower than RON95-III, possibly due to concerns of biofuel quality, the sales volume of E5 remained significantly lower than that of RON95-III. Despite Vietnam's efforts to promote E5 and low-sulfur fuels since 2007, sales volumes for E5 and Grade-V fuel remain relatively low.

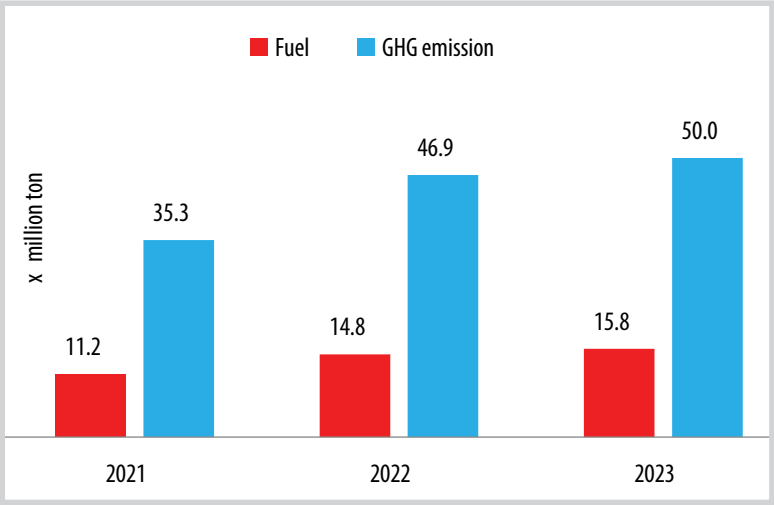

Figure 3. *Estimate petroleum fuel volume consumption and GHG emissions.*

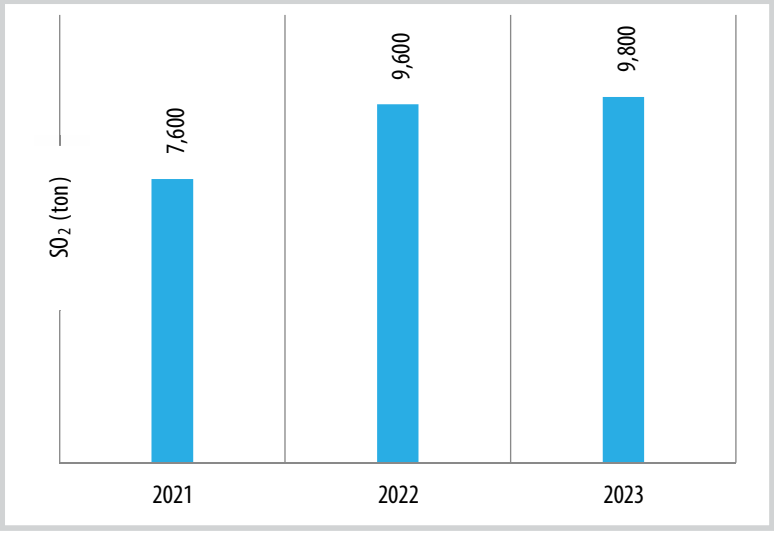

Figure 4. *SO_2 emission from petroleum fuel combustion in transportation.*

To encourage the adoption of E5, in-depth studies on consumer behavior during the shift from gasoline to E5 are essential. Identifying the psychological barriers, consumption habits, and the public's willingness to accept alternative fuels is crucial and needs further study.

By combining sales volume and GHG emission factors for petroleum and ethanol fuels, total GHG emissions were quantified, and the results are shown in Figure 3. The findings indicate that approximately 11.2 million tons of gasoline and diesel were consumed in 2021, rising to 14.8 million tons in 2022 and 15.8 million tons in 2023. Correspondingly, GHG emissions increased from 35.3 million tons in 2021 to 46.9 million tons in 2022, reaching approximately 50 million tons in 2023. Vietnam currently supplies gasoline and diesel with varying sulfur content. Based on the national fuel consumption and sulfur levels in different fuel grades, SO_2 emissions were estimated. The results reveal that approximately 7,600 tons of SO_2 were released into the atmosphere in 2021, increasing to 9,600 tons in 2022 and 9,800 tons in 2023 (Figure 4). Although Vietnam mandated that vehicle manufacturers comply with Euro 5 emissions standards starting in 2022, the local market continues to supply Grade II and Grade III fuels at lower prices than Grade V fuels. As a result, SO_2 emissions of vehicles are unlikely to meet Euro 5 targets as the Government had anticipated.

3.2. GHG and SO_2 emissions of the baseline scenario for the 2025 - 2030 period

Oh J.E. estimated that Vietnam's gasoline and diesel consumption could reach 9.33 million tons and 10.62 million tons, respectively, by 2025, and further increase to

at least 12.33 million tons of gasoline and 15.10 million tons of diesel by 2030 [3]. The Baseline scenario calculates GHG and SO_2 emissions for 2025 and 2030, assuming that the market will continue consuming three types of gasoline (E5-RON92-II, RON95-III, and RON95-V) with the same proportions as in 2023. Based on the volume of E5-RON92-II for 2025 and 2030, the volume of E100 is expected to reach approximately 128,000 tons in 2025 and increase to 170,000 tons by 2030. GHG emissions from gasoline and diesel consumption for these years were quantified. The results indicate that with a total petroleum consumption of 20 million tons in 2025, emissions could reach 63.7 million tons of CO_2eq. By 2030, fuel consumption is projected to rise to 27.4 million tons, resulting in an estimated 87.7 million tons of GHG emissions (Figure 5).

The amount of SO_2 emissions can be quantified as mentioned above, reaching 13,400 tons in 2025 and 18,700 tons in 2030. However, if the country uses the Grade V petroleum fuel according to QCVN 01:2022/BKHCN standard, the SO_2 emissions would be markedly reduced to approximately 400 tons in 2025 and 550 tons in 2030. These findings highlight that a substantial reduction in SO_2 emissions can be achieved if Grade V petroleum fuels are strictly enforced nationwide in the future.

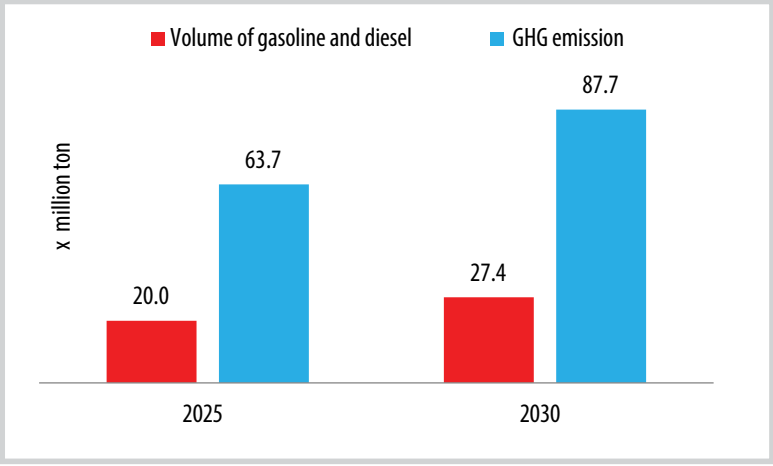

Figure 5. *Estimate petroleum consumption and GHG emissions for 2025 and 2030.*

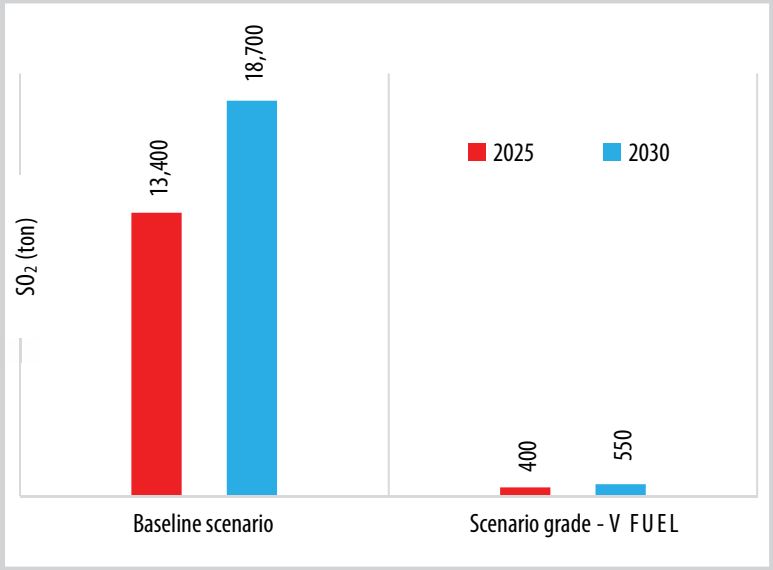

Figure 6. *Comparison of SO_2 emission in the Baseline scenario and the mandatory use of Grade-V gasoline and diesel.*

3.3. First scenario for mandatory E5

Vietnam has four ethanol plants with a total annual capacity of 280,000 tons. These plants began operation in 2012, however, due to low ethanol consumption, some were temporarily shut down. During 2021 - 2023, ethanol fuel consumption remained low at only 100,000 tons, so there is just one plant currently in operation to supply the domestic market. According to Decision No. 876/QĐ-TTg, which enforces the nationwide adoption of E5 fuel in the coming years, ethanol consumption is expected to increase (First scenario). Under this scenario, three types of ethanol-blended gasoline E5-RON92-II, E5-RON95-III, and E5-RON95-IV will be supplied to the domestic market. Ethanol consumption is projected to reach 531,000 tons in 2025 and increase to 702,000 tons by 2030. Compared to the total capacity of the four local ethanol plants, this would meet only 40% of market demand by 2030.

As mentioned above, Vietnam's gasoline and diesel consumption could reach 20 million tons and 27.4 million tons, respectively, by 2025 and 2030, and the data will be considered as Baseline scenarios for our report. Table 2 presents the GHG emissions for the Baseline and First scenarios for 2025 and 2030, focusing solely on gasoline consumption. In the Baseline scenario, the gasoline volume will be 9.33 million tons in 2025 and increase to 12.33 million tons in 2030. As a result, GHG emissions are projected to be 28.9 million tons in 2025, rising to approximately 38.1 million tons by 2030. Under the First scenario, with the increase of ethanol fuel from 531,000 tons to 702,000 tons for the period of 2025 - 2030, the GHG emissions are expected to decrease slightly to 28.4 million tons in 2025 and 37.5

Table 2. *Comparison of the Baseline and First scenario for GHG reduction in 2025 and 2030*

	2023	2025	2030
Baseline scenario			
E100 volume (thousand tons)	102	133	154
Gasoline volume (million tons)	8.3	9.33	12.33
GHG (million tons CO_2)	26.0	28.9	38.1
First scenario			
E100 volume (thousand tons)		531	702
Gasoline volume (million tons)		8.8	11.6
GHG (million tons CO_2)		28.4	37.5

million tons by 2030. This suggests that full implementation of Decision No. 876/QĐ-TTg, obligating the use of E5 fuel, could reduce GHG emissions by 500,000 tons in 2025 and 600,000 tons in 2030 compared to the Baseline scenario. Furthermore, this decision would not only contribute to GHG reduction but also provide an opportunity to reopen ethanol plants in Vietnam.

Vietnam has pledged to reduce GHG emissions by 15.8% below business-as-usual (BAU) levels by 2030, as outlined in its updated NDC-2022. The energy sector must reduce emissions of 7%, equivalent to 64.8 million tons of GHG. The transport sector accounts for 20.2% of the final energy consumption of the nation [9]. The NDC-2022 does not specify a reduction target for the transport sector, so it is assumed a reduction of 7%, corresponding to a decrease of 13 million tons of GHG by 2030. By implementing the E5 gasoline mandate policy, as proposed in the First scenario, it will only reduce 600,000 tons by 2030 and will contribute approximately 4.6% of the target.

3.4. Secondary scenario for transition from gasoline vehicles to EV

Wang B. reported promising figures for the vehicle transition in Vietnam. By 2025, electric vehicle registrations are projected to include 1,163,000 electric motorbikes (e-bikes), 60,000 electric cars (e-cars), and 470 electric buses (e-buses). By 2030, these registered numbers are expected to grow to 1,159,000 e-bikes, 297,000 e-cars, 2,440 e-buses, 10 inter-provincial passenger cars, and 2,500 electric trucks. With 4,490,000 EVs and an emission factor of 0.52 tons CO_2/MWh in 2030, it will reduce 5.3 million tons of GHG, equivalent to a 9% reduction compared to the NDC target for the energy sector and up to a 41% reduction for the transport sector [4]. These optimistic situations are based on strong policy and financial support for transition initiatives by both the public and private sectors.

According to DEA report, Vietnam had approximately 2.4 million gasoline cars and around 48.3 million motorbikes by 2022. Motorbikes accounted for 71% of gasoline consumption, while cars used 29% [10]. Based on the nation's gasoline consumption of 7.8 million tons in 2022, motorbikes consumed approximately 5.5 million tons, while car engines used around 2.3 million tons. The data indicates that motorbikes significantly contribute to GHG emissions.

The adoption of e-bikes is increasing recently, and in particular, it does not require the modification of the electric charging system, as they can be conveniently charged at home overnight. However, for e-cars, developing the necessary charging infrastructure is crucial to support market growth. Companies like VinFast are already investing and establishing the foundation for the broader adoption of EVs. Moreover, economic factors such as investment costs, government incentives, and especially access to charging infrastructure considerably influence the transition to EVs. Within the scope of this paper, we do not examine these issues. Instead, we provide a relative comparison of emissions from EV and gasoline vehicles, based on average growth rates of EVs in recent years.

Currently, the transition to cleaner public bus transportation is also progressing rapidly. According to Wang B., public transportation contributes only 1% of total transport sector emissions. The government plans to replace 1,470 of the 6,180 city buses with e-buses by 2025 (23.8%), and 2,440 of the 12,750 city buses by 2030 (19.1%) [4]. With a total of 12,750 e-buses in operation by 2030 and based on the fuel consumption of diesel buses, the power consumption of e-buses, and transport distances, our calculations show that switching from diesel to e-buses will reduce 221,000 tons of CO_2.

Diesel engines contribute substantially to GHG emissions including ships, railways, heavy-duty trucks...

Table 3. *GHG emissions of gasoline engine and EV*

	Unit	Power consumption	GHG (kg CO_2/km)	GHG Decrease rate (%)
Emission factor of grid 0.6766 kg CO_2/kWh for 2025				
Gasoline motorbike	liter/100 km	1.92	0.043	
E-bike	kWh/100 km	1.76	0.012	72.5
Gasoline car	liter/100 km	5.68	0.128	
E-car	kWh/100 km	14.20	0.096	25.0
Emission factor of grid 0.52 kg CO_2/kWh for 2030 [4]				
Gasoline motorbike	liter/100 km	1.92	0.043	
E-bike	kWh/100 km	1.76	0.009	78.9
Gasoline car	liter/100 km	5.68	0.128	
E-car	kWh/100 km	14.20	0.074	42.3

Due to the limitation of the technology and high investment costs, these transport modes have not been deployed in Vietnam. Wang B. reports the assumption that, by 2025, only 10 diesel trucks will be replaced by e-truck; by 2030, the replacement will include only 10 e-vehicles for passenger transportation and 2,500 medium-duty e-trucks [4]. Therefore, by 2030, diesel vehicles will unlikely be replaced by EVs. Based on the above assumption, we have not included e-diesel in our assessment, as their contribution to GHG reduction is negligible for 2030. Instead, the study focuses on the transition of gasoline engine scenarios.

The Second scenario considers the transition from gasoline engines to EVs for motorbikes and cars by 2030. Considering the number of vehicles registered and gasoline consumption in 2022, it is estimated that each motorbike consumes an average of 114 kg of gasoline per year, resulting in the emissison of 354 kg of CO_2 annually. In comparison, a car engine consumes an average of 958 kg of gasoline per year, emitting approximately 2,977 kg of CO_2 annually. According to the Dinh S.T. research, the fuel consumption rates are 1.92 liters per 100 km for motorbikes and 5.68 liters per 100 km for gasoline cars [11], which corresponds to an average annual travel distance of 8,200 km for each motorbike and 23,000 km for a gasoline car. Currently, the Government is encouraging the transition from gasoline vehicles to EVs to reduce emissions in urban areas. The average power consumption of EVs is shown in Table 3 [11]. According to Decision No. 2826/QĐ-BTNMT, the emission factor for the grid is 0.6766 kg CO_2/kWh. Calculations of GHG emissions for 2025 indicate that e-bikes reduce emissions by 72.5% compared to motorbikes, corresponding to a reduction of 256 kg CO_2/vehicle/year. Similarly, the substitution of gasoline cars with EVs will result in a reduction of 586 kg CO_2/vehicle/year, equivalent to a 25% decrease. For 2030, the emission factor of the grid might be 0.52 kg CO_2/kWh, resulting an increase in the reduction of GHG emissions for EVs as mentioned in Table 3.

In 2019, approximately 163,000 e-bikes were registered, and in 2020 increased to 273,000 e-bikes, representing a growth rate of 8.54% [12]. It is forecasted that 240,000 e-bikes will be registered by 2025, contributing to a reduction of 61,540 tons of GHG emissions that year. In recent years, the adoption of e-cars has accelerated, with 8,364 vehicles registered in 2022 and 15,700 vehicles in 2023. It is anticipated that the number of e-cars will grow by 25.8% during 2023 - 2032 [14], reaching approximately 33,000 registered EVs by 2025. Each e-car is expected to reduce emissions by 586 kg of CO_2 annually compared to a gasoline car. With the transition of 33,000 e-cars, it will reduce approximately 24,540 tons of GHG emissions in 2025. With the total number of EVs that might reach approximately 2.9 million e-bikes and 87,000 e-cars by 2025, the estimated GHG reduction will be 808,000 tons.

For the Second scenario of the transition from gasoline engine to EV, with an e-bike growth rate of 8.54% and an e-car growth rate of 25.8%, it is estimated that by 2030, there will be 290,000 registered e-bikes and 55,000 registered e-cars. A total of 4.3 million e-bikes and 320,000 e-cars might be put in operation by 2030 and combined with the lower emissions of the grid, the GHG emissions are expected to be reduced by approximately 1.6 million tons, contributing around 12.3% of the NDC's commitment for the transport sector.

4. Conclusion

Vietnam has committed to reducing GHG emissions by 15.8% by 2030 with the transport sector expected to cut approximately 13 million tons of GHG. Vietnam uses various fuel types, including gasoline and diesel of

different quality grades. By 2025, the country is expected to consume 20 million tons of gasoline and diesel, resulting in emissions of 63.7 million tons of GHG and 13,400 tons of SO_2. Looking ahead to 2030, if the entire nation adopts grade-V fuels, total fuel consumption is expected to reach 27.4 million tons, leading to GHG emissions of 87.7 million tons and SO_2 emissions of 550 tons.

Currently, green solutions for transportation, including the transition to EVs, the use of biofuels, and CNG, are being implemented. If the E5 policy is implemented (First scenario), ethanol consumption is projected to reach about 700,000 tons by 2030, contributing to a reduction of 600,000 tons of GHG emissions in comparison to the Basic scenario. With the Second scenario of the transition of gasoline vehicles to EVs, it is expected that 4.3 million e-bikes and 320,000 e-cars will be in operation by 2030, leading to a reduction of 1.6 million tons of GHG emissions. By combining the E5 policy with the EV transition pathway, total GHG emissions could be reduced by 2.2 million tons, equivalent to a 16.9% reduction compared to the NDC commitment for the transport sector by 2030. This indicates that additional solutions are required to achieve a reduction target of 13 million tons of GHG emissions, equivalent to replacing approximately 4 million tons of gasoline and diesel with cleaner fuel.

To promote the use of E5 or the transition of gasoline engines to EVs, it is essential to conduct in-depth research on consumer behavior, economic factors, and the accessibility of charging infrastructure. A systematic study of these factors is necessary to provide more accurate forecasts of the shift from gasoline vehicles to EVs in the Vietnamese market.

References

[1] Ministry of Natural Resources and Environment, *Report on National GHG inventory for 2016*, 2020.

[2] Vietnam, *Nationally determined contribution (NDC)*, 2022.

[3] Jung Eun Oh, Maria Cordeiro, John Allen Rogers, Khanh Nguyen, Daniel Bongardt, Ly Tuyet Dang, and Vu Anh Tuan, "Addressing climate change in transport: Volume 1: Pathway to low-carbon transport", 2019.

[4] Tarek Keskes, Chiara Odetta Rogate, Zayra Romo, Shigeyuki Sakaki, and Bowen Wang, "Viet Nam - Recommendations to the national roadmap and action plan for the electric-mobility transition: Executive Version (English)". [Online]. Available: https://documents.worldbank.org/en/publication/documents-reports/documentdetail/099102224045529146.

[5] ADB, "Guidelines for estimating greenhouse gas emissions of Asian development bank projects: Additional guidance for transport projects", 2016. [Online]. Available: https://www.adb.org/sites/default/files/institutional-document/219791/guidelines-estimating-ghg-emissions-transport.pdf.

[6] Petrolimex, *Báo cáo phát triển bền vững*, 2023.

[7] PVOIL, *Báo cáo thường niên*, 2020 - 2022.

[8] Ministry of Industry and Trade of the Socialist Republic of Vietnam, Information on fuel price management. [Online]. Available: https://moit.gov.vn/tin-tuc/thong-bao/thong-tin-dieu-hanh-gia-xang-dau-ngay-28-12-2023.html.

[9] IEA, "Where does Vietnam get its energy?". [Online]. Available: https://www.iea.org/countries/viet-nam/energy-mix.

[10] Danish Energy Agency, "Viet Nam energy outlook report: Pathways to net-zero", 2024. [Online]. Available: https://ens.dk/sites/ens.dk/files/Globalcooperation/1._eor-nz_english_june2024_0.pdf.

[11] Dinh-Son Tran, Huong Le, and Zifei Yang, "Two-wheelers in Vietnam: A baseline analysis of fleet characteristics and fuel consumption in 2019 and 2020", 2022. [Online]. Available:https://theicct.org/publication/2w-lvs-vietnam-asia-baseline-feb22/.

[12] Huong Le, Francisco Posada, and Zifei Yang, "Assessment of electric two-wheelers development in Vietnam: An overview", 2022. [Online]. Available: https://theicct.org/wp-content/uploads/2022/10/asia-pacific-lvs-NDC-TIA-E2W-mkt-growth-Vietnam-nov22.pdf.

[13] Dinh Van Hiep, Nam Hoai Tran, Nguyen Anh Tuan, Tran Manh Hung, Ngo Viet Duc, and Hoang Tung, "Assessment of electric two-wheelers development in establishing a national E-mobility roadmap to promote sustainable transport in Vietnam", *Sustainability*, Volume 15, Issue 9, 2023. DOI: 10.3390/su15097411.

[14] BMI, "Vietnam EV profile: VinFast to provide a strong boost to BEV sales", 2023. [Online]. Available: https://www.fitchsolutions.com/bmi/autos/vietnam-ev-profile-vinfast-provide-strong-boost-bev-sales-03-08-2023.

SELECTIVE CATALYTIC REDUCTION (SCR) TECHNOLOGY USING DEF SOLUTION REDUCES NO_x EMISSIONS FROM DIESEL ENGINES

Selective catalytic reduction (SCR) technology is being recognized as the most effective solution for mitigating nitrogen oxide (NO_x) emissions from diesel engines. The SCR system uses diesel exhaust fluid (DEF) to facilitate the conversion of up to 90% of NO_x into benign nitrogen and water vapor, enabling engines to maintain optimal operating performance while reducing fuel consumption.

Diesel fuel remains a fundamental energy source in transportation and industrial sectors due to its performance advantages and cost-effectiveness. However, diesel is also a major source of NOx emissions, which have a severe impact on air quality. To resolve this issue, Diesel Exhaust Fluid (DEF) has become the standard solution in countries with stringent emission regulations, including the European Union, the United States, and Japan…

DEF is manufactured from high-purity urea in accordance with ISO 22241 standards, consisting of 32.5% urea and 67.5% demineralized water, creating an odorless, non-corrosive, and non-toxic solution. When injected into the exhaust treatment system, DEF decomposes to produce ammonia (NH_3), which reacts within the SCR catalyst to convert up to 90% of NOx into nitrogen and water vapor, helping engines maintain optimal operating performance and reduce fuel consumption.

The DEF market is entering a period of strong global growth. Precedence Research forecasts that the global DEF market size could reach USD 84.92 billion by 2034, corresponding to a stable Compound Annual Growth Rate (CAGR) of 7.93% over the 2025 - 2034 period [1]. Another study indicates that the DEF market size could reach approximately USD 61.56 billion by 2030, with a CAGR of 7.9% during the 2024 - 2030 period [2]. These forecasts, while differing in time scope, both reflect the overall trend that the DEF market will continue to experience stable growth over the next decade, driven by the increasing number of vehicles using SCR technology, countries tightening emission standards, and the demand for enhanced operating performance of diesel engines in transportation and industrial applications.

Globally, increasingly stringent environmental regulations are becoming the primary driver of demand for DEF. The implementation of Euro 6 standards in Europe and EPA Tier 4 standards in the United States has led to widespread adoption of SCR technology to meet strict NOx emission regulations for automotive manufacturers. Additionally, DEF is also widely used in construction equipment (heavy machinery) and the agricultural sector (farming equipment) to achieve sustainable agricultural development goals...

The Asia-Pacific region, particularly Southeast Asia, is recognized as the fastest-growing DEF market. Market research organizations forecast that the global DEF market size will continue to expand with a Compound Annual Growth Rate (CAGR) ranging from 4.5% to 11.8%, depending on the application segment and region.

Currently, Artificial intelligence (AI) and machine learning (ML) algorithms are being researched for application in optimizing DEF consumption and enhancing exhaust treatment system performance. AI models are capable of analyzing real-time operational data to adjust DEF injection quantities, thereby maintaining optimal NOx reduction efficiency and reducing fuel consumption. Automation technology is being deployed in DEF production and distribution, contributing to reduced operating costs, improved quality, and enhanced supply capacity. The integration of AI and automation solutions into the DEF value chain is expected to optimize fuel consumption and improve emission control efficiency in the long term.

In Vietnam, the roadmap for the implementation of vehicular emission control standards is being progressively enforced. Since January 1, 2022, all newly manufactured and imported automobiles must meet Euro 5 emission standards. Vehicles manufactured from 2017 onwards will be required to comply with Euro 4 emission standards from January 1, 2026. Consequently, the adoption of technical support solutions, particularly SCR systems combined with DEF solution, enables diesel-powered vehicles to comply with current emission regulations, optimize operating performance, extend engine lifespan, and align with Vietnam's strategic orientation toward green and sustainable transportation development.

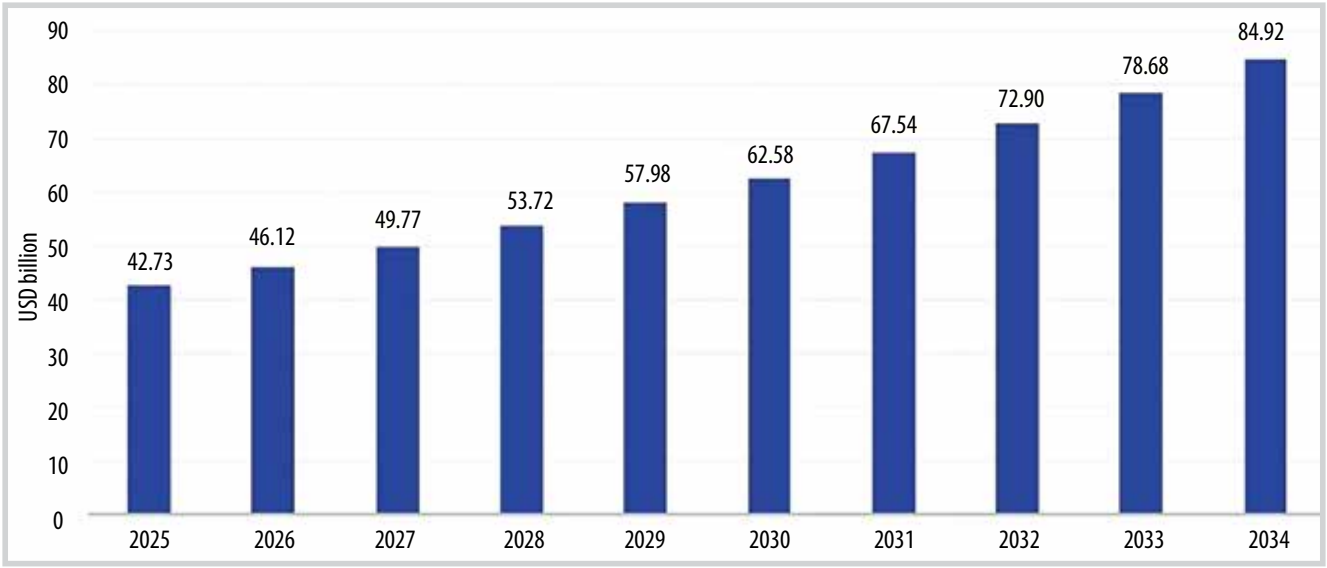

Figure 1. *Diesel exhaust fluid market size 2025 to 2034 [1].*

To achieve sustainable development goals and leverage advantages from raw materials and technology at the Phu My Fertilizer Plant, Vietnam National Industry - Energy Group (Petrovietnam)/ Petrovietnam Fertilizer and Chemicals Corporation (PVFCCo) has researched and produced DEF - Phu My green, meeting international standards with a composition of 32.5% urea and 67.5% purified distilled water.

After exhaust gases pass through the Diesel Particulate Filter (DPF), DEF - Phu My green is injected and mixed into the exhaust stream through a precision dosing control system as it enters the SCR catalytic converter. Here, ammonia in the urea reacts with NOx in the exhaust stream, neutralizing them into benign nitrogen (N_2) and water vapor (H_2O) that exit through the exhaust pipe. The SCR system, when combined with exhaust treatment fluid, can reduce NOx by up to 90%. DEF does not cause clogging in the injection system nor affect the catalyst layer of the SCR exhaust treatment system.

Independent testing results show that DEF - Phu My green is a high-purity deionized urea solution for diesel engine exhaust treatment through the SCR system, helping to reduce pollutant emissions into the environment. All impurity indicators are many times lower than permissible limits, thereby protect the SCR catalyst system and maintain maximum treatment efficiency.

Every single batch is tested in PVFCCo's laboratory to ensure consistent quality and compliance with the stringent ISO 22241 standard on purity and composition. DEF product has also achieved international quality certification from SGS for its quality and reliability. In addition to DEF - Phu My green 32.5% product, PVFCCo can supply DEF - Phu My green 40% for marine applications, with a maximum annual production capacity of 40,000 tons.

PVFCCo continues to maintain its position as Vietnam's leading fertilizer producer while accelerating expansion into basic chemicals manufacturing. The company is proactively preparing the necessary capabilities and resources to enter the petrochemicals, gas-based chemicals, and green chemicals when opportunities arise. PVFCCo targets revenue of at least USD 1 billion by 2030, with chemicals accounting for over 35% of total revenue and an average annual revenue growth rate of 10%. In particular, PVFCCo is intensifying its production of green chemicals, thereby supporting the achievement of its greenhouse-gas emissions reduction targets.

Vu Thu Tra

References

[1] Precedence Research, "Diesel exhaust fluid market size and forecast 2025 to 2034", 2025. [Online]. Available: https://www.precedenceresearch.com/diesel-exhaust-fluid-market.

[2] Brandon Ward, "Diesel exhaust fluid market expected to reach $61.56 billion by 2030, 2025. [Online]. Available: https://www.fuellogic.net/diesel-exhaust-fluid-market-growth-forecast-2030/.

GLOBAL OIL & GAS OUTLOOK FOR 2026

Major international organization assessments indicate that 2026 will be a year in which the oil and gas sector faces sustained low prices while accelerating new business models and digital transformation. Rystad Energy forecasts that digital initiatives could save the industry over USD 320 billion and will continue to reshape the oilfield services landscape. Wood Mackenzie observes that companies will tighten capital discipline, prioritize high-return projects, and expand the use of AI to improve efficiency as investment in low-carbon businesses declines. Reports from the IEA and EIA indicate persistent oversupply and rising inventories, suggesting that oil prices are likely to remain low throughout 2026. However, demand growth in non OECD markets and strategic M&A activity may drive significant structural shifts in the global oil and gas industry.

Rystad Energy's research highlights digital innovation as an increasingly defining force in the oilfield services (OFS) sector as it responds to evolving market conditions, creating opportunities for steady, long-term growth. Rystad Energy predicts that over the next 5 years, the oil and gas industry could save more than USD 320 billion by further digitalizing operations in 5 key areas: drilling optimization, autonomous robotics, predictive maintenance, reservoir management, and logistics optimization (Figure 1) [1]. Rystad Energy further notes that the OFS business ecosystem is expected to undergo a significant transformation as continued merger and acquisition (M&A) activity, new business partnerships with technology firms, and greater software integration drive digital-first business strategies for key OFS players.

Rystad Energy's analysis indicates that the importance of digitalization, while still unstandardized and sometimes difficult to measure, is increasingly reflected in financial disclosures. Most supply-chain players do not yet break out standalone, generally accepted accounting principles (GAAP)-level "digital profit" in the same way a pure software-as-a-service company would. Nevertheless, this is gradually changing,

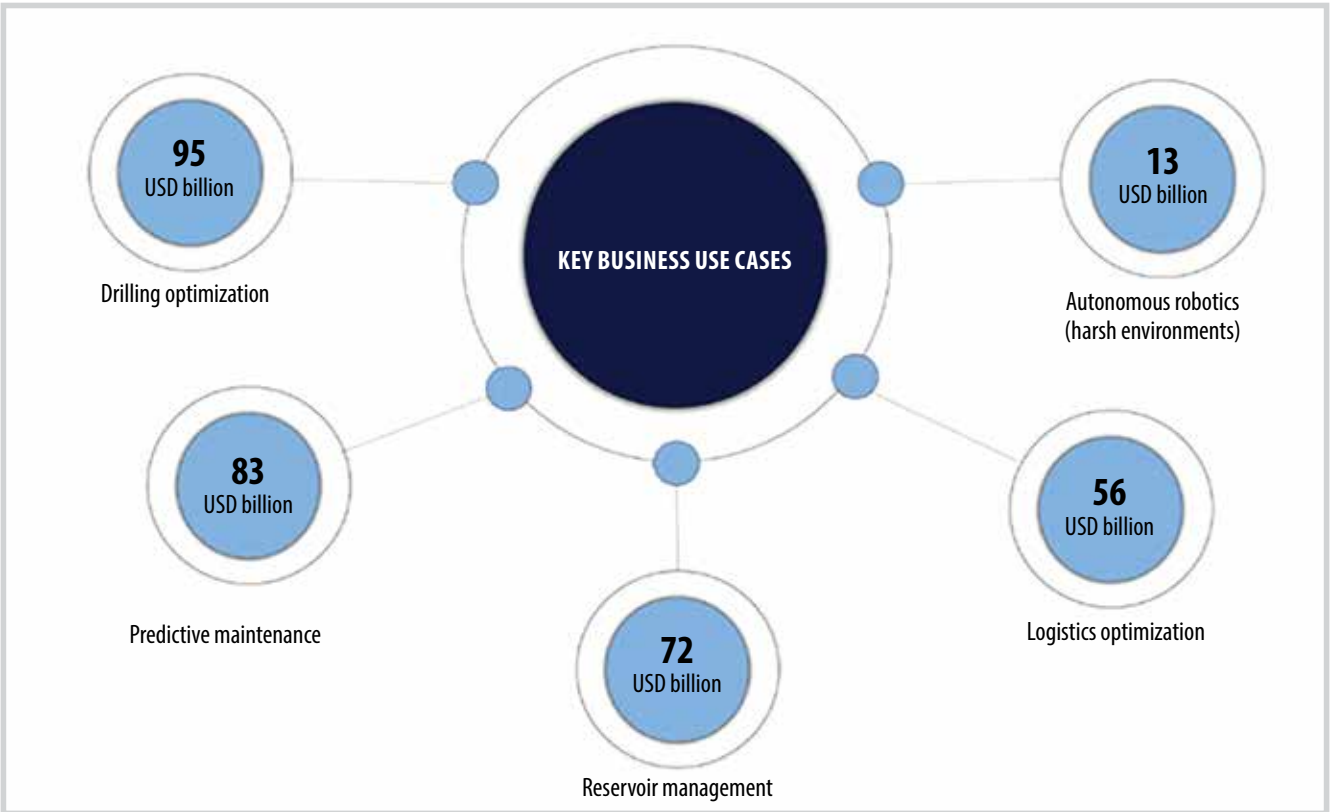

Figure 1. *Key digitalization use cases in oil and gas, expected savings through 2030 [1].*

with Schlumberger now reporting a digital division in its earnings and projecting that the division's margin will reach 35% on a full-year basis in 2025. A similar trend can be observed at Viridien, a global technology and geoscience company, whose digital, data and environment (DDE) segment generated USD 787 million in revenue last year, representing 17% growth and delivering adjusted earnings before interest, taxes, depreciation and amortization (EBITDA) of USD 458 million. Digital revenue streams offer more stable, resilient growth trajectories that are less exposed to the volatility of upstream capex.

Rystad Energy observes that the investment community is increasingly valuing energy-technology narratives, with service companies that clearly articulate technology-driven and recurring-revenue strategies often commanding higher valuation multiples than those tied solely to equipment cycles. As noted by Binny Bagga, Senior Vice President of supply chain at Rystad Energy, a strong emphasis on digitalization represents a direct pathway to creating lasting shareholder value

At the same time, the widespread deployment of digital oilfield solutions continues to face notable barriers, including substantial upfront costs for hardware and software, ongoing maintenance costs, and cybersecurity. These hurdles are especially acute for smaller firms or those operating with legacy infrastructure, complicating the justification of such investments amid economic uncertainty. To mitigate these challenges, mid-tier companies are selectively enhancing their offerings with targeted digital capabilities, while smaller niche players and specialized software vendors focus on delivering modular, custom solutions.

Rystad Energy further highlights a clear acceleration in digital investment through partnerships with technology firms, complementing internal capability building and acquisitions in the digital space. The overall intensity and frequency of these partnerships have increased sharply, especially since 2021, with the most significant uptick observed in the past 2 years among leading companies such as Schlumberger, Halliburton, NOV and Baker Hughes, underscoring a broader industry shift toward digital transformation, with large suppliers actively accelerating their collaborations with technology partners in recent years.

According to Wood Mackenzie [2], oil and gas companies face an even tougher strategic balancing act in 2026 than in 2025, as lower oil prices will force more structural cost reductions and cuts to share buyback programs. The firm projects that companies will continue to shift investment from low-carbon initiatives towards upstream operations while broadening their resource capture strategies.

Wood Mackenzie assesses that companies will allocate capital even more rigorously to their best-returning projects in 2026. This strategic shift will

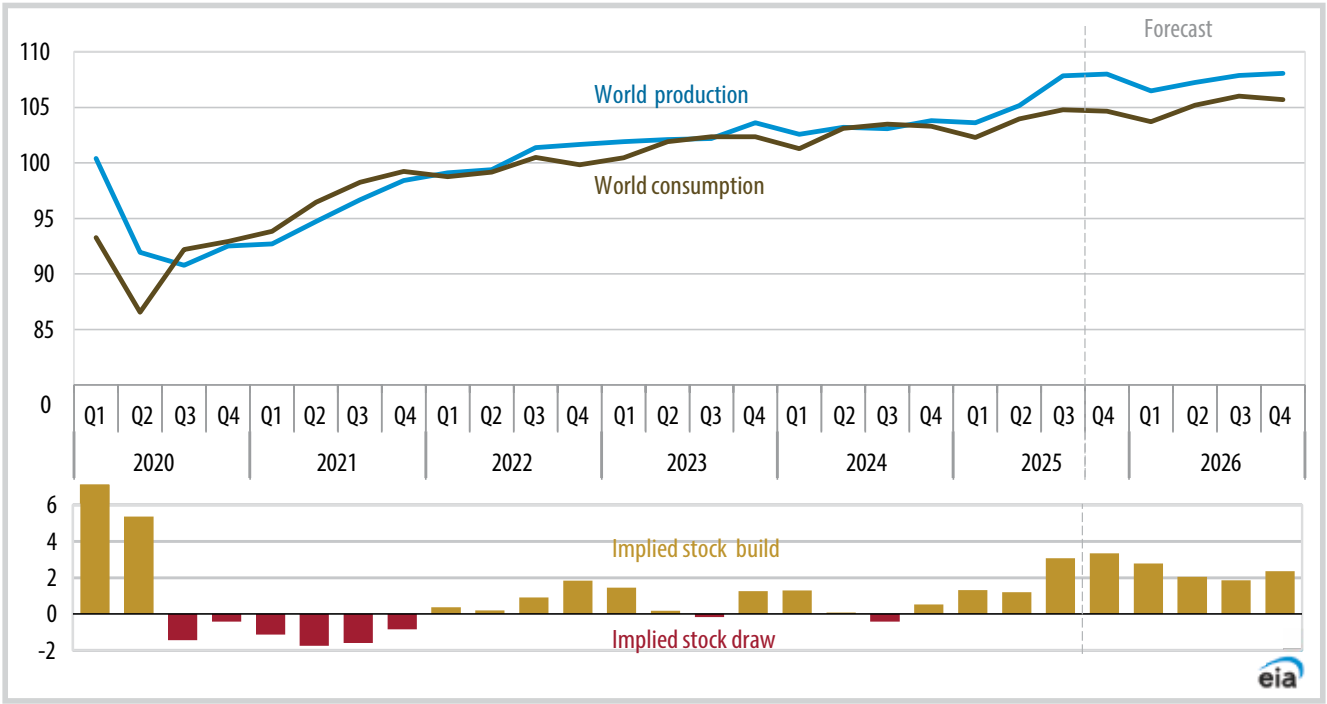

Figure 2. *Global liquid fuels production and consumption balance [4].*

result in modest year-on-year declines in investment across the industry, further reductions in low-carbon guidance as companies prioritize immediate returns. Reinvestment rates average around 55% of operating cash flow, though Wood Mackenzie notes that some players will outspend their operating cash flow to maintain strategic initiatives.

Wood Mackenzie forecasts that the largest players will lead the industry up the AI adoption curve. The majors will be at the forefront of identifying where AI and digitalisation can cut costs, increase productivity, and drive efficiency. National oil companies (NOCs) can extract major operational efficiencies from two unique structural advantages: Their massive scale of operations within single geographic regions and their integrated, single-country operations spanning the entire value chain. These characteristics could give NOCs a competitive edge in deploying AI at scale.

According to Wood Mackenzie's analysis, production growth exceeding 3% and margin expansion will mitigate the impact of lower prices. The majors are increasingly divided on their ability to sustain oil and gas production into the next decade. ExxonMobil and BP possess more post-2030 project options in their portfolios. The other majors face mounting pressure to accelerate upstream portfolio renewal.

Wood Mackenzie observes that the peer group is primed for counter-cyclical M&A, but is unlikely to find distressed opportunities under its price forecasts. Key themes will include boosting free cash flow and returns, share buybacks even below USD 60 per barrel (led by Shell and the US majors), and acreage reloading (all players). Wood Mackenzie forecasts that the majors will broaden resource capture strategies. US gas could emerge as an M&A hotspot even if prices do not fall. Some players will increase exploration budgets, with Wood Mackenzie specifically identifying Chevron as likely to boost spending to address previous under-investment. A rebound in discovered resource opportunities as companies accelerate portfolio rebuilding for the next decade. Wood Mackenzie assesses that the majors will expand geographically into resource-rich regions, including the Middle East, North Africa and the Atlantic Margin, reversing the recent trend of portfolio shrinkage.

Wood Mackenzie's analysis identifies a bifurcation emerging among oil-focused US independent producers. Devon Energy and ConocoPhillips will continue to deliver production growth in the Permian basin. However, Wood Mackenzie notes that concerns around the depth of top-tier well inventory will force companies to emphasize operational efficiency and continue reducing unnecessary development spending. The prioritization of shareholder distributions and returns will result in most players delivering flattish production. Plateauing tight oil production will push some E&Ps to

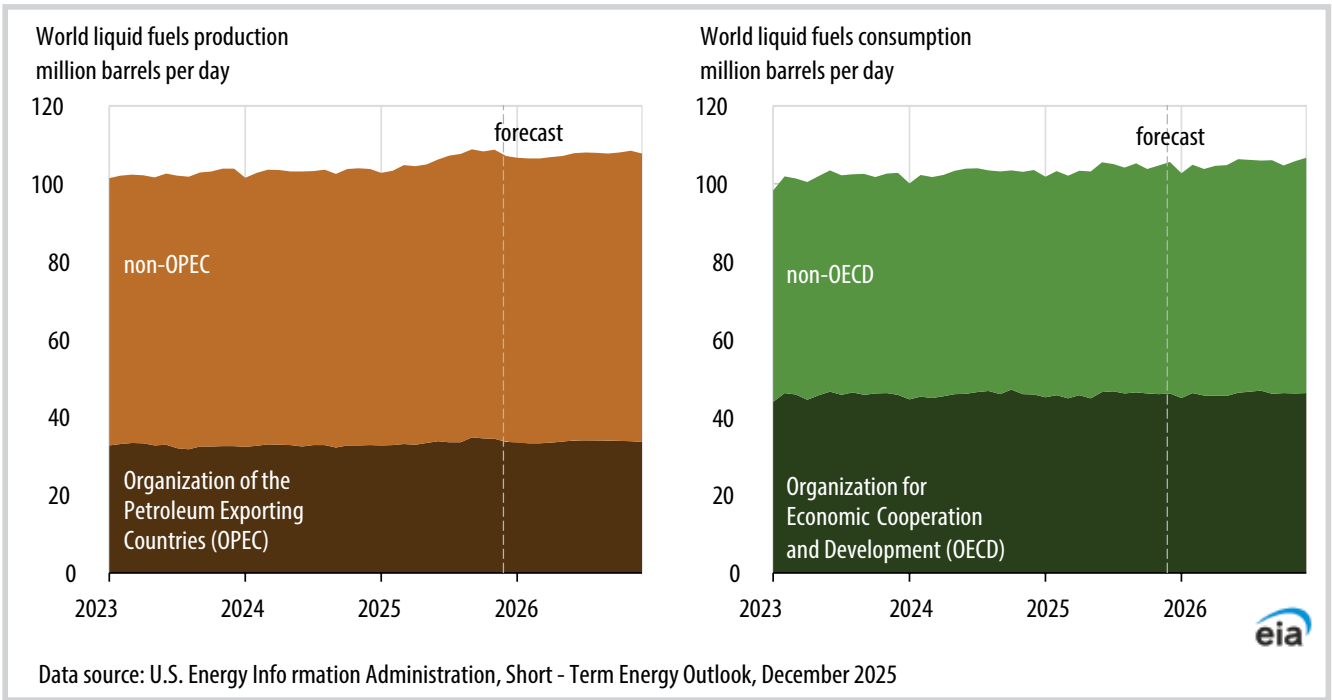

Figure 3. *World liquid fuels production and consumption [4].*

add international shale opportunities to support longer-term growth (EOG, Continental). Wood Mackenzie anticipates consolidation as companies seek to build scale and resilience. Repsol may pursue a reverse merger, most likely targeting a US player to gain a US-listing and scale-up. Harbour and Ithaca may also diversify to address production declines, having been linked to onshore and offshore US acquisitions. Companies with advantaged portfolios will attract interest from larger players, though the weakest E&P companies will face the most pressure to seek combinations.

According to the International Energy Agency's latest oil market report [3], global oil demand is set to rise by 830 thousand barrels per day in 2025 amid an improving macroeconomic and trade outlook. The IEA notes that these brighter prospects extend to its 2026 forecast, which the agency has upgraded by 90 thousand barrels per day, to 860 thousand barrels per day year-on-year. Gasoil and jet/kerosene account for half of 2025's gains, with fuel oil losing ground to natural gas and solar in power generation. In 2026, petrochemical feedstocks will dominate growth, with their share rising to more than 60% from 40% in 2025.

On the supply side, IEA reports that global oil supply fell by 610 thousand barrels per day in November, extending the decline from September's record of 109 million barrels per day to 1.5 million barrels per day. Global oil supply growth has been cut by 100 thousand barrels per day to 3 million barrels per day for 2025 and by 20 thousand barrels per day for 2026 to 2.4 million barrels per day, to 106.2 million barrels per day and 108.6 million barrels per day, respectively.

The IEA observes that, after weathering significant unplanned refinery outages in November, tightness in refined product markets has eased, but sanctions in the first quarter of 2026 will provide fresh challenges. The agency has increased its refinery run forecasts for 2026 to 84.4 million barrels per day, raising expected growth to 750 thousand barrels per day.

Regarding inventories, IEA reports that global observed inventories rose to four-year highs in October, at 8,030 million barrels. Stock builds averaged 1.2 million barrels per day during the first 10 months of the year, with October recording a 42 million barrels build (+1.4 million barrels per day), led by higher oil on water (+83 million barrels), while on-land stocks declined by 41 million barrels, led by a 26 million barrels contraction in OECD countries. Preliminary data for November indicates a further increase in global stocks, largely attributable to higher non-OECD on-land crude inventories.

According to the U.S. Energy Information Administration's latest

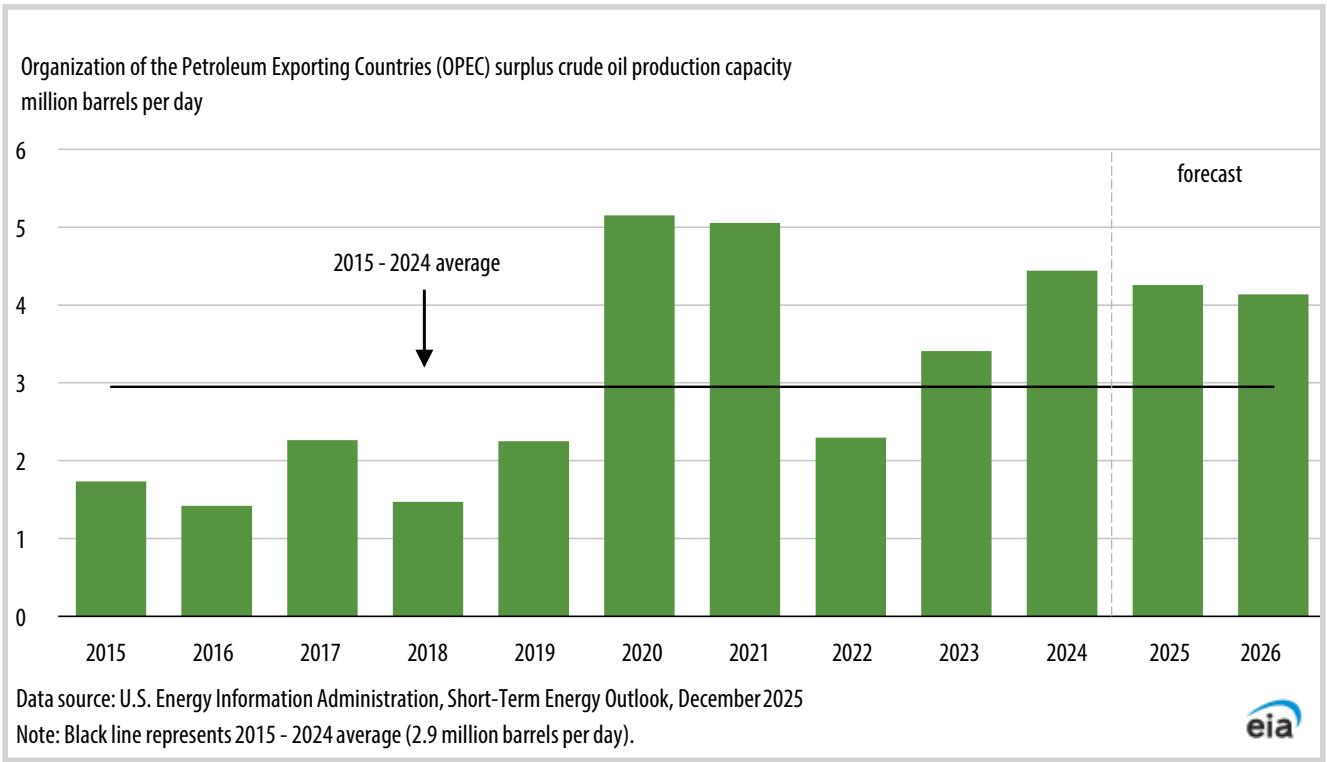

Figure 4. *OPEC surplus crude oil production capacity [4].*

short-term energy outlook [4], the Brent crude oil spot price averaged USD 64 per barrel in November, USD 11 per barrel lower than in November 2024. The EIA reports that crude oil prices continue to fall in the coming months as growing global oil production and lower demand over the winter will accelerate the accumulation of oil inventories. EIA projects that the Brent price will drop to an average of USD 55 per barrel in the first quarter of 2026 and will remain near that price for the rest of the year.

The EIA's assessment indicates that strong global oil production growth has outpaced consumption in recent months, leading to a rapid rise in global oil inventories in the second half of 2025. In 2026, the EIA expects production and consumption to grow at similar rates, but notes that production levels will continue to exceed consumption, further adding to inventories (Figures 2 - 6). The agency forecasts that global oil inventory builds will exceed 2 million barrels per day in 2026, broadly in line with 2025. Persistent inventory builds could fill commercial storage options on land, which may prompt market participants to increasingly seek other, more expensive options for storing crude oil, such as floating storage. As a result, the EIA suggests that some of the crude oil price declines will likely reflect the higher marginal cost of storage.

The EIA forecasts that global liquid fuels consumption will increase by 1.1 million barrels per day in 2025 and by 1.2 million barrels per day in 2026 (Figure 6). Global liquid fuels consumption growth is driven primarily by non-OECD countries. The EIA's analysis indicates that most non-OECD growth is concentrated in Asia. The total liquid fuel consumption in China is expected to increase by 250,000 barrels per day in 2025 and by an additional 300,000 barrels per day in 2026. The EIA notes it has raised its forecast of 2026 oil consumption in China by 50,000 barrels per day from last month's STEO due to upward revisions to expected GDP growth. The agency expects India's liquid fuel consumption to increase by 70,000 barrels per day this year and 170,000 barrels per day next year. The Middle East is also a significant source of non-OECD demand growth, increasing by 170,000 barrels per day in 2025 and 100,000 barrels per day in 2026. The agency forecasts total liquid fuel consumption in Africa will increase by 240,000 barrels per day in 2025 and 150,000 barrels per day in 2026, led by strong growth in Sub-Saharan Africa.

The EIA forecasts global liquid fuels production will increase by 3.0 million barrels per day in 2025 and by more than 1.2 million barrels per day in 2026. Along with OPEC+, the United States, Brazil, Guyana, and Canada are expected to drive production growth. Together these four countries contribute more than 50% (1.5 million barrels per day) of total global growth this year and about 60% (0.8 million barrels per day) in 2026. The EIA notes that production in South America has been the leading source of growth in 2025 as new offshore vessels

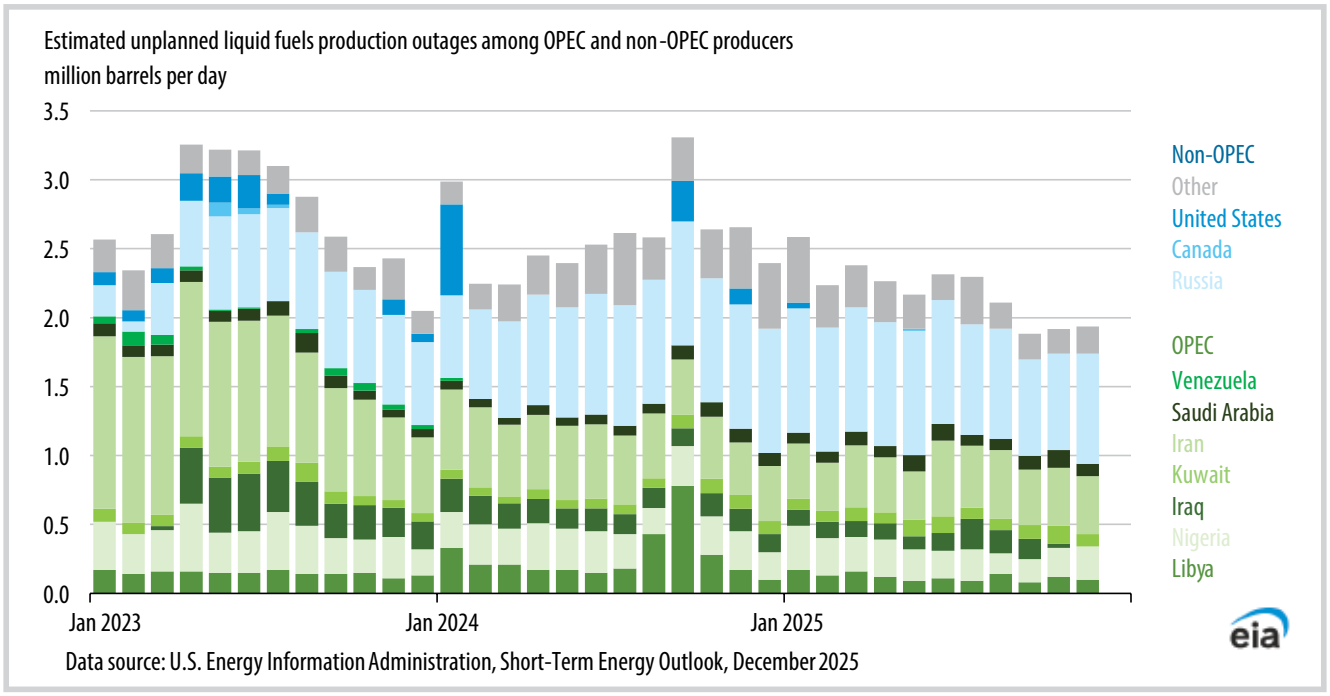

Figure 5. *Estimated unplanned liquid fuels production outages among OPEC and non-OPEC producers [4].*

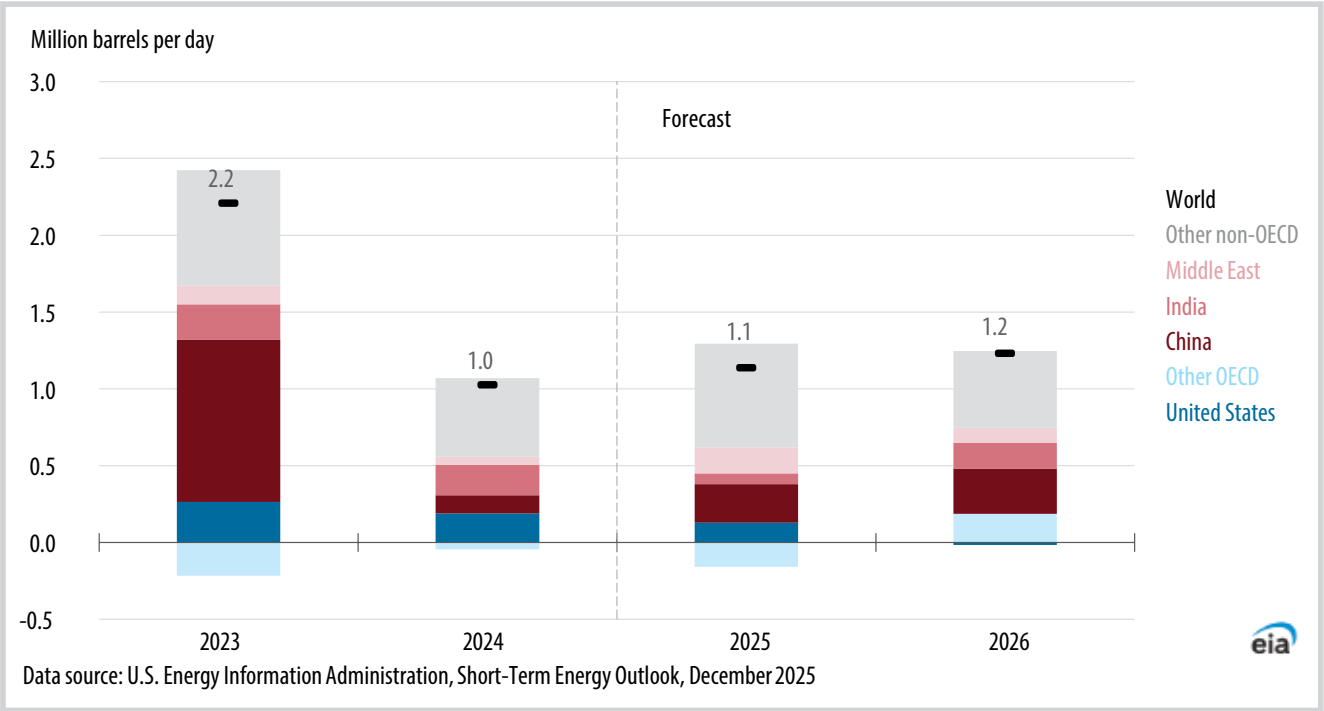

Figure 6. *Annual change in global liquid fuels consumption [4]*

have started up ahead of schedule in Brazil and Guyana, with additional projects still in development.

According to Petroleum Economist [5], several analysts, including Rapidan Energy Group, expect oil prices to come under pressure next year as supply exceeds demand. If market surpluses materialise, either OPEC+ or sanctions must reduce supply; otherwise, prices will fall until high-cost producers, especially US shale, pull back. The oil industry is not investing nearly enough to meet global demand growth that will continue after 2030, when demand fails to peak. BP, Equinor, McKinsey and other forecasters are already pushing their peak-demand estimates further into the future [5]. According to Bloomberg, IEA will reintroduce a policy-neutral reference case in its forthcoming World Energy Outlook, showing continued oil demand growth through 2050. For the first time in 5 years, the world's most influential energy forecaster is expected to project that, under current policies, oil and gas demand will rise indefinitely rather than peak imminently.

Goldman Sachs forecasts that Brent and WTI crude prices will decline further, averaging USD 56 per barrel and USD 52 per barrel, respectively, in 2026. The bank notes that barring large supply disruptions or OPEC production cuts, lower oil prices in 2026 will likely be required to rebalance the market after 2026. The bank expects prices to bottom around mid-2026 as demand grows by about 1.2 million barrels per day. Goldman then sees a gradual recovery, with Brent and WTI reaching about USD 80 per barrel and USD 76 per barrel by late 2028 [6].

Hong Hanh

References

[1] RystadEnergy, "Key digital initiatives could save oil and gas industry over $320 billion", 2025.

[2] Woodmackenzie, "Corporate oil & gas: 5 things to look for in 2026", 2025. [Online]. Available: https://www.woodmac.com/news/opinion/corporate-oil-gas-2026-outlook.

[3] International Energy Agency (IEA), "Oil market report", 12/2025. [Online]. Available: https://www.iea.org/reports/oil-market-report-december-2025.

[4] U.S. Energy Information Administration (EIA), "Short-term energy outlook", 12/2025. [Online]. Available: https://www.eia.gov/outlooks/steo/.

[5] Bob McNally, "Outlook 2026: The next oil shock - From peak demand mirage to structural tightness", 2025.

[6] Reuters, "Goldman sees gold at $4,900 by December 2026, projects oil price decline; copper remains favored industrial metal", 2025.